UNIVERSITY OF CALIFORNIA,
IRVINE

Uptake of Water and Other Molecules by Aerosolized Nanoparticles

DISSERTATION

submitted in partial satisfaction of the requirements
for the degree of

DOCTOR OF PHILOSOPHY

in Chemistry

by

Amanda Claire MacMillan

Dissertation Committee:
Professor Sergey A. Nizkorodov, Chair
Professor Douglas J. Tobias
Professor Matthew Law

2015

Dedication

To my Father

"It's not worth it if it isn't difficult."

Table of Contents

iii

List of Figures

Chapter 1: Introduction

Chapter 2: Experimental and Computational Methods

x

Chapter 4: Interaction of Water Vapor with the Surfaces of Imidazolium-Based Ionic Liquid Nanoparticles and Thin Films

Chapter 6: CO$_2$ Sequestration in Aerosolized Ionic Liquid Nanoparticles

Chapter 7: Ionic Liquids as Suitable Seed Particles for Secondary Organic Aerosol Formation and Growth

Appendix A: One- and Two-Parameter Correlative Liquid Activity Coefficient Models

List of Tables

Acknowledgements

Firstly, I would like to thank my research advisor, Professor Sergey Nizkorodov. Sergey is an amazing person and a fantastic boss. I am so thankful that I was able to work in his research group. I have learned so much during my time at UCI. I entered graduate school with a goal: learn a variety of skills and techniques, so that, when I left UCI, I would be a well-rounded chemist and professional. I definitely feel like I accomplished this goal and I owe a large portion of that, if not all of it, to Sergey's leadership, motivation, guidance, and support. I am so proud to become an alumnus of Sergey Nizkorodov's Aerosol Photochemistry Group. Thank you, so much, Sergey. I would also like to thank my dissertation committee, Professor Douglas Tobias and Professor Matthew Law.

I would like to thank my fellow research group members, as well. I joined Sergey's group at a time when there were only two other graduate students, Dr. Tran Ngyuen and Dr. Adam Bateman. Now, as I get ready to end my graduate studies at UCI, our group is seven strong! All of my fellow research group members, past and present, are fantastic people. I have thoroughly enjoyed their company. Not only while working alongside them in the laboratory and office, but also during our fun-tastic get-togethers. I will always have fond memories of our bowling parties, movie nights, bocce ball tournaments, awkward ~~family~~ group photos, barbecues in the park, and winter beach trips. I especially enjoyed the projects that I co-collaborated on with other group members. I would like to thank my fellow group members Sandra Blair and Paige Aiona, whom I worked with on two separate projects investigating the composition and photochemistry of diesel fuel (Sandra) and naphthalene (Paige) secondary organic aerosol (SOA).

project to investigate the phase state of laboratory-generated and ambient SOA. Dr. Peng Lin, at the Environmental Molecular Science Laboratory (EMSL) at Pacific Northwest National Laboratory (PNNL), for his help with the nano-DESI HR-MS and HR-LC-MS analysis of the naphthalene and diesel SOA samples. I am grateful to Dr. Alexander Laskin and Dr. Julia Laskin for not only allowing me to work in EMSL, learning how to use nano-DESI HR-MS to analyze SOA samples, but also for their hospitality while staying in Washington.

I would also like to thank my sources of funding. One of the highlights of my time in graduate school was becoming a NSF Graduate Research Fellowship Program Fellow. I am so very thankful that I was chosen. Other sources of funding include an AirUCI NSF grant and a UCI Regent's Dissertation Fellowship.

I especially would like to thank my undergraduate research advisor, Professor Karen Steelman. As an undergraduate, I was new to conducting research and am so grateful that it was in her research group. I spent almost three years in her group and worked on a variety of projects. During that time, I accrued a wide range of skills and gained valuable experiences with research concepts and techniques. My involvement with those projects strengthened my communication and scientific writing skills through presenting my research and writing project reports, journal articles, and research grant applications. It was in Dr. Steelman's group that I discovered my love of conducting research and working in the laboratory. The time I spent in her group was invaluable to my graduate school experience. I am also fairly certain that some of Dr. Steelman's Analytical Chemistry background rubbed off on me. ☺

Of course, none of this would have been possible without my wonderful family. My family has always been extremely supportive and proud of me and my accomplishments. My father advised me long ago to major in Chemistry (I had initially considered Biology). I finally took his advice (one year into chemistry research and I was hooked!) and never looked back.

Thank you, Dad. Thank you for your foresight. Thank you for pushing me to be my very best.

Thank you for believing in me. And, thank you for always letting me know how very proud you

were of me. ♥

My sister has also been a huge source of support and encouragement for me. She is

possibly my loudest, most boisterous cheerleader and I love her for that. I am so grateful to have

such an incredible sister and friend. Thank you, Sissy. Finally, I have to give a very special

thanks to my significant other, Dr. Nathaniel Sickerman. He has been extremely supportive of

me throughout my graduate career. I am forever indebted to him for his help, advice, friendship,

love, and support.

Curriculum Vitae

Amanda Claire MacMillan

385 Rowland Hall ● University of California, Irvine ● Irvine, CA 92697
Office Phone: (949) 824-7473 ● Cell Phone: (501) 960-8570 ● Email: amacmill@uci.edu

Education:

Ph.D. in Chemistry, University of California, Irvine. Irvine, CA. Received December 2015.

M.S. in Chemistry, University of California, Irvine. Irvine, CA. Received June 2011.

B.S. in Chemistry and Biology, University of Central Arkansas, Minor in Honors Interdisciplinary Studies. Conway, AR. Received May 2008.
- Honors Thesis: "Interconnecting and Coordinating Traffic Signals: A case study for Conway, Arkansas", Advisor: Dr. Jerry Reynolds

Research Experience:

Graduate Research Assistant, University of California, Irvine. (December 2009–Present)
Department of Chemistry, Principle Investigator: Dr. Sergey Nizkorodov
- Interactions of water molecules and nanometer-sized particles
- Composition and chemistry of secondary organic aerosols

Undergraduate Research Assistant, University of Central Arkansas. (September 2005–May 2008)
Department of Chemistry, Principle Investigator: Dr. Karen Steelman
- Plasma oxidation and accelerator mass spectrometry radiocarbon measurement of environmental and archeological samples

Work Experience:

Production Chemist, Rineco Chemical Industries, Inc., Benton, AR (October 2008–July 2009)
- Superintendent for an environmental services and waste management company, specializing in waste recycling, disposal, and fuel-blending.
- Responsibilities included: supervising lab technicians and plant workers; daily plant inspections to ensure RCRA, OSHA, and EPA compliance; review of all incoming waste profiles; on-site laboratory analysis of waste; determination of proper method for plant processing of waste; release of all waste material for plant processing.

Teaching Experience:

AirUCI Workshop in Environmental Chemistry Teaching Assistant, University of California, Irvine.
- AirUCI Outreach Program for Science Teachers; laboratory module: "Ability of catalytic converters to reduce air pollution from automobiles" (Summer 2011)

Graduate Teaching Assistant, University of California, Irvine.
- Analytical Chemistry laboratory (Fall 2009); General Chemistry I laboratory (Winter 2010); Physical Chemistry laboratory (Spring 2010)

Undergraduate Teaching Assistant, University of Central Arkansas.
- College Chemistry I laboratory (Fall 2007); Organic Chemistry I laboratory (Fall 2007)

Publications:

MacMillan, A. C.; McIntire, T. M.; Epstein, S. A.; Nizkorodov, S. A. Effect of Alkyl Chain Length on Hygroscopicity of Nanoparticles and Thin Films of Imidazolium-Based Ionic Liquids. *J. Phys. Chem. C* **2014**, *118* (50), 29458–29466. **DOI**: 10.1021/jp503049j

O'Brien, R. E.; Neu, A.; Epstein, S. A.; MacMillan, A. C.; Wang, B.; Kelly, S. T.; Nizkorodov, S. A.; Laskin, A.; Moffet, R. C.; Gilles, M. K. Phase State and Physical Properties of Ambient and Laboratory Generated Secondary Organic Aerosol. *Geophys. Res. Lett.* **2014,** *41* (12), 4347–4353. **DOI:** 10.1002/2014GL060219

MacMillan, A. C.; McIntire, T. M.; Freites, J. A.; Tobias, D. J.; Nizkorodov, S. A. Interaction of Water Vapor with the Surfaces of Imidazolium-Based Ionic Liquid Nanoparticles and Thin Films. *J. Phys. Chem. B* **2012**, *116* (36), 11255–11265. **DOI**: 10.1021/jp305029n

MacMillan, A. C.; Morrison, J. B.; Harmon, C. W.; Nizkorodov, S. A. Enhancement of Surfactants in Nanoparticles Produced by an Electrospray Aerosol Generator. *Aerosol Sci. Technol.* **2012,** *46* (11), 1239–1245. **DOI**:10.1080/02786826.2012.708946

Marley, N. A.; Gaffney, J. S.; Tackett, M.; Sturchio, N. C.; Heraty, L.; Martinez, N.; Hardy, K. D.; Marchany-Rivera, A.; Guilderson, T.; MacMillan, A.; Steelman, K. The impact of biogenic carbon sources on aerosol absorption in Mexico City. *Atmos. Chem. Phys.* **2009,** 9, 1537–1549. **DOI**:10.5194/acp-9-1537-2009

Steelman, K.; MacMillan, A.; Shearer, J.; McQueen, M. *Analysis of organic residue from possible mammoth rubbing stones, Sonoma, California*; Interdepartmental Report for California State Parks: Sonoma Coast State Beach, CA, 2008, 1–4. [*Filed*]

Steelman, K.; MacMillan, A.; McQueen, M. *Radiocarbon dating of pictograph samples for site 24TT0006, Teton County, Montana, USDA-Forest Service, Lewis and Clark National Forest*; Interdepartmental Report for the USDA-Forest Service: Teton County, MN, 2007, 1–5. [*Filed*]

Publications in Preparation:

MacMillan, A. C.; Blair, S. L.; Lin, P.; Laskin, J.; Laskin, A.; Nizkorodov, S. A. Effect of SO_2, NH_3, Relative Humidity, and Photolysis on Photooxidized Biodiesel and Diesel Fuel Secondary Organic Aerosol Composition. *Environ. Sci. Technol.* **2015.**

Blair, S. L.; MacMillan, A. C.; Drozd, G. T.; Goldstein, A. H.; Lin, P.; Laskin, J.; Laskin, A.; Nizkorodov, S. A. Composition and Photochemistry of Diesel Fuel Secondary Organic Aerosol. *Atmos. Chem. Phys.* **2015.**

Zhang, X.; Helgestad, T.; MacMillan, A. C.; Aiona, P. K.; Lee, J.; Novak, G.; Lin, P.; Perraud, V.; Laskin, J.; Laskin, A.; Bertram, T. H.; Cappa, C.; Nizkorodov, S. A. Optical Properties and Molecular Composition of Photooxidized Naphthalene Secondary Organic Aerosol. *Phys. Chem. Chem. Phys.* **2015.**

Phalen, R. F.; MacMillan, A. C.; Herman, D. A.; Keebaugh A.; Owens, L. P. (editors), Advances in Aerosol Dosimetry Research: Proceedings of a Conference, APHEL Report, University of California, Irvine, **2015.**

Oral Presentations:

"Effect of SO_2 and Photolysis on Photooxidized Diesel Fuel Secondary Organic Aerosol Composition", American Geophysical Union Fall Meeting, San Francisco, CA (December 16, 2014)

"Interaction of Water Vapor with the Surfaces of Imidazolium-Based Ionic Liquid Nanoparticles and Thin Films", 8th AirUCI Workshop in Chemistry, Laguna Beach, CA (January 19, 2012)

"Mexico City 2003 Carbonaceous Aerosol Radiocarbon Measurements", 64th American Chemical Society Southwest Regional Meeting, Little Rock, AR (October 2008)

"Radiocarbon Measurements of Black Carbon in Mexico City Aerosol", National Conference on Undergraduate Research, Ashville, NC (April 2006)

Poster Presentations:

"Composition and Photochemistry of Diesel Fuel Secondary Organic Aerosol", 32nd Informal Symposium on Kinetics and Photochemical Processes in the Atmosphere, Northridge, CA (April 3, 2015)

"Effect of Alkyl Chain Length on Hygroscopicity of Nanoparticles and Thin Films of Imidazolium-Based Ionic Liquids", 248th American Chemical Society National Meeting, Physical Chemistry Technical Program, San Francisco, CA (August 13, 2014)

"Effect of Alkyl Chain Length on Hygroscopicity of Nanoparticles and Thin Films of Imidazolium-Based Ionic Liquids", 248th American Chemical Society National Meeting, Sci-Mix, San Francisco, CA (August 11, 2014)

"Effect of Alkyl Chain Length on Hygroscopicity of Nanoparticles and Thin Films of Imidazolium-Based Ionic Liquids", 10th AirUCI Workshop in Chemistry, Laguna Beach, CA (January 22–23, 2014)

"Interaction of Water Vapor with Aerosolized Ionic Liquid Nanoparticles and with Bulk Ionic Liquids", 242nd American Chemical Society National Meeting, Environmental Chemistry Technical Program, Denver, CO (August 31, 2011)

"Interaction of Water Vapor with Aerosolized Ionic Liquid Nanoparticles and with Bulk Ionic Liquids", 242nd American Chemical Society National Meeting, Sci-Mix, Denver, CO (August 29, 2011)

"Enhancement of Surface-Active Species in Nanoparticles produced by an Electrospray Aerosol Generator", American Association for Aerosol 29th Annual Conference, Portland, OR (October 2010)

"Radiocarbon Measurements of Carbonaceous Aerosols from Mexico City in 2003", UCA College of Natural Sciences and Mathematics Research Poster Symposium, Conway, AR (April 2008)

"Radiocarbon Measurements of Carbonaceous Aerosols from Mexico City in 2003", 235th American Chemical Society National Meeting, New Orleans, LA (March 2008)

"Measurement of ^{14}C Content in Mexico City Atmospheric Aerosol", UCA College of Natural Sciences and Mathematics Research Poster Symposium, Conway, AR (April 2007)

"Measurement of ^{14}C Content in Mexico City Atmospheric Aerosol", 233rd American Chemical Society National Meeting, Chicago, IL (March 2007)

"Sourcing ^{14}C Content in Mexico City Black Carbon Aerosol", Arkansas IDeA Network of Biomedical Research Excellence Conference, Fayetteville, AR (October 2006)

"Radiocarbon Measurements of Black Carbon in Mexico City Aerosol", UCA College of Natural Sciences and Mathematics Research Poster Symposium, Conway, AR (April 2006)

Fellowships, Scholarships, and Awards:

Joan Rowland Award, UCI Chemistry Department (Spring 2015)
Regent's Dissertation Fellowship, University of California, Irvine (Spring 2015)
Graduate Research Fellowship, National Science Foundation (Summer 2011–Summer 2014)
Michael E. Gebel Award, Gebel Foundation (Spring 2012)

I. M. Kolthoff Award, ACS Division of Analytical Chemistry (Spring 2008)
Honors College Tuition and Fees Scholarship, University of Central Arkansas (Fall 2007–Spring 2008)
Trustee Scholarship, University of Central Arkansas (Fall 2003–Spring 2007)
Arkansas Society of Professional Sanitarians Scholarship (Fall 2005)
Presidential Scholar, University of Central Arkansas (Fall 2003, Spring 2005)
Dean's List, University of Central Arkansas (Fall 2003, Spring and Fall 2004, Spring and Fall 2005, Fall and Spring 2006, Spring 2007)

Grants:

UCA Honors College Undergraduate Research Grant: "Radiocarbon Measurements of Black Carbon in Mexico City Aerosol" (Summer 2007) [*Funded*]
UCA Honors College Travel Abroad Grant: "Learning Italian in Rome, Italy" (Summer 2006) [*Funded*]

Affiliations and Activities:

American Chemical Society, Member (2006–Present)
American Geophysical Union, Member (2014–Present)
American Association for Aerosol Research, Member (2010–2011)
Iota Sigma Pi, National Honor Society for Women in Chemistry, Member (2010–Present)
UCA Student Affiliates ACS Student Chapter, Secretary (2007–2008); Member (2006–2008)
UCA Environmental Alliance, President (2005–2006); Member (2004–2006)
UCA Sustainable Environment and Ecological Design Committee, Student Member (2004–2006)

Outreach/Community Service:

Session Monitor; Advances in Aerosol Dosimetry Conference; Beckman Center of the National Academies; Irvine, CA (October 24–25, 2014)
Irvine Unified School District Science Fair Judge; Judged both physical and biological science fair projects (February 2014)
AirUCI Workshop in Environmental Chemistry; Laboratory Tour Organizer; Irvine, CA (July 2013)
Safety on Site Representative for the Nizkorodov Laboratory (2010–2011)
Radiation Safety Officer for the Nizkorodov Laboratory (2010–2011)
California Science Program's Annual "Future of Science" Conference Volunteer; Conducted Hands-On Lab Demo; Irvine, CA (September 2010)
Santa Ana Zoo's National Chemistry Week Volunteer; Santa Ana, CA (October 2010)
AirUCI Workshop in Environmental Chemistry; Laboratory Tour Guide; Irvine, CA (July 2010)
Oak Grove Elementary School Volunteer; North Little Rock, AR (2005–2010)
Chemistry Tutoring Volunteer; Conway, AR (Fall 2007)
Museum of Discovery's National Chemistry Week Volunteer; Little Rock, AR (Fall 2007)
UCA Environmental Alliance Earth Day Co-coordinator; Conway, AR (2005–2006)
Heifer International Organic Garden Volunteer; Heifer Ranch; Perryville, AR (Summer 2005)
Game & Fish Commission Stream Team Clean-Up Coordinator/Participant; Conway, AR (2004–2006)
Arkansas Earth Day Volunteer; Conway, AR (2004–2005)

Abstract of the Dissertation

Uptake of Water and Other Molecules by Aerosolized Nanoparticles

By

Amanda C. MacMillan

Doctor of Philosophy in Chemistry

University of California, Irvine, 2015

Professor Sergey A. Nizkorodov, Chair

The fundamental properties of 1-n-alkyl-3-methylimidazolium ([C_nMIM$^+$], n = number of carbons on the linear alkyl chain)-based ionic liquids (ILs) are not fully characterized, including quantification of the amount of water or carbon dioxide (CO_2) absorbed from the atmosphere and the nature of the IL–water or IL–CO_2 interactions. For example, interactions of bulk ILs and water in previous studies were limited by slow equilibration times of the ILs when exposed to water vapor. This is the first study of the interaction of water or CO_2 with aerosolized IL nanoparticles. The particles' small size ensures IL–water vapor equilibrium is achieved quickly. Additionally, ILs may have the ability to absorb large amounts of CO_2 and can be used for CO_2 sequestration in the environment.

The combined experimental and theoretical techniques of tandem nano-differential mobility analysis (TDMA), attenuated total reflection-Fourier transform infrared (ATR-FTIR) spectroscopy, and molecular dynamics (MD) simulations were used to provide a comprehensive picture of the behavior of absorbed water or CO_2 in IL nanoparticles and thin films. [C_nMIM]$^+$ (n = 2, 4, or 6) paired with Cl$^-$ or BF$_4^-$ were studied to examine the effect of alkyl chain length on IL hygroscopicity and CO_2 uptake. Particles' growth from water or CO_2 uptake was

quantified using TDMA. For the hygroscopicity studies, growth curves show steady uptake of water vapor with increasing relative humidity. Water molar fractions (χ_w) agreed well with those estimated from ATR-FTIR data. Additionally, the performance of several liquid activity coefficient models were evaluated by fits to the experimental data. MD simulations, used to model IL−water interactions, revealed considerably stronger interactions between Cl^- and water compared to BF_4^- and water. The increase in growth factor after CO_2 exposure showed little change for the IL studied. These combined experimental, theoretical, and modeling techniques help provide a more complete picture for these two families of ILs in the presence of water or CO_2. The techniques also provide a quantitative parameterization of the amount of water vapor that ILs with different alkyl chain lengths can absorb under equilibrium conditions.

The use of ILs as suitable seed particles for secondary organic formation and growth from α-pinene ozonolysis in an environmental smog chamber was also explored. Additionally, we investigated the sensitivity of the nanoparticles' chemical composition to varying operation conditions in electrospray aerosol generators.

Chapter 1: Introduction

1.1. Introduction

1.1.1. Nanoparticles and the Environment

Nanoparticles are particles with aerodynamic diameters less than 50 nm.[1] They are generated by a variety of sources, including biogenic (e.g., vegetation and sea spray) and anthropogenic (e.g., vehicles and industries).[1] They are characterized by large surface-to-volume ratios, which translate into unique physical and chemical properties. Atmospheric nanoparticles represent the most important type of particulate matter in the atmosphere in terms of number density.[1] Their surfaces serve as the sites of important heterogeneous atmospheric reactions and nanoparticles themselves act as nuclei in cloud formation.[1,2] Nanoparticles can also adversely affect human health; their small size can easily penetrate the lining of the lung or enter the brain via the central nervous system, causing illness and even death.[1,3,4]

Despite the fact that nanoparticles are fairly ubiquitous throughout the atmosphere, their unique chemical and physical properties (the result of their large surface-to-volume ratios) are still not well understood. Too few studies have been conducted to investigate the fundamental properties of nanoparticles and only recent improvements in aerosol technology, specifically the introduction of differential mobility analyzers (DMAs) and ultra-fine condensation particle counters for nanoparticles, have made the study of nanoparticle interactions with other species even possible.[5–7]

Understanding the fundamental properties of nanoparticles is a cornerstone to understanding the behavior of nanoparticles in the environment. This is especially necessary because nanoparticles are abundant throughout the atmosphere.[1] Additionally, nanoparticles will soon be key elements of future technology, such as solar energy conversion, drug delivery, nano-materials, medical diagnostics, and computing.[8] A better understanding of the interactions of

2

nanoparticles with water and CO_2 is of particular importance for several reasons. Most notably: because water and CO_2 exist literally everywhere. Additional reasons will be discussed in detail below.

1.1.2. Hygroscopic Growth of Aerosolized Nanoparticles

Water is ubiquitous in the environment. After exposure to dry nanoparticles, water can adhere to the nanoparticles' surface. This causes the dry particle can grow in size (Figure 1.1).[9–12] To quantify the amount of water vapor particles can take up (i.e., their "hygroscopicity"), the difference in size between the wet and dry nanoparticle can be calculated using the Growth Factor (GF) (eq 1.1).

$$GF\left(RH\right) = \frac{d_{m,wet}\left(RH\right)}{d_{m,dry}} \tag{1.1}$$

where $d_{m,\,wet}$(RH) is the mobility-equivalent diameter of the particles in equilibrium with water vapor at a specific relative humidity (RH) and $d_{m,dry}$ is the mobility-equivalent diameter of the dry particles. Plotting the GF as a function of RH allows one to observe the behavior of nanoparticles exposed to water vapor. The behavior of nanoparticles exposed to a wide range of humidity values (e.g., 0 to 100% RH) can be observed by plotting the GF as a function of RH to obtain a growth curve. Growth factors, growth curves, and the techniques used to measure them are further explained in Chapters 2–5.

In regards to nanoparticles in the atmosphere, knowledge of nanoparticle hygroscopicity provides insight into how clouds are formed. It also aids in understanding how nanoparticle composition can affect water uptake (Chapter 3). Water can also interact with nanoparticles, along with other organic precursors and oxidants, to promote reactions leading to the formation of secondary organic aerosol (SOA) (Chapter 7). Most importantly, uptake of water can alter

nanoparticles physical and chemical properties.[13–15] Thus, quantifying nanoparticles hygroscopicity is vital to further the use of nanoparticles in industrial and technological applications (Chapter 4–5).
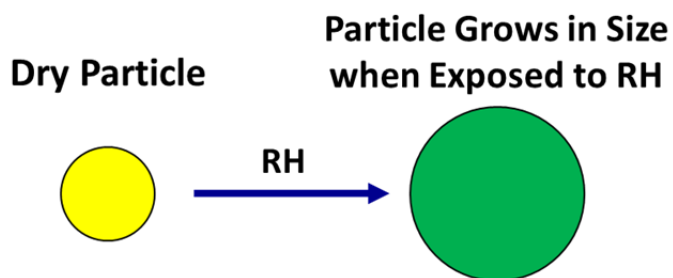
Figure 1.1. Cartoon of exposing a dry nanoparticle to relative humidity (RH), which causes the particle to increase in size.

1.2. Generation of Nanoparticles

1.2.1. Electrospray

Electrospray is a process of creating small highly charged droplets by dispersing a conducting solution through an electrified capillary. In electrospray ionization (ESI), the conditions are optimized for mass spectrometric analysis so that the droplets disintegrate down to individual ions through a series of droplet fission and solvent/ion evaporation steps.[16,17] An electrospray aerosol generator (EAG) employs a somewhat different set of conditions to produce particles in the nanometer to micron size range.[18–21] Generally, this is achieved by keeping the solution concentrations several orders of magnitude higher than in ESI (mM vs. μM) and removing the excess charge from the particles immediately after the electrospray process.

Under appropriately chosen conditions, such as capillary flow and applied potential, electrospray operates in a cone-jet mode,[22] in which the liquid exiting the capillary forms a sharp

conical tip, known as the Taylor cone. As first described by Taylor,[23] charged primary droplets containing both the solutes and solvent break off from the Taylor cone and travel towards the nearest grounded surface. It is believed that solvent evaporation causes shrinkage of these primary droplets, which leads to asymmetric fission events at the Rayleigh space charge limit and result in a release of several *progeny* droplets.[16] The progeny droplets carry only a fraction of the primary particle mass and remove a substantial fraction of its charge. These processes take place on a millisecond time scale, and by the time the droplets reach the grounded surface several evaporation/fission cycles may have already occurred (Figure 1.2). In EAG applications, droplet fission is typically suppressed by injecting the droplets directly into a weak plasma,[24] which facilitates the flow of the excess charge between the droplets and the surrounding metal surfaces.
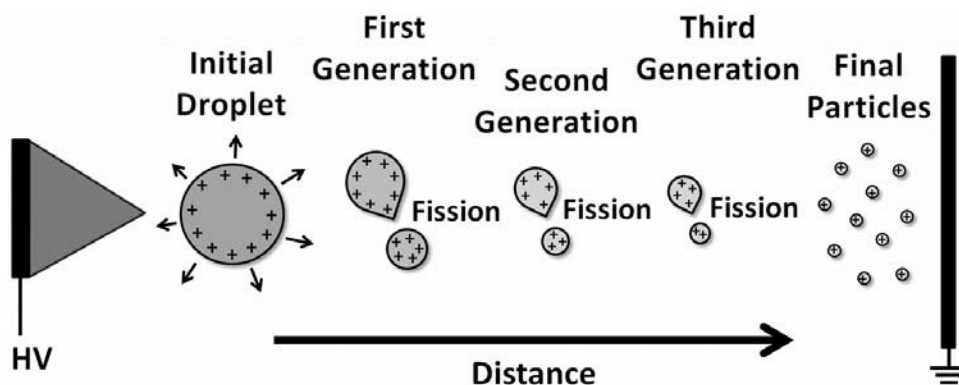
Figure 1.2. Cartoon of the fission process droplets undergo as they break off from the Taylor cone and travel (left to right) toward the neutralizer.

1.2.2. Surfactant Enhancement in Nanoparticles

In the electrospray process, as the progeny droplets break off from the apex of a distorted primary droplet they may become enriched with the more surface-active solute. It is well known

that ESI sources preferentially generate ions corresponding to molecules with high surface activities due to the interplay between surface charge and surface tension.[25] An enhancement in the surface-active species in nanoparticles generated by EAG has also been noted in previous work.[9,10,26] Several experimental parameters are expected to affect the enhancement, including the capillary voltage, capillary (i.e., liquid) flow rate, drying air flow rate, and the distance (l_s) of the electrospray capillary tip to the neutralizing surface.

The effect of these parameters on the enhancement of surface-active species in nanoparticles has not been systematically investigated. One relevant study was conducted by Schmidt et al.,[27] who examined the effect of liquid flow rates on the ESI mass spectra of solutions containing solutes with significant differences in surface activities. They observed a strong suppression of the signal intensity of hydrophilic solutes with decreasing flow rate. They attributed this effect to smaller initial droplet sizes obtained at reduced flows resulting in a greater chance that surface-active solutes would remain in progeny droplets during fission events.

Another relevant study by Benkestock et al.[28] investigated the effect of changing various electrospray parameters, including l_s, on the concentration of non-covalently bound complexes between proteins and small organic ligands. They found that the protein–ligand complex to free protein ratio increased with l_s when a hydrophilic ligand was used, whereas the opposite trend was observed using hydrophobic ligands. They attributed this effect to preferential sampling of ions from the bulk of the primary droplet through formation of late-generation residue droplets at large values of l_s. Chapter 3 of this dissertation discusses the effect of l_s on the enhancement of surface-active species in nanoparticles containing a hygroscopic salt and an ionic surfactant produced by an EAG.

1.3. Ionic Liquids Overview

Ionic liquids (ILs) are organic salts with melting points around or below 100 °C. They comprise a large class of molecules due to a nearly unlimited number of cation–anion combinations (estimated at over one million).[15] ILs differ from traditional molten salts (e.g., NaCl) because of their lower boiling points and most are liquid at room temperature.[15] They have unique physical and chemical properties that are highly tunable, depending on the combination of cation and anion.[14,15,29]

These "designer" salts have properties customizable to suit any task and an almost unlimited number of potential cation–anion pairs (a significant portion of which have not been created or discovered, yet).[14,30,31] Chemistry research on ILs is being conducted by a variety of sub-disciplines, from electrochemistry and organic chemistry to even atmospheric chemistry.[14,15,31] Starting in the year 2000, the number of publications on ILs has been increasing exponentially.[15] The IL publication rate, from both academia and industry, for the past two decades (January 1995 to November 2015) is shown in Figure 1.3 (from Sci-Finder). In 2014 alone, there were 6,720 papers published on ILs. That is 18 papers published daily, 126 papers published weekly. Comparing the year 2014 to 2009 (the year I started my graduate research on ILs), publications have increased by 70%. [Note: while the number of 2015 publications is lower than the number published in 2014, this is most likely because the data was collected in November 2015. By the end of this year, I am confident that the total number of 2015 IL publications will surpass the 2014 total.] Discovery, design, and utilization of ILs in a myriad of applications continues to increase rapidly and will likely not show signs of slowing down for a long time.[14,15]
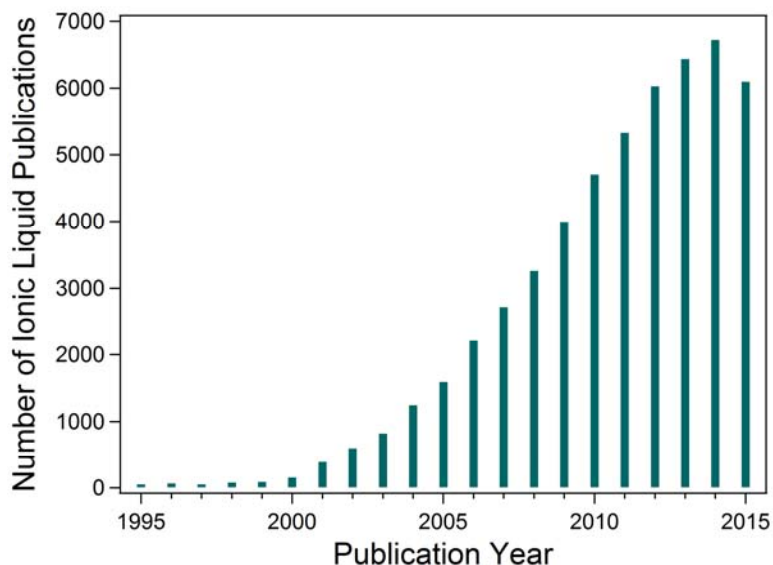
Figure 1.3. Number of academic and industrial papers published on ionic liquids in the past two decades (January 1995 to November 2015). (Source: Sci-Finder.)

ILs possess several distinctive physicochemical properties that have sparked a significant interest in the use of ILs in Green Chemistry,[13,32] for example, the use of ILs as industrial solvents. Conventional industrial solvents emit large amounts of volatile organic compounds (VOCs) into the atmosphere, a major source of air pollution.[29,31] The negligible vapor pressures of ILs make them promising alternatives to traditional industrial solvents.[31] Other notable properties of ILs include non-flammability, high thermal stability, broad liquidus temperature range, wide electrochemical window, and being highly solvating for several types of solutes. Along with low vapor pressures, these properties have allowed ILs to be used in several interesting applications[15] including: batteries, fuel cells,[33] fuel additives, biopreservation, gas capture and storage,[34–37] and chemical extraction.[15,29,32]

Physical properties such as conductivity, viscosity, density, and surface tension of ILs are known to be affected by the presence of contaminants,[14,38] such as water vapor in the hygroscopicity studies discussed below. As stated previously, design of various applications involving task-specific ILs are dictated by knowing the exact physical and chemical properties of the IL in use.[14,15] There is a great need to gather an extensive body of information on the physical properties of these unique substances. Due to the lack of data regarding ionic liquids' physical properties, the ability to fully utilize these unique substances is hindered. Thus, understanding the effects of contaminants, such as water vapor, on ILs are critical for use of ILs in future applications. [14,38–44]

1.4. Interaction of Water with Ionic Liquids

1.4.1. Previous Studies

As mentioned previously, IL physical properties are known to depend on the presence of water, both adsorbed and absorbed.[14,38] Water is ubiquitous in the environment and hygroscopic ILs, such as those with 1-n-alkyl-3-methylimidazolium ([C$_n$MIM]$^+$, n = number of carbons on the linear alkyl chain) cations, can uptake considerable amounts of water vapor from ambient air.[14,15] Even ILs considered "hydrophobic", such as those with [C$_n$MIM$^+$] cations and hexafluorophosphate (PF$_6^-$) anions can uptake ambient water vapor, 0.16 χ_w (molar fraction of water), over a three hour period.[14] Both absorbed and adsorbed water can dramatically alter the physical and chemical properties of ILs. Understanding the effects of water on ILs, including quantification of water vapor uptake and insight into IL–water interactions, are critical for use of ILs in future applications. [38–44]

Numerous experimental and theoretical studies have investigated the interaction of imidazolium-based ILs with water.[14,38–65] It is understood that both the cation and the anion have an effect on how ILs interact with water, with the anion having a stronger effect.[14,47,49] Early experimental work by Seddon et al. investigated the miscibility of water with ILs containing $[C_nMIM]^+$ cations and various anions at room temperature.[14] It was determined that, regardless of the alkyl chain length, all halide anions were fully soluble in water and all PF_6^- anions were insoluble.[14] However, alkyl chain length did have an effect on water miscibility of $[C_nMIM]^+$-based ILs with tetrafluoroborate (BF_4^-) anions; for chain lengths of $n = 2$ or 4, the ILs were fully miscible, but for $n > 4$, the ILs formed biphasic systems.[14]

Cammarata et al. performed early attenuated total reflection (ATR) infrared (IR) studies on the molecular states of water absorbed from the atmosphere in ILs under ambient conditions.[49] For 1-butyl-3-methylimidazolium tetrafluoroborate ($[C_4MIM][BF_4]$), water interacted mainly with the anions at low water content to create stable hydrogen bonds (H-bonds) to two BF_4^- anions, via $[F^-\cdots H–O–H\cdots F^-]$ bridges.[49] The IR spectra showed two bands at 3640 and 3560 cm^{-1} characteristic of the water forming H-bonds to the anions; a predominance of these complexes occurred at χ_w (the molar fraction of water in the IL–water mixture) < 0.2, while the formation of H-bonded water clusters was favored at $\chi_w > 0.3$. However, for more basic anions, such as acetate, one broad band around 3400 cm^{-1} indicated the preference to form water–water aggregates.[49] Similarly, more recent ATR–Fourier transform infrared (FTIR) and NMR studies involving the interaction of 1-ethyl-3-methylimidazolium tetrafluoroborate ($[C_2MIM][BF_4]$) and water molecules also observed a significant change in the state of water molecules in $[C_2MIM][BF_4]$ at $\chi_w \approx 0.3$.[60] In addition, large-angle X-ray scattering experiments showed that as the concentration of water increased in $[C_2MIM][BF_4]$ solutions, stronger

interactions between the C2 on the ethyl imidazolium ring and the BF_4^- anion occur, with a concomitant weakening of interactions at C4 and C5 (Figure 1.4).
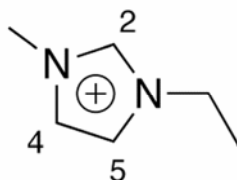
Figure 1.4. Example of imidazolium cation structure (i.e., $[C_2MIM]^+$) with carbons on the imidazolium ring labeled.

Early molecular dynamics (MD) simulations by Hanke et al. on single water molecules and 1,3-dimethylimidazolium chloride ($[C_1MIM][Cl]$) found that water interacts predominantly with Cl^- in the solution.[59] The same group investigated $[C_1MIM][Cl]$–water mixtures and observed that at low water concentrations water is either isolated or contained in small water clusters, but at higher concentrations the water molecules form a continuous network.[61] They also found that at higher water concentrations the properties of the IL–water mixture were different from the pure IL.[61] Work by Saha and Hamaguchi using single crystal X-ray diffraction and Raman spectroscopy showed that water has the ability to alter the conformation of the *n*-butyronitrile side chain in 1-butyronitrile-3-methylimidazolium halides and that water participates in a H-bonding network with the anions.[51] This H-bonding network displaces the anion's position, which disturbs the arrangement and stable molecular structure of the IL.[51]

NMR experiments carried out by Mele et al. gave direct evidence of the existence of tight ion pairs in the pure IL, even with the presence of small amounts of water.[50] The IL structure is disturbed with a lower degree of ring stacking by cation-mediated H-bonds between water and the imidazolium ion protons. MD simulations performed by Moreno et al. on $[C_4MIM][BF_4]$–

water mixtures from 0 to 0.5 χ_w indicated that at low χ_w the water molecules are selectively

coordinated to both the cation and anion, and the ionic network is unperturbed.[58] However, at

higher χ_w they observed the formation of whole water clusters that perturbed the ionic network.

Additionally, they found water clusters formed almost entirely from linear chains of H-bonded

molecules. Far-IR measurements and density functional calculations by the Ludwig group

correlated cation–anion cohesive energies in imidazolium-based ILs; the intermolecular

stretching modes shifted to higher energies as the anion ionic strength increased.[62,66] Recently,

cohesive energies and the electron density of H-bonding interactions for imidazolium-based ILs

as a function of anion identity were studied by Gao et al.[63] Their results showed that water

dissolved in ILs weakened the electron density of the C–H···Y bond between the cation and

anion. Finally, Dang and Wick performed MD simulations to calculate the potentials of mean

force for transporting a water molecule across the air–IL interface in $[C_4MIM][BF_4]$ and

$[C_4MIM][PF_6]$.[65] They found that water prefers bulk solvation with no evidence for interfacial

energy minima.

1.4.2. Interaction of Water with Ionic Liquid Nanoparticles and Thin Films

While numerous studies of water and ILs have been conducted, few studies have

attempted to quantify the amount of water vapor that ILs can absorb from the atmosphere.[42,64]

Previous studies were performed on bulk quantities of ILs. However, there are kinetic

limitations associated with studying large quantities of ILs, often taking several hours or longer

for bulk ILs to reach equilibrium with water vapor. Work by Cuadrado-Prado et al. studied the

change in mass of 1 mL volumes (initial masses: ~1–2 g) of imidazolium-based ILs with BF_4^-

and alkyl sulfate anions after exposure to varying levels of RH.[64] They found that the mass of IL

film increased as the RH increased, though it was incorrectly concluded that water was only adsorbed on the surface, creating a thin film. At 100% RH, it took from 80 to 100 h for the ILs to reach an equilibrium with the atmospheric water vapor and become completely saturated (without stirring).[64] In a similar study, Di Francesco et al. examined the kinetics of water vapor uptake by several ILs at two RH levels, 43% and 81% RH, using gravimetric analysis on initial ILs volumes of 2 mL.[42] The results showed that the more hydrophilic ILs absorbed more water vapor compared to the more hydrophobic ILs. Their study also took a long time for the ILs to either reach or begin to approach equilibrium with exposed water vapor; anywhere from 20 to 60+ h at 43% RH.[42] At 81% RH, equilibrium was reached for most of the ILs after 20, while $[C_4MIM][BF_4]$ took almost 60 h. For both RH levels, they found that $[C_4MIM][BF_4]$ took the longest time to reach equilibrium and absorbed the most amount of water, concluding that it was the most hydrophilic of the ILs in their study.[42]

The kinetic limitations associated with large quantities of IL in previous studies of water vapor absorption by imidazolium-based ILs can be circumvented by studying water uptake by IL nanoparticles (a few tens of nanometers in diameter) or thin films (a few micrometers in thickness). Hygroscopic nanoparticles generally achieve equilibrium with water vapor in a fraction of a second.[67] Using a combination of experimental, theoretical, and modeling techniques, several types of ILs were studied to investigate their interactions with water vapor and are discussed in Chapters 4 and 5.

1.6. CO$_2$ Sequestration in Aerosolized Ionic Liquid Nanoparticles

Of the various areas of academia and industry that work with ILs, the most notable are the ones that utilize ILs for Green Chemistry and Environmental Sustainability. As discussed

above, ILs have desirable properties for Green Chemistry and Environmental Sustainability applications.[15] The solubility of various gases in ILs is of particular interest.[34,35,37,68–71] Recent studies have found that ILs have a remarkable ability to solvate a wide range of gases.[34,35,68,69] A significant amount of that research is being conducted on studying the solubility and selectivity of gases, such as CO_2, in ILs.[34,35,37,68–71] Imidazolium-based IL cations have been found to be especially good solvents for CO_2.[35,37,68] Though, when comparing the effects of cation s and anions on solutbility, studies suggest the anion has more influence.[34,35,68,69]

Sequestration of CO_2 in the environment using ILs is a potential long-term storage option for CO_2, with the goal of mitigating climate change. In the study discussed in Chapter 7, the ability of aerosolized IL nanoparticles to uptake CO_2 was examined. The IL nanoparticles were composed of aerosolized 1-ethyl-3-methylimidazolium bis(trifluoromethylsulfonyl)imide ($[C_2MIM][Tf_2N]$). This particular IL was chosen for two reasons: (1) Previous studies on the solubility of various gases in bulk quantities of ILs found CO_2 to be the most soluble in $[C_2MIM][Tf_2N]$.[34,35,68] (2) It was readily available in our laboratory.

This preliminary study is unique because, to the best of our knowledge, no studies involving CO_2 sequestration by IL nanoparticles have been performed. Because of their small size and large surface areas, aerosolized IL nanoparticles have the potential to be uptake large amounts of CO_2. Furthermore, because of nanoparticles' large surface area, they might take up CO_2 faster than bulk materials.

1.7. Ionic Liquids as Suitable Seed Particles for Secondary Organic Aerosol Formation and Growth

Atmospheric chemists strive to better understand the processes occurring in the atmosphere. However, these processes are highly complex. This is especially true for the formation and composition of SOA in the atmosphere. Generating SOA in an environmental smog chamber is one way to better understand the processes involved in SOA formation and composition. There are several techniques that can be used to generate SOA in smog chamber studies. Seeding is the technique of using a starting aerosol seed particle for the organic precursor(s).[72] The seed particles act as nuclei for SOA formation to help overcome the Kelvin barrier associated with homogeneous nucleation.[7] Seed particles are introduced into the chamber before the other SOA precursors are added. In some experiments, it is advantageous for the seed particles to have the same size; in this case, the seed particles are size-selected before injecting them in the chamber.

Traditionally, the seed particles used in chamber studies are those that are already abundant in the atmosphere. This includes solid, inorganic salts (e.g., $(NH_4)_2SO_4$ and NH_4NO_3)[73] and liquid acids (i.e., H_2SO_4).[73,74] The latter is used to test the effect of seed acidity on SOA formation.[73,75–77] The choice of seed particle used to form SOA can affect the final distribution of products in the particles.[72–77] The seed particle's physicochemical properties (e.g., phase state and acidity) can alter things like SOA formation, SOA composition, reaction rates, and SOA yield in laboratory experiments.[72] However, there is still a lot that we do not know about the interactions occurring between the seed and organic precursors, as well as the reaction pathways taking place and what effect this has on the SOA composition. A better understanding

of these interactions, reactions, and end composition is vital for understanding SOA formation and composition.

Decreasing this complexity can be achieved by simplifying the starting components, such as using a seed particle that does not react with the organic precursor. While not abundant in the atmosphere, ionic liquids have physical and chemical properties that make them very promising for use as seed particles. They have negligible vapor pressures, are liquid at room temperature, and dissolve a wide range of organic compounds.[14,15,32] Because of this, it is believed that they would react less with the VOC photooxidation products compared to previous seeds studied, while at the same time promoting partition of these products in the particle phase because of their high solubility in ILs. Use of ILs in various applications continues to increase rapidly. If successful, this project might allow for ILs to be used in an even wider range of applications than those mentioned in Chapter 1.

Chapter 7 presents the results from a preliminary study to investigate the formation and composition of SOA produce from ozonolysis of α-pinene. The Chapter's Future Work section discusses the steps necessary to optimize this study for future experiments. The ILs studied as suitable seed particles for SOA growth and formation were 1-hexyl-3-methylimidazolium tetrafluoroborate ([C$_6$MIM][BF$_4$]), 1-ethyl-3-methylimidazolium bis(trifluoromethylsulfonyl)-imide ([C$_2$MIM][Tf$_2$N]), and 1-ethyl-3-methylimidazolium dicyanamide ([C$_2$MIM][dca]). These ILs were chosen because they are all liquid at room temperature and were readily available in the lab. Ozone (O$_3$) was used as the oxidant; it is not expected to be reactive with respect to ILs. (Poly)ethylene glycol (PEG) was used as the control seed particle because it is not known to react with O$_3$ and is also a liquid at room temperature. Solutions of PEG in MeOH were created to match the IL solutions.

1.8. Goals and Motivations

My thesis research is focused on trying to better understand the interactions of aerosolized nanoparticles with various species of molecules. Nanoparticles are an important type of particulate matter in the atmosphere. Understanding their fundamental properties will aid in our understanding their role in heterogeneous atmospheric reactions, cloud processes/formation, and Earth's climate. As discussed in Chapter 3, the composition of nanoparticles is highly dependent on the particle generation source parameters and starting solution composition. If exact nanoparticle compositions were needed, even slight alterations in the source or solution, as discussed in Chapter 3, could result in very different particle compositions. Chapter 4 and 5 investigate the ability of several types of ILs to take up water. This could have various effects on task-specific IL where the physical properties need to be constant; otherwise they could ruin the application that the IL was designed for. Chapter 6 will investigate another physical property of ILs: the solubility of CO_2 in ILs. Finally, Chapter 7 will continue with the ILs trend, but will take ILs out of industrial appliacations and put them to use in the field of atmospheric chemistry research. Understanding SOA formation and growth is complex. Any variation in SOA formation conditions, for example, using IL seeds, could get us one step closer to better understanding the chemistry of SOA in the atmosphere.

References

(1) Anastasio, C.; Martin, S. T. Atmospheric Nanoparticles. *Rev. Mineral. Geochem.* **2001**, *44*, 293-349.

(2) Finlayson-Pitts, B. J.; Pitts, J. N. *Chemistry of the Upper and Lower Atmosphere: Theory, Experiments, and Applications*; Academic Press: San Diego, Calif., 2000.

(3) Slezakova, K.; Morais, S.; Pereira, M. d. C. Atmospheric Nanoparticles and Their Impacts on Public Health. *Current Topics in Public Health*. [Open Access Journal], **2013**, 503-529. DOI: 10.5772/54775 .

(4) Oberdörster, G.; Sharp, Z.; Atudorei, V.; Elder, A.; Gelein, R.; Kreyling, W.; Cox, C. Translocation of Inhaled Ultrafine Particles to the Brain. *Inhal. Toxicol.* **2004**, *16*, 437-445.

(5) Rader, D. J.; McMurry, P. H. Application of the Tandem Differential Mobility Analyzer to Studies of Droplet Growth or Evaporation. *J. Aerosol Sci.* **1986**, *17*, 771-787.

(6) McMurry, P. H. A Review of Atmospheric Aerosol Measurements. *Atmos. Environ.* **2000**, *34*, 1959-1999.

(7) Seinfeld, J. H.; Pandis, S. N. *Atmospheric Chemistry and Physics: From Air Pollution to Climate Change*; J. Wiley: Hoboken, N.J., 2006.

(8) *Nanoparticles: From Theory to Application*; Schmid, G., Ed.; Wiley-VHC: Weinheim, Germany, 2004.

(9) Alshawa, A.; Dopfer, O.; Harmon, C. W.; Nizkorodov, S. A.; Underwood, J. S. Hygroscopic Growth and Deliquescence of NaCl Nanoparticles Coated with Surfactant AOT. *J. Phys. Chem. A* **2009**, *113*, 7678-7686.

(10) Harmon, C. W.; Grimm, R. L.; McIntire, T. M.; Peterson, M. D.; Njegic, B.; Angel, V. M.; Alshawa, A.; Underwood, J. S.; Tobias, D. J.; Gerber, R. B.; Gordon, M. S.; Hemminger, J. C.; Nizkorodov, S. A. Hygroscopic Growth and Deliquescence of NaCl Nanoparticles Mixed with Surfactant SDS. *J. Phys. Chem. B* **2010**, *114*, 2435-2449.

(11) MacMillan, A. C.; McIntire, T. M.; Freites, J. A.; Tobias, D. J.; Nizkorodov, S. A. Interaction of Water Vapor with the Surfaces of Imidazolium-Based Ionic Liquid Nanoparticles and Thin Films. *J. Phys. Chem. B* **2012**, *116*, 11255-11265.

(12) MacMillan, A. C.; Morrison, J. B.; Harmon, C. W.; Nizkorodov, S. A. Enhancement of Surfactants in Nanoparticles Produced by an Electrospray Aerosol Generator. *Aerosol Sci. Technol.* **2012**, *46*, 1239-1245.

(13) *Ionic Liquids: Industrial Applications for Green Chemistry*; Rogers, R. D.; Seddon, K. R., Eds.; American Chemical Society Symposium Series 818; American Chemical Society; Distributed by Oxford University Press: Washington, D.C., 2002.

(14) Seddon, K. R.; Stark, A.; Torres, M. J. Influence of Chloride, Water, and Organic Solvents on the Physical Properties of Ionic Liquids. *Pure Appl. Chem.* **2000**, *72*, 2275-2287.

(15) *Ionic Liquids in Synthesis*; 2nd ed.; Wasserscheid, P.; Welton, T., Eds.; Wiley-VCH: Weinheim, Germany, 2008; Vol. 1.

(16) Kebarle, P.; Peschke, M. On the Mechanisms by which the Charged Droplets Produced by Electrospray lead to Gas Phase Ions. *Anal.Chim. Acta* **2000**, *406*, 11-35.

(17) Kebarle, P.; Verkerk, U. H. On the Mechanism of Electrospray Ionization Mass Spectrometry (ESIMS). In *Electrospray and MALDI Mass Spectrometry: Fundamentals, Instrumentation, Practicalities, and Biological Applications*; 2nd ed.; Cole, R. B., Ed.; John Wiley & Sons, Inc.: Hoboken, NJ, 2010.

(18) Chen, D.-R.; Pui, D. Y. H.; Kaufman, S. L. Electrospraying of Conducting Liquids for Monodisperse Aerosol Generation in the 4 nm to 1.8 mu-m Diameter Range. *J. Aerosol Sci.* **1995**, *26*, 963-977.

(19) Rulison, A.; Flagan, R. C. Electrospray Atomization of Electrolytic Solutions. *J. Colloid Interf. Sci.* **1994**, *167*, 135-145.

(20) Tang, K.; Gomez, A. Generation by Electrospray of Monodisperse Water Droplets for Targeted Drug Delivery by Inhalation. *J. Aerosol Sci.* **1994**, *25*, 1237-1249.

(21) Chattopadhyay, S.; Modesto-Lopez, L. B.; Venkataraman, C.; Biswas, P. Size Distribution and Norphology of Liposome Aerosols Generated by Two Methodologies. *Aerosol Sci. Technol.* **2010**, *44*, 972-982.

(22) Jaworek, A.; Sobczyk, A. T. Electrospraying Route to Nanotechnology: An Overview. *J. Electrostat.* **2008**, *66*, 197-219.

(23) Taylor, G. Disintegration of Water Drops in an Electric Field. *Proc. Royal Soc. London. A. Math. Phys. Sci.* **1964**, *280*, 383-397.

(24) Lu, Q.; Koropchak, J. A. Corona Discharge Neutralizer for Electrospray Aerosols used with Condensation Nucleation Light-Scattering detection. *Anal. Chem.* **2004**, *76*, 5539-5546.

(25) Cech, N. B.; Enke, C. G. Practical Implications of Some Recent Studies in Electrospray Ionization Fundamentals. *Mass Spectrom. Rev.* **2001**, *20*, 362-387.

(26) Tang, K.; Smith, R. D. Physical/Chemical Separations in the Break-up of Highly Charged Droplets from Electrosprays. *J. Am. Soc. Mass Spectrom.* **2001**, *12*, 343-347.

(27) Schmidt, A.; Karas, M.; Dülcks, T. Effect of Different Solution Flow Rates on Analyte Ion Signals in nano-ESI MS, or: When does ESI turn into nano-ESI? *J. Am. Soc. Mass Spectrom.* **2003**, *14*, 492-500.

(28) Benkestock, K.; Sundqvist, G.; Edlund, P.-O.; Roeraade, J. Influence of Droplet Size, Capillary-Cone Distance and Selected Instrumental Parameters for the Analysis of Noncovalent Protein-Ligand Complexes by nano-Electrospray Ionization Mass Spectrometry. *J. Mass Spectrom.* **2004**, *39*, 1059-1067.

(29) Rogers, R. D.; Seddon, K. R. Ionic Liquids - Solvents of the Future? *Science* **2003**, *302*, 792-793.

(30) Wasserscheid, P.; Keim, W. Ionic Liquids - New "Solutions" for Transition Metal Catalysis. *Angew. Chem., Int. Ed.* **2000**, *39*, 3772-3789.

(31) Welton, T. Room-Temperature Ionic Liquids. Solvents for Synthesis and Catalysis. *Chem. Rev.* **1999**, *99*, 2071-2083.

(32) *Ionic Liquids as Green Solvents: Progress and Prospects*; Rogers, R. D.; Seddon, K. R., Eds.; American Chemical Society Symposium Series 856; American Chemical Society; Distributed by Oxford University Press: Washington, DC; [Cary, N.C.], 2003.

(33) *Electrochemical Aspects of Ionic Liquids*; Ohno, H., Ed.; Wiley-Interscience: Hoboken, 2005.

(34) Cadena, C.; Anthony, J. L.; Shah, J. K.; Morrow, T. I.; Brennecke, J. F.; Maginn, E. J. Why Is CO_2 So Soluble in Imidazolium-Based Ionic Liquids? *J. Am. Chem. Soc.* **2004**, *126*, 5300-5308.

(35) Anthony, J. L.; Anderson, J. L.; Maginn, E. J.; Brennecke, J. F. Anion Effects on Gas Solubility in Ionic Liquids. *J. Phys. Chem. B* **2005**, *109*, 6366-6374.

(36) Huddleston, J. G.; Visser, A. E.; Reichert, W. M.; Willauer, H. D.; Broker, G. A.; Rogers, R. D. Characterization and Comparison of Hydrophilic and Hydrophobic Room

Temperature Ionic Liquids incorporating the Imidazolium Cation. *Green Chem.* **2001**, *3*, 156-164.

(37) Chen, Y.; Mutelet, F.; Jaubert, J.-N. Solubility of Carbon Dioxide, Nitrous Oxide, and Methane in Ionic Liquids at Pressures close to Atmospheric. *Fluid Phase Equilib.* **2014**, *372*, 26-33.

(38) Ficke, L. E.; Brennecke, J. F. Interactions of Ionic Liquids and Water. *J. Phys. Chem. B* **2010**, *114*, 10496-10501.

(39) Masaki, T.; Nishikawa, K.; Shirota, H. Microscopic Study of Ionic Liquid-H(2)O Systems: Alkyl-Group Dependence of 1-Alkyl-3-Methylimidazolium Cation. *J. Phys. Chem. B* **2010**, *114*, 6323-6331.

(40) Sun, B.; Wu, P. Trace of the Thermally Induced Evolution Mechanism of Interactions Between Water and Ionic Liquids. *J. Phys. Chem. B* **2010**, *114*, 9209-9219.

(41) Singh, T.; Kumar, A. Cation-Anion-Water Interactions in Aqueous Mixtures of Imidazolium Based Ionic Liquids. *Vib. Spectrosc.* **2011**, *55*, 119-125.

(42) Di Francesco, F.; Calisi, N.; Creatini, M.; Melai, B.; Salvo, P.; Chiappe, C. Water Sorption by Anhydrous Ionic Liquids. *Green Chem.* **2011**, *13*, 1712-1717.

(43) Maiti, A.; Rogers, R. D. A Correlation-Based Predictor for Pair-Association in Ionic Liquids. *Phys. Chem. Chem. Phys.* **2011**, *13*, 12138-12145.

(44) Hou, J.; Zhang, Z.; Madsen, L. A. Cation/Anion Associations in Ionic Liquids Modulated by Hydration and Ionic Medium. *J. Phys. Chem. B* **2011**, *115*, 4576-4582.

(45) Dupont, J. On the Solid, Liquid and Solution Structural Organization of Imidazolium Ionic Liquids. *J. Braz. Chem. Soc.* **2004**, *15*, 341-350.

(46) Freire, M. G.; Santos, L.; Fernandes, A. M.; Coutinho, J. A. P.; Marrucho, I. M. An Overview of the Mutual Solubilities of Water-Imidazolium-Based Ionic Liquids Systems. *Fluid Phase Equilib.* **2007**, *261*, 449-454.

(47) Tran, C. D.; Lacerda, S. H. D.; Oliveira, D. Absorption of Water by Room-Temperature Ionic Liquids: Effect of Anions on Concentration and State of Water. *Appl. Spectrosc.* **2003**, *57*, 152-157.

(48) Anthony, J. L.; Maginn, E. J.; Brennecke, J. F. Solution Thermodynamics of Imidazolium-Based Ionic Liquids and Water. *J. Phys. Chem. B* **2001**, *105*, 10942-10949.

(49) Cammarata, L.; Kazarian, S. G.; Salter, P. A.; Welton, T. Molecular States of Water in Room Temperature Ionic Liquids. *Phys. Chem. Chem. Phys.* **2001**, *3*, 5192-5200.

(50) Mele, A.; Tran, C. D.; Lacerda, S. H. D. The Structure of a Room-Temperature Ionic Liquid with and without Trace Amounts of Water: The Role of C-H···O and C-H···F Interactions in 1-*n*-Butyl-3-Methylimidazolium Tetrafluoroborate. *Angew. Chem., Int. Ed.* **2003**, *42*, 4364-4366.

(51) Saha, S.; Hamaguchi, H.-o. Effect of Water on the Molecular Structure and Arrangement of Nitrile-Functionalized Ionic Liquids. *J. Phys. Chem. B* **2006**, *110*, 2777-2781.

(52) Rodríguez, H.; Brennecke, J. F. Temperature and Composition Dependence of the Density and Viscosity of Binary Mixtures of Water + Ionic Liquid. *J. Chem. Eng. Data* **2006**, *51*, 2145-2155.

(53) Wang, Y.; Li, H.; Han, S. A Theoretical Investigation of the Interactions between Water Molecules and Ionic Liquids. *J. Phys. Chem. B* **2006**, *110*, 24646-24651.

(54) Rollet, A.-L.; Porion, P.; Vaultier, M.; Billard, I.; Deschamps, M.; Bessada, C.; Jouvensal, L. Anomalous Diffusion of Water in [BMIM][TFSI] Room-Temperature Ionic Liquid. *J. Phys. Chem. B* **2007**, *111*, 11888-11891.

(55) Jiang, W.; Wang, Y.; Voth, G. A. Molecular Dynamics Simulation of Nanostructural Organization in Ionic Liquid/Water Mixtures. *J. Phys. Chem. B* **2007**, *111*, 4812-4818.

(56) Schroder, C.; Rudas, T.; Neumayr, G.; Benkner, S.; Steinhauser, O. On the Collective Network of Ionic Liquid/Water Mixtures. I. Orientational Structure. *J. Chem. Phys.* **2007**, *127*, 234503.

(57) Fazio, B.; Triolo, A.; Di Marco, G. Local Organization of Water and its Effect on the Structural Heterogeneities in Room-Temperature Ionic Liquid/H_2O Mixtures. *J. Raman Spectrosc.* **2008**, *39*, 233-237.

(58) Moreno, M.; Castiglione, F.; Mele, A.; Pasqui, C.; Raos, G. Interaction of Water with the Model Ionic Liquid [bmim][BF_4]: Molecular Dynamics Simulations and Comparison with NMR Data. *J. Phys. Chem. B* **2008**, *112*, 7826-7836.

(59) Hanke, C. G.; Atamas, N. A.; Lynden-Bell, R. M. Solvation of Small Molecules in Imidazolium Ionic Liquids: A Simulation Study. *Green Chem.* **2002**, *4*, 107-111.

(60) Takamuku, T.; Kyoshoin, Y.; Shimomura, T.; Kittaka, S.; Yamaguchi, T. Effect of Water on Structure of Hydrophilic Imidazolium-Based Ionic Liquid. *J. Phys. Chem. B* **2009**, *113*, 10817-10824.

(61) Hanke, C. G.; Lynden-Bell, R. M. A Simulation Study of Water-Dialkylimidazolium Ionic Liquid Mixtures. *J. Phys. Chem. B* **2003**, *107*, 10873-10878.

(62) Fumino, K.; Wulf, A.; Ludwig, R. The Cation–Anion Interaction in Ionic Liquids Probed by Far-Infrared Spectroscopy. *Angew. Chem., Int. Ed.* **2008**, *47*, 3830-3834.

24

(63) Gao, Y.; Zhang, L.; Wang, Y.; Li, H. Probing Electron Density of H-Bonding between Cation-Anion of Imidazolium-Based Ionic Liquids with Different Anions by Vibrational Spectroscopy. *J. Phys. Chem. B* **2010**, *114*, 2828-2833.

(64) Cuadrado-Prado, S.; Dominguez-Perez, M.; Rilo, E.; Garcia-Garabal, S.; Segade, L.; Franjo, C.; Cabeza, O. Experimental Measurement of the Hygroscopic Grade on Eight Imidazolium Based Ionic Liquids. *Fluid Phase Equilib.* **2009**, *278*, 36-40.

(65) Dang, L. X.; Wick, C. D. Anion Effects on Interfacial Absorption of Gases in Ionic Liquids. A Molecular Dynamics Study. *J. Phys. Chem. B* **2011**, *115*, 6964-6970.

(66) Köddermann, T.; Wertz, C.; Heintz, A.; Ludwig, R. The Association of Water in Ionic Liquids: A Reliable Measure of Polarity. *Angew. Chem., Int. Ed.* **2006**, *45*, 3697-3702.

(67) Djikaev, Y. S.; Ruckenstein, E. A Kinetic Approach to the Theory of Heterogeneous Nucleation on Soluble Particles during the Deliquescence Stage. *J. Chem. Phys.* **2006**, *124*, 194709.

(68) Anthony, J. L.; Maginn, E. J.; Brennecke, J. F. Solubilities and Thermodynamic Properties of Gases in the Ionic liquid 1-n-Butyl-3-Methylimidazolium Hexafluorophosphate. *J. Phys. Chem. B* **2002**, *106*, 7315-7320.

(69) Blanchard, L. A.; Hancu, D.; Beckman, E. J.; Brennecke, J. F. Green Processing using Ionic Liquids and CO_2. *Nature* **1999**, *399*, 28-29.

(70) Finotello, A.; Bara, J. E.; Camper, D.; Noble, R. D. Room-Temperature Ionic Liquids: Temperature Dependence of Gas Solubility Selectivity. *Ind. Eng. Chem. Res.* **2008**, *47*, 3453-3459.

(71) Brennecke, J. F.; Maginn, E. J. Ionic liquids: Innovative Fluids for Chemical Processing. *Aiche J.* **2001**, *47*, 2384-2389.

(72) Hamilton, J. F.; Rami Alfarra, M.; Wyche, K. P.; Ward, M. W.; Lewis, A. C.; McFiggans, G. B.; Good, N.; Monks, P. S.; Carr, T.; White, I. R.; Purvis, R. M. Investigating the Use of Secondary Organic Aerosol as Seed Particles in Simulation Chamber Experiments. *Atmos. Chem. Phys.* **2011**, *11*, 5917-5929.

(73) Liggio, J.; Li, S. M. Reversible and Irreversible Processing of Biogenic Olefins on Acidic Aerosols. *Atmos. Chem. Phys.* **2008**, *8*, 2039-2055.

(74) Chu, B.; Jiang, J.; Lu, Z.; Wang, K.; Li, J.; Hao, J. Effects of Inorganic Seeds on Secondary Organic Aerosol (SOA) Formation. *Atmos. Aerosol. - Regional Characteristics - Chem. Phys.* [Open Access Journal] **2012**, 347-362. DOI: 10.5772/48424.

(75) Jang, M.; Czoschke, N. M.; Lee, S.; Kamens, R. M. Heterogeneous Atmospheric Aerosol Production by Acid-Catalyzed Particle-Phase Reactions. *Science* **2002**, *298*, 814-817.

(76) Iinuma, Y.; Müller, C.; Böge, O.; Gnauk, T.; Herrmann, H. The Formation of Organic Sulfate Esters in the Limonene Ozonolysis Secondary Organic Aerosol (SOA) Under Acidic Conditions. *Atmos. Environ.* **2007**, *41*, 5571-5583.

(77) Czoschke, N. M.; Jang, M.; Kamens, R. M. Effect of Acidic Seed on Biogenic Secondary Organic Aerosol Growth. *Atmos. Environ.* **2003**, *37*, 4287-4299.

Chapter 2: Experimental and Computational Methods

2.1. Introduction

This chapter describes the experimental and computational techniques used for the projects discussed in this dissertation.

2.2. Materials

2.2.1. Materials Used in Chapter 3

All chemicals were purchased and their sources and purities were as follows: sodium dodecyl sulfate (SDS) (Fluka, $\geq$ 99.0%), sodium chloride (NaCl) (Sigma-Aldrich, 99.999%), HPLC grade water (OmniSolv, < 8 $\mu\Omega$ cm), and methanol (MeOH) (Sigma-Aldrich, HPLC grade). The structure of SDS is shown in Figure 2.1.
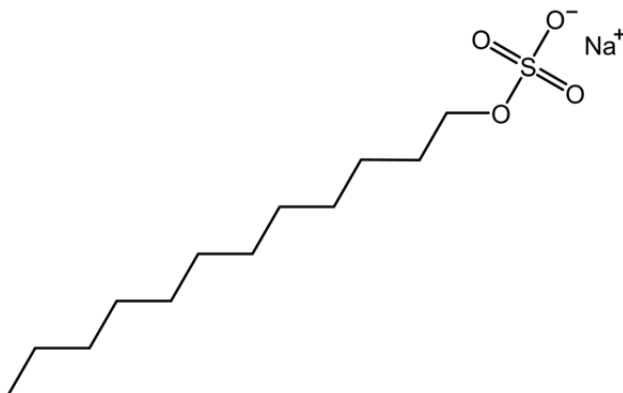
Figure 2.1. Structure of sodium dodecyl sulfate (SDS).

2.2.2. Materials Used in Chapters 4–7

The sources and purities of the ionic liquids (ILs) used in Chapter 4 were as follows: 1-ethyl-3-methylimidazolium chloride ([C$_2$MIM][Cl]) (Aldrich, 98%) and 1-ethyl-3-

methylimidazolium tetrafluoroborate ([C$_2$MIM][BF$_4$]) (Aldrich, 98%). Their chemical structures are shown in Figure 2.2.
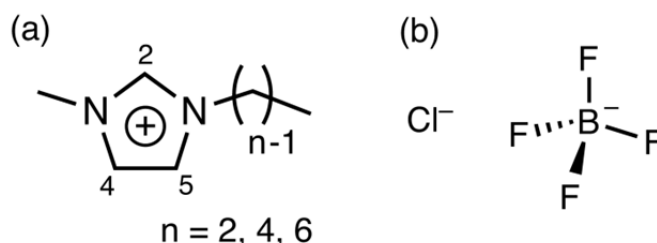
Figure 2.2. Ionic liquids used in the hygroscopicity studies: (a) 1-*n*-alkyl-3-methylimidazolium ([C$_n$MIM]$^+$) cations with varying linear alkyl chain lengths (*n* = 2, 4, or 6) were paired with either (b) a chloride (Cl$^-$) or tetrafluoroborate (BF$_4^-$) anion.

Chapter 5 examined ILs containing [C$_n$MIM]$^+$ (1-*n*-alkyl-3-methylimidazolium) cations with varying linear alkyl chain lengths (*n* = 4 or 6) (Figure 2.2) that were paired with either chloride (Cl$^-$) or tetrafluoroborate (BF$_4^-$) anions (Figure 2.2). All ILs were purchased and their source and purity were as follows: 1-butyl-3-methylimidazolium chloride ([C$_4$MIM][Cl]) (Aldrich, 98%), 1-hexyl-3-methylimidazolium chloride ([C$_6$MIM][Cl]) (IoLiTec, 98%), 1-butyl-3-methylimidazolium BF$_4$ ([C$_4$MIM][BF$_4$]) (Aldrich, 98%), and 1-hexyl-3-methylimidazolium BF$_4$ ([C$_6$MIM][BF$_4$]) (IoLiTec, 99%).

The IL solutions used in Chapter 4 and 5 for the hygroscopicity measurements were prepared by dissolving the ILs in anhydrous MeOH to reach the desired IL solution concentration. Anhydrous MeOH was prepared by sparging with argon and then dried with columns containing Q-5 (supported redox catalyst to remove dioxygen) and molecular sieves.

To study the uptake of carbon dioxide (CO_2) (99.99%, Airgas) by aerosolized ILs, as described in Chapter 6, the IL 1-ethyl-3-methylimidazolium bis(trifluoromethylsulfonyl)imide ([C_2MIM][Tf_2N]) (IoLiTec, 99%) was used. The chemical structure for [C_2MIM][Tf_2N] is shown in Figure 2.3. Aerosolized ammonium sulfate ((NH_4)$_2SO_4$) (Sigma-Aldrich, 99.999%) was used as the control. Solutions were prepared in MeOH (Fisher, HPLC grade).
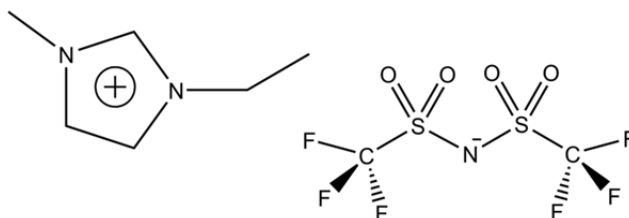
Figure 2.3. Structure of the ionic liquid, 1-ethyl-3-methylimidazolium bis(trifluoromethylsulfonyl)imide ([C_2MIM][Tf_2N]), used to study CO_2 uptake.

In Chapter 7, the use of ILs as suitable seed particles for secondary organic aerosol (SOA) formation was studied. The sources and purities of those ILs are as follows: [C_6MIM][BF_4] (IoLiTec, 99%) (Figure 2.2), [C_2MIM][Tf_2N] (IoLiTec, 99%) (Figure 2.3), and 1-ethyl-3-methylimidazolium dicyanamide ([C_2MIM][dca]) (IoLiTec, > 98%) (Figure 2.4). Aerosolized poly(ethylene) glycol (PEG) (Acros Organics, ACS grade) was used was used as the control. SOA was formed by oxidation of α-pinene (Acros Organics, 98%) with ozone (O_3) (UHP, 99.999%, Airgas).
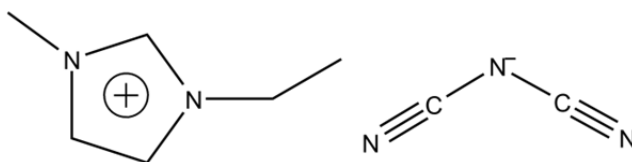
Figure 2.4. Structure of the ionic liquid, 1-ethyl-3-methylimidazolium dicyanamide ([C$_2$MIM][dca]), used to in Chapter 7 as a suitable seed particle for secondary organic aerosol formation and growth.

To keep the ILs free of water during preparation, all samples were prepared in a drybox that was continuously purged with dry air. After preparation, all chemicals were sealed with paraffin film and stored in a desiccator when not in use. To prevent potential photodegradation, glassware used for purification and drying of [C$_2$MIM][BF$_4$], [C$_4$MIM][BF$_4$], and [C$_6$MIM][BF$_4$] was wrapped in foil. In addition, the pure chemicals and prepared solutions were stored in amber vials.

2.3. Ionic Liquid Purification

ILs used in Chapters 4 and 5 were purified and dried before all experiments using standard literature techniques.[1–4] [C$_2$MIM][Cl], [C$_4$MIM][Cl], and [C$_6$MIM][Cl] were washed several times with ethyl acetate (Acros Organics, 99.5% Spectroscopy grade) and dried under rough vacuum (2–3 Torr) at ~ 363 K for 48 h.[2–4] [C$_2$MIM][BF$_4$], [C$_4$MIM][BF$_4$], and [C$_6$MIM][BF$_4$] were stirred with activated carbon (Sigma-Aldrich, 20–40 mesh) for 12 h, filtered with a short column of neutral, activated alumina (Fisher, 60–325 mesh), and dried under rough vacuum (2–3 Torr) at ~ 343 K for 48 h.[1,4] [C$_2$MIM][Tf$_2$N], used in Chapter 6 and 7, and

[C$_2$MIM][dca], used in Chapter 7, were used as is. The [C$_6$MIM][BF$_4$], used in Chapter 7, was not purified and dried and was used as is.

2.4. Ionic Liquid ^{1}H Nuclear Magnetic Resonance Spectroscopy

Once the ILs that were purified and dried, their purities were verified before and after purification and drying with ^{1}H nuclear magnetic resonance spectroscopy, using a Bruker DRX500 equipped with a TCI cryoprobe at 298 K using acetone-d_6 (Cambridge Isotope Laboratories, Inc.; D, 99.9%, with 1% v/v TMS) as the solvent.

2.5. Ionic Liquid Water Content

After vacuum drying, the amount of water left in the ILs was measured using a Karl Fischer titrator (Mettler Toledo, Model DL39) with analyte hydranal coulomat A and catholyte hydranal coulomat CG (both from Fluka). For [C$_2$MIM][Cl], [C$_4$MIM][Cl], and [C$_6$MIM][Cl], a solution was prepared by diluting ~ 0.6 g of the IL into ~ 1 mL of anhydrous MeOH, prepared as described in Section 2.2.2. For [C$_2$MIM][BF$_4$], [C$_4$MIM][BF$_4$], and [C$_6$MIM][BF$_4$], neat samples were examined. The water contents of [C$_2$MIM][Cl], [C$_4$MIM][Cl], [C$_6$MIM][Cl], [C$_2$MIM][BF$_4$], [C$_4$MIM][BF$_4$], and [C$_6$MIM][BF$_4$], averaged over 3–4 measurements of the solutions and neat samples, were approximately 390, 526, 278, 120, 99, and 168 ppm, respectively, by mass. The water content of the anhydrous MeOH solvent was ~ 180 ppm using Karl Fischer titration.

2.6. Nanoparticle Generation for Electrospray

2.6.1. NaCl and SDS/NaCl Nanoparticle Generation

SDS/NaCl solution for electrospray, as discussed in Chapter 3, was prepared using NaCl and SDS dissolved in HPLC grade water, with a small volume (< 5%) of MeOH to stabilize the electrospray cone. The solute consisted of 10.7 wt% SDS and 89.3 wt% NaCl (solute molar fractions of 0.0237 and 0.976, respectively). The combined SDS + NaCl weight concentration in the solution was 2.1 g L^{-1}, resulting in solution concentrations of SDS and NaCl of 0.78 mM and 32 mM, respectively. The electrosprayed solution of pure NaCl was prepared by dilution of NaCl in HPLC grade water and a small volume (< 5%) of MeOH. SDS and NaCl are both soluble in water and have solubility values of 150 and 359 g L^{-1}, respectively. SDS is capable of forming micelles; however, its critical micelle concentration is 8.2 mM at 298 K. Therefore, no micelles are expected in the initial solution used in the experiments.

Nanoparticles were generated using a custom-built electrospray aerosol generator (EAG).[5,6] Using a syringe pump, solutions were pushed through a capillary tube (360 μm outer diameter (o.d.), 100 μm inner diameter (i.d.)) at a rate of ~ 80 μL h^{-1} at 295 K. The capillary was housed in a 5 cm^3 chamber, with transparent windows to allow for viewing the electrospray (Figure 2.5a). A positive potential (~ 4 kV) was applied to the capillary to produce a stable cone-jet. The spray was carried by a ~ 1 SLM (standard liter per minute) flow of dry air towards the entrance of an electrically-grounded neutralizer ([85]Kr, 10 mCi, TSI, Model 3077A, 6.4 mm o.d., 4.8 mm i.d.). The distance from the capillary tip to the entrance of the neutralizer (l_s) was varied from 4 mm to 10 mm in approximately 0.3 mm increments with a linear translation stage. After exiting the neutralizer, the number concentrations of polydisperse nanoparticles were typically in excess of 10^5 particles cm^{-3}.
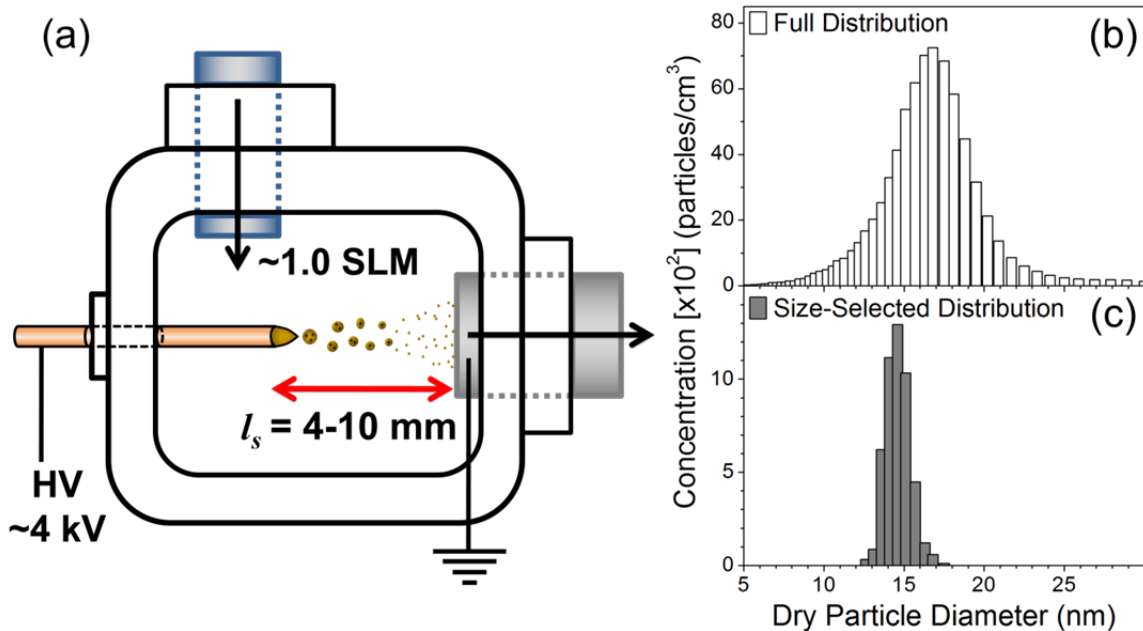
Figure 2.5. (a) Schematic diagram of the electrospray housing chamber. An SDS/NaCl solution is pushed through a capillary and electrosprayed. Droplets are carried toward the neutralizer opening (dark grey cylinder on right) with a flow of dry air. The double-sided arrow indicates the capillary tip to neutralizer distance (l_s), which is varied in the experiments. (b) Full particle mobility-equivalent size distribution of the SDS/NaCl particles measured by the first nano-DMA and (c) after size selection for 14.5 nm SDS/NaCl particles using the second nano-DMA.

2.6.2. Ionic Liquid Nanoparticle Generation

IL solutions used for hygroscopic growth measurements were prepared by dilution of the purified and dried IL, as described above, in anhydrous MeOH to reach a final solution concentration of ~ 0.5–0.6 g L^{-1}. The [C$_2$MIM][Tf$_2$N] IL solution used for CO$_2$ uptake measurements in Chapter 6 was prepared by dissolving [C$_2$MIM][Tf$_2$N] in MeOH (Fisher, HPLC grade) to reach a final solution concentration of 1.2 g L^{-1}. All IL solutions were stored in dark, amber vials that were closed with septum caps, sealed with a paraffin film, and stored in a

desiccator when not in use. Additionally, a solution of $(NH_4)_2SO_4$, the CO_2 uptake study control, was prepared by dissolving $(NH_4)_2SO_4$ in MeOH (Fisher, HPLC grade) to reach a final solution concentration of 1.1 g L^{-1}.

Solutions were electrosprayed (at 295 K and 1 atm) using a custom-built EAG, as described above. Solutions were withdrawn from the vial directly using a syringe (Hamilton GT, 1 mL) to avoid water uptake from the atmosphere. A syringe pump (KD Scientific, Model 780100), with a flow rate of 0.15 mL h^{-1}, was used to push the solutions through a 5 cm long, quartz capillary tube (i.d. 100 μm, o.d. 360 μm).

The capillary was housed in a 5 cm^3 chamber that was equipped with glass windows, a microscope objective, and a CCD camera for viewing the spray (Figure 2.6a,b). A stable cone-jet (Taylor cone) of the solution was generated by applying a ~ 3 kV potential directly to the stainless steel union, which connected the capillary and syringe. The capillary tip was positioned ~ 7–8 mm away from a bipolar neutralizer (either [85]Kr 10 mCi TSI, Model 3077A or [210]Po 10 mCi NRD, Model P-2021).

Nanoparticles were carried with a flow of dry air (< 1% relative humitidy, RH), at a flow rate of ~ 0.8 SLM, toward the electrically grounded neutralizer opening. The EAG was operated continuously and generated a dry, polydisperse number concentration of particles on the order of 10^5 particles cm^{-3}, with sizes ranging from ~ 5 to 55 nm for the hygroscopic growth measurements (Figure 2.6c). The narrow size distribution of particles was selected from this polydisperse population of particles (Figure 2.6d).
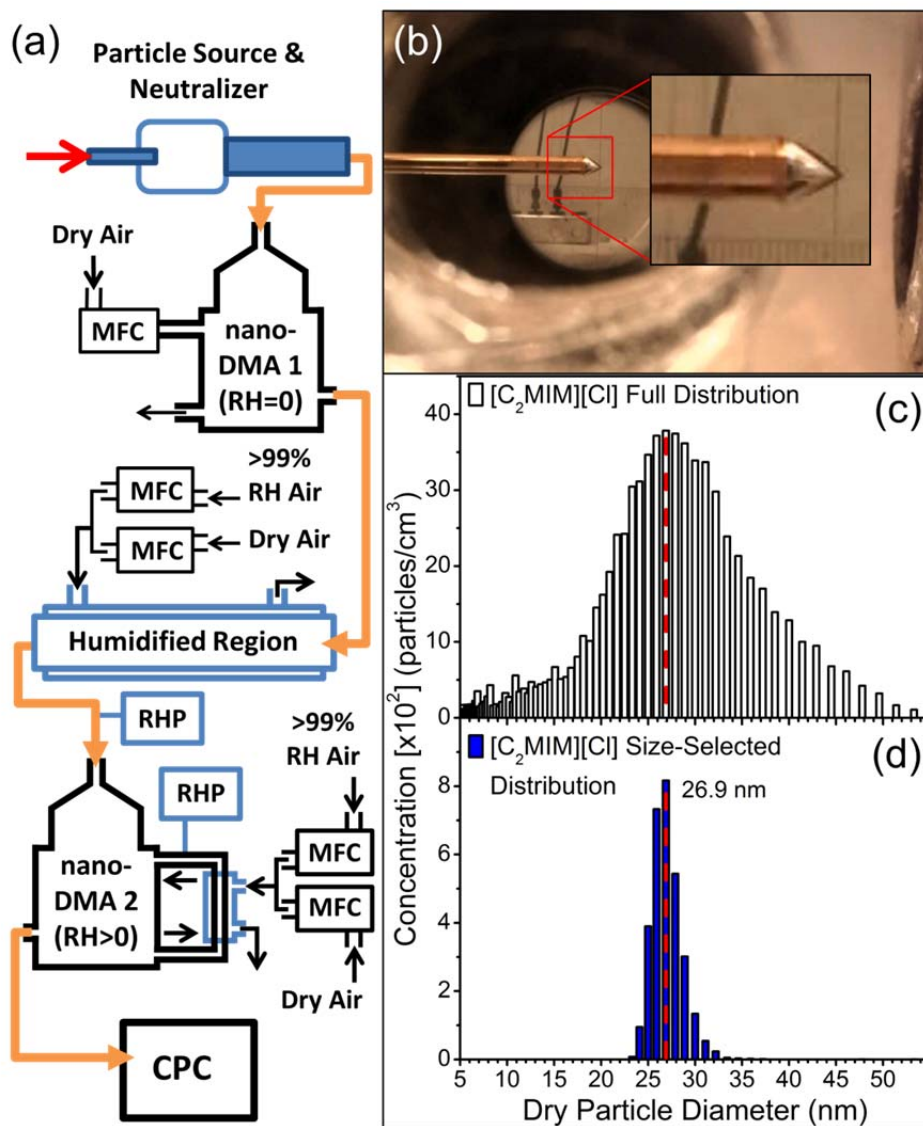
Figure 2.6. (a) Schematic diagram of the apparatus used for ionic liquid nanoparticle hygroscopic growth measurements. Key: DMA, differential mobility analyzer; RHP, relative humidity probe; CPC, condensation particle counter; MFC, mass flow controller. (b) An image of the Taylor cone for an electrosprayed solution of $[C_2MIM][Cl]$ with an inset, magnified image of the quartz capillary tube (o.d. 360 μm) and Taylor cone. (c) Full particle mobility size distribution of the dry $[C_2MIM][Cl]$ particles measured by DMA1. (d) The mobility size distribution after size selection for 26.9 ± 0.01) nm $[C_2MIM][Cl]$ particles measured by DMA2. The red, dotted line in panels c and d indicates where the dry particle distributions were centered (at 26.9 nm).

For the hygroscopic growth studies, the particles' sizes are considerably larger than the 1–7 nm IL nanodroplets investigated by de la Mora and co-workers,[7–10] which were also generated by an electrospray method. The differences in the observed particles' size distributions were likely due to the significantly different EAG operation conditions. The IL particles produced in the de la Mora experiments were not neutralized immediately after the electrospray process, making them more susceptible to Coulomb fission. Prompt neutralization in the present experiments effectively removed charge from the primary droplets to prevent them from fissioning into smaller progeny droplets, resulting in larger residue particles.

2.7. Hygroscopic Growth Measurements

2.7.1. NaCl and SDS/NaCl Hygroscopic Growth Measurements

Nanoparticles were size selected and their hygroscopic growth factors (GFs) were measured using hygroscopicity tandem nano-differential mobility analysis (TDMA).[11] The initial dry mobility-equivalent diameter was selected using the first nano-differential mobility analyzer (nano-DMA1, TSI, Model 3085) operated under dry conditions (RH < 1%). A fixed DC voltage was applied to nano-DMA1 in order to select a narrow distribution of mobility-equivalent diameter $(d_{m,dry})$ = 14.5 ± 0.1 nm (with a geometric standard deviation of ~ 1.06). This particular size was chosen because it was near the peak of the full size-distribution for the particles generated by the EAG, thus maximizing the particle count. The selected particles were then passed through a humidifier (90% RH) and entered the second nano-DMA (nano-DMA2, TSI, Model 3085) for sizing. The sheath flow of nano-DMA2 was also humidified to 90% RH. Following the particle mobility-equivalent diameter measurements with nano-DMA2, the

37

particles were detected with an ultrafine condensation particle counter (CPC; TSI, Model 3025A).

Nano-DMA2 was operated in a scanning mobility particle sizer (SMPS) mode, wherein the voltage applied to the central rod was scanned using an Electrostatic Classifier (EC; TSI, Model 3080) controlled by TSI Aerosol Instrument Manager (AIM) software (version 9.0). We should note that the assumptions made by the data inversion algorithms used by the SMPS software may lead to inaccurate results for sizing particles in TDMA experiments. As discussed by Rader and McMurry,[11] in cases where the particle number concentration changes significantly over the size range transmitted by the fixed-voltage nano-DMA1, the peak in the particles' size distribution measured by the nano-DMA2 will be shifted from the actual average size of the particles. A proper way to correct for these effects is to use a data inversion algorithm designed specifically for TDMA[11], such as TDMAFIT[12]. However, one can also minimize these effects by size-selecting particles with DMA1 close to the peak of the initial full size distribution produced by the EAG. In the experiments described in this work, we adopted the latter approach. While the absolute GF values may be slightly off, the change in GF measured in this way should be reasonably accurate.

2.7.2. Ionic Liquid Hygroscopic Growth Measurements

IL nanoparticle hygroscopicity was determined using a similar TDMA system as described above. The experimental schematic is shown in Figure 2.6a. Under dry conditions (< 1% RH), a narrow size distribution of nanoparticles was selected by applying a fixed negative dc potential (~ -320 V) to nano-DMA1. Dry IL particles with mobility-equivalent diameters centered at 26.9 ± 0.1 nm were selected with geometric standard deviations of ~ 1.06 (the stated

uncertainty of ± 0.1 nm refers to the reproducibility of the average diameter, not to the width of the size-selected distribution, which was ~ 4 nm fwhm).

As demonstrated by Rader and McMurry, the interpretation of TDMA measurements is simplified considerably if the particle number concentrations do not vary significantly over the size selection window of nano-DMA1.[11] The size of 26.9 nm was specifically chosen because it neared the maximum of the full size distribution for the particles generated by the EAG, thus maximizing the particle count (Figure 2.6c,d) and minimizing the variation in the particle number concentrations across the nano-DMA1 selection window. While the initial particle size selected in this work was fixed, it would be interesting to conduct similar experiments with variable particle sizes in the future, especially in the sub-10 nm size range, where significant size-effects on hygroscopicity can be expected.

Dry IL nanoparticles were then exposed to humidified air by sending them through a Nafion tube (PermaPure). Controlled humid air flowing around the Nafion tube provided the source of RH. RH was maintained by mixing different proportions of wet (RH > 99%) and dry (RH < 1%) air. RH and temperature were monitored using Vaisala HMP237 RH probes and a LabVIEW program. The probe humidity accuracy was ± 2% RH (0–90% RH) and ± 3% RH (90–100% RH), while the precision was about ± 0.1% RH. Each probe was calibrated by taking measurements over saturated solutions of $MgCl_2$, NaCl, and K_2SO_4, with a second- or third-order polynomial fit used to interpolate the dependence of the probe response on RH. After particles exited the humidified region, nano-DMA2 was used to measure the particle size distribution of the wet particle size. nano-DMA2 was operated in a SMPS mode, wherein the potential applied to the central rod was scanned using an EC controlled by TSI AIM software (version 9.0). A CPC (TSI, Model 3025A) was used to detect particles from either nano-DMA.

2.8. CO$_2$ Sequestration in Aerosolized Ionic Liquid Nanoparticles

The ability of ILs to uptake CO$_2$ was determined by TDMA measurements. For these experiments, the TDMA setup used for the hygroscopicity experiments, as described above, underwent several modifications to allow for introduction of CO$_2$ into the system instead of water vapor. The TDMA setup used for hygroscopicity measurements required the addition of a humidified region (Figure 2.6a), located between nano-DMA1 and nano-DMA2, to allow for nanoparticles to be exposed to a controlled RH. The humidified region, itself, consisted of several components including nafion, nafion dryers, RH and temperature probes, several MFCs, a multi gas controller (MKS, Model 647C), and lots of tubing.

For the TDMA system used for CO$_2$ uptake measurements, the humidified region was replaced by a "100% CO$_2$ Region" (Figure 2.7). For the preliminary studies of IL–CO$_2$ uptake, only 100% CO$_2$ was used and the gas flow was controlled by a MFC located between the CO$_2$ tank and the 100% CO$_2$ Region. In future experiments, where the levels of CO$_2$ are varied, more MFCs would be added to control the mixing ratios of CO$_2$ and dry air inside the CO$_2$ Region. The amount of CO$_2$ in nano-DMA2 would be controlled by the CO$_2$ Region and the EC. No CO$_2$ probes were used for the preliminary 100% CO$_2$ experiments. In future experiments, when CO$_2$ levels are varied and exact CO$_2$ values would be needed, CO$_2$ probes would be added to the setup to monitor CO$_2$ levels inside the CO$_2$ region and nano-DMA2. The CO$_2$ from the tank was filtered with a HEPA filter before it entered the CO$_2$ region.
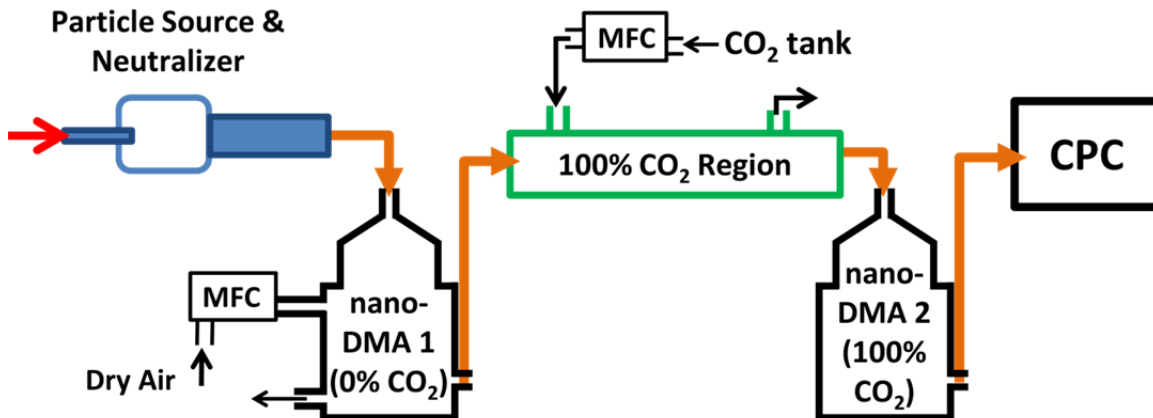
Figure 2.7. Schematic diagram of the apparatus used for ionic liquid and $(NH_4)_2SO_4$ nanoparticle CO_2 uptake measurements. Key: DMA, differential mobility analyzer; CPC, condensation particle counter; MFC, mass flow controller.

IL nanoparticles were generated as described above in Section 2.6.2. Under dry, 0% CO_2 conditions, a narrow size distribution of $[C_2MIM][Tf_2N]$ or $(NH_4)_2SO_4$ nanoparticles was selected by applying a fixed negative dc potential (~ -450 V) to nano-DMA1. Dry $[C_2MIM][Tf_2N]$ IL nanoparticles with a mobility-equivalent diameter centered at 31.1 ± 0.1 nm were selected with a geometric standard deviation of ~ 1.06 (the stated uncertainty of ± 0.1 nm refers to the reproducibility of the average diameter, not to the width of the size-selected distribution, which was ~ 4 nm fwhm). Additionally, $(NH_4)_2SO_4$ nanoparticles with a mobility-equivalent diameter centered at 30.9 ± 0.2 nm were selected with geometric standard deviations of ~ 1.06.

Dry nanoparticles were then exposed to 100% CO_2 by sending them through a stainless steel tube saturated with CO_2 (i.e., the CO_2 Region). After particles exited the 100% CO_2

Region, nano-DMA2 was used to measure the particle size distribution after exposure to 100% CO_2. nano-DMA2 was operated in SMPS mode, wherein the potential applied to the central rod was scanned using an EC controlled by TSI AIM software (version 9.0). A CPC (TSI, Model 3025A) was used to detect particles from either nano-DMA.

2.9. Ionic Liquids as Suitable Seed Particles for Secondary Organic Aerosol Formation and Growth

2.9.1. Solution Preparation for Atomization

Use of ILs as suitable seed particles for SOA growth and formation was investigated using the ILs [C_6MIM][BF_4], [C_2MIM][Tf_2N], and [C_2MIM][dca] (Figures 2.2, 2.3, and 2.4, respectively). For the experiments where seed particles were not size-selected, solutions of ILs were prepared by dissolving the ILs in MeOH (Fisher, HPLC grade) to reach final solution concentrations of ~ 1 g L^{-1}. A solution of the control seed, PEG, was made by dissolving PEG in MeOH to match the concentration of the IL solutions used (1 g L^{-1}). For the size selection experiments, the concentrations of ILs' solutions (dissolved in MeOH) ranged from ~ 1–50 g L^{-1}.

2.9.2. Ionic Liquid Seed Particle Atomization

To use our laboratory's large 5 m^3 environmental smog chamber to study ILs as suitable seed particles for SOA formation and growth, the experiments were first optimized in our small 1 m^3 smog chamber (Figure 2.8). This allowed us to determine the correct solution concentrations, atomizer flow rates, and atomizer atomization times needed to obtain, by extrapolating the 1 m^3 chamber results, the desired seed particle concentrations in our 5 m^3 smog chamber.

42
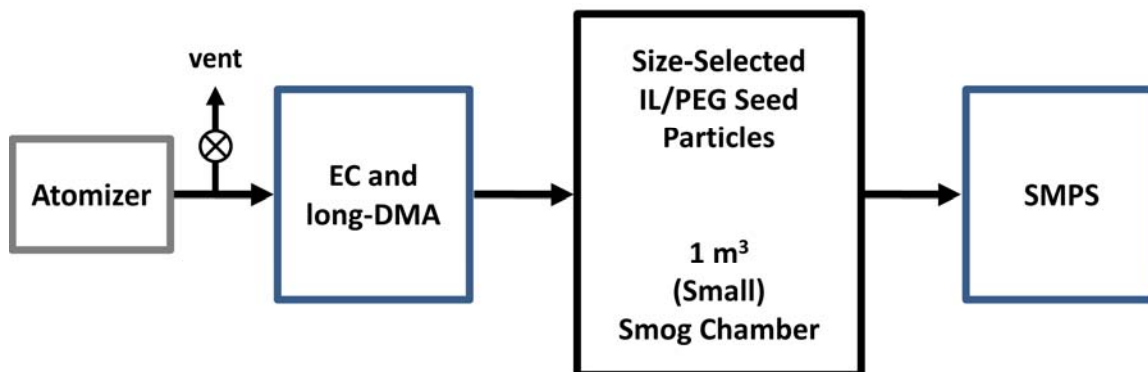
Figure 2.8. Schematic diagram of the small 1 m³ smog chamber experimental setup to study ionic liquids' suitability as a seed particle for secondary organic aerosol formation and growth. Key: EC, electrostatic classifier; long-DMA, long differential mobility analyzer; SMPS, scanning mobility particle sizer.

Seed particles were generated by atomizing solutions using a constant output atomizer (TSI, Model 3076) with a flow of dry air. Seed particles were not dried prior to entering either the small or large smog chamber. The small 1 m³ smog chamber consisted of a ~ 2 cm thick, hollow Plexiglas cylinder fitted with two capped ends. The cylinder's bottom cap was fitted with a computer fan attached inside the cylinder to allow for aerosol mixing inside the small chamber. The cylinder's top cap was fitted with several ports to allow for introduction and sampling of the various IL seed particles used in this study (Figure 2.8). For the experiments where particles were not size-selected, several solution concentrations were tested in the small smog chamber to obtain the desired initial seed particle mass concentration in our large 5 m³ smog chamber (i.e., 100–150 μg m⁻³). The best solution concentration for this particle mass concentration was ~ 1 g L⁻¹. It is worth noting that mass concentrations other than 100–150 μg m⁻³ can be studied,

specifically lower concentrations. This higher concentration range was chosen because, if the preliminary results looked interesting, the SOA generated in future studies would be collected on filters and analyzed with a high-resolution mass spectrometer.

The large smog chamber consisted of a 5 m^3 Teflon bag enclosed in a UV resistant black box (Figure 2.9). After introduction into the large chamber, the seed particles were allowed to stabilize for 1 h. For the experiments where seed particles were not size-selected, all four seed particle mass concentrations were ~ 150 μg m^{-3} before adding O$_3$. After the seed particles' concentrations stabilized, 600 ppb O$_3$, to be in excess of the seed mass concentration (i.e., two times higher), was introduced into the chamber and allowed to equilibrate for 1 h before addition of the organic precursor. For experiments where seed particles were size-selected, the seed particle mass concentrations ranged from 3–115 μg m^{-3}. In the size selection experiments, the amount of O$_3$ added was determined by multiplying the estimated α-pinene mixing ratio by five. The RH and temperature were monitored with a RH probe (Vaisala, Model HMT333). O$_3$ was monitored using an O$_3$ analyzer (Thermo Scientific, Model 49i). All materials were thoroughly mixed inside the large chamber using a small fan.
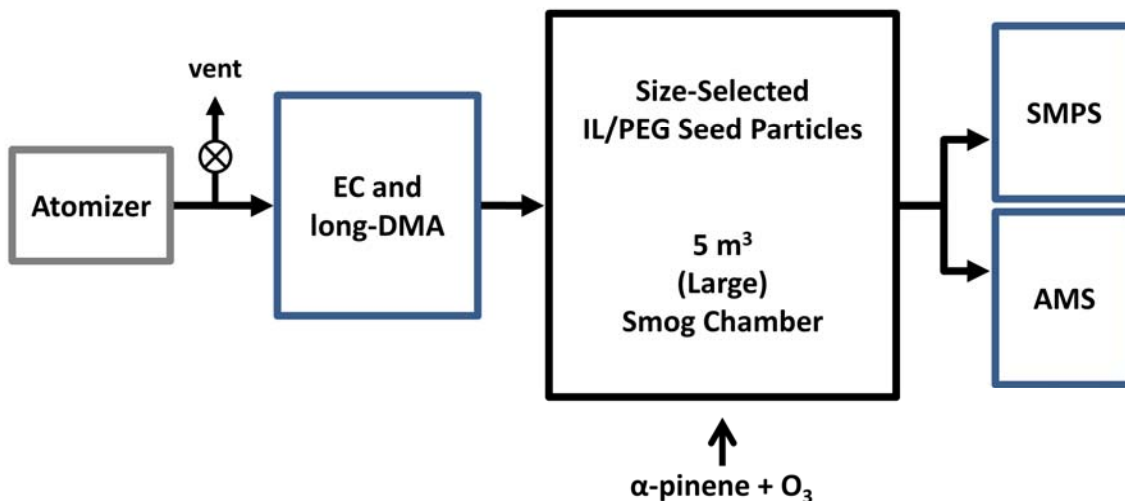
Figure 2.9. Schematic diagram of the large 5 m^3 smog chamber experimental setup to study ionic liquids' suitability as a seed particle for secondary organic aerosol formation and growth. Key: EC, electrostatic classifier; long-DMA, long differential mobility analyzer; SMPS, scanning mobility particle sizer; AMS, aerosol mass spectrometer.

2.9.3. Secondary Organic Aerosol Formation and Growth

Initial experimental runs in the large 5 m^3 smog chamber to test ILs as suitable seed particles for SOA formation and growth did not size-select the atomized IL seed particles. The full particle size distributions were atomized directly into the large chamber, thus the EC and long-DMA between the atomizer and smog chamber were not utilized (Figure 2.9). Later experiments were performed where IL seed particles were size-selected before entering either chamber, as shown in Figure 2.9.   The solutions were atomized and sent through an additional EC (TSI, Model 3080) and long-DMA (TSI, Model 3081), set to a fixed voltage, that size-selected for the seed particle size desired in the chamber.

When size-selecting, a portion of the aerosolized seed particles was vented before

entering the EC. This was done to maintain the aerosol flow inside the EC (i.e., 0.3 or 1.5 SLM)

(Figure 2.9). Initial attempts at size-selecting atomized seed particles used a Sheath to Aerosol

flow ratio of 3.0:0.3 SLM inside the EC. Though, this resulted in very low seed particle mass

concentrations. Additional studies, to increase atomizer seed particle concentrations, were

performed testing a higher Sheath to Aerosol flow ratio of 15:1.5 SLM inside the EC.

For the experiments where seed particles were not size-selected, after seed particles and

O_3 were introduced and well-mixed, ~ 2 µL of α-pinene was added (to obtain a 1:1 seed to

hydrocarbon ratio) and the reaction was allowed to commence for ~ 3 h. For size selection

experiments where seed particles were size-selected, the amount of α-pinene added was

determined by multiplying the initial seed particle mass concentration by ten. This was done to

ensure enough SOA would be generated for filter collection and further analysis.

The SOA particles' number and mass concentrations were measured using an EC (TSI,

Model 3080), long-DMA (TSI, Model 3081), and CPC (TSI, Model 3775). The EC and long-

DMA, set to SMPS mode, scanned the full range of voltages. SOA particle composition in the

large 5 m^3 chamber was monitored with a high-resolution time-of-flight aerosol mass

spectrometer. All experiments were done in darkness, in the absence of any UV light.

2.10. Attenuated Total Reflection Crystals

For the hygroscopicity attenuated total reflection Fourier transform infrared (ATR-FTIR)

spectroscopy measurements, zinc selenide (ZnSe) ATR crystals (80 mm × 10 mm × 4 mm, Pike

Technologies or Balboa Scientific) were used as received. The crystals were optimized for 10

internal reflections along the length of the crystal. Prior to each use, the ATR crystals were

cleaned by sequential sonication in ethanol (EMD, OmniSolv, 99.99%) and acetone (EMD, OmniSolv, 99.84%). To remove any trace organics that remained, the ATR crystal was placed in an argon plasma discharge (Harrick Plasma Cleaner/Sterilizer PDC-32G, low or medium power, Harrick Scientific Products, Inc.) for ~ 30 min, rinsed with ultrapure (Milli-Q) water (18 MΩ cm), and dried with nitrogen (UHP, 99.999%, Oxygen Services).

2.11. Fourier Transform Infrared Spectroscopy Measurements

For the hygroscopicity ATR-FTIR measurements, solutions for FTIR were prepared by dissolving the purified and dried ILs in anhydrous MeOH (final solution concentration of ~ 0.5–0.6 g L^{-1}; to resemble the solutions used for electrospray), ultrapure water, or a mixture of ultrapure water in excess D_2O (H_2O/D_2O). H_2O/D_2O solutions, as described in Smith et al.,[13] [13] were prepared using ultrapure water and D_2O (Cambridge Isotope Laboratories, Inc., 99.96%). IL–water and IL–H_2O/D_2O solutions were prepared in 1:1 molar ratios. Thin films of purified ILs (neat or in MeOH, water, or H_2O/D_2O solutions) were applied to clean ZnSe ATR substrates by drop deposition. In some cases, aliquots of the final solutions were sprayed onto the clean ATR crystal using a small nebulizer (artist's airbrush), as previously described.[14,15]

The IL-coated ATR crystal was immediately placed into a trough plate flow-through multiple reflection horizontal ATR cell (Pike Technologies) situated in the platform optics assembly within the sampling compartment of the FTIR spectrometer. A flow of dry nitrogen (UHP) was introduced into the ATR cell overnight to drive off the solvent and water absorbed during film preparation.

IR spectra were acquired using a Nicolet 6700 FTIR spectrometer (now Thermo Electron Corporation) equipped with a KBr beam splitter and a high-temperature ceramic source. FTIR

spectra were acquired as single beams at 4 cm^{-1} resolution with a liquid nitrogen-cooled mercury cadmium telluride detector (MCT-A). A background scan was recorded under the condition of dried flow, described above, for both ILs. The extent of water uptake was monitored using ATR-FTIR. Thin films of [C$_2$MIM][Cl] and [C$_2$MIM][BF$_4$] were exposed to water vapor in the ATR cell as a function of RH at 295 K (Figure 2.10). The spectra were calculated as –log (S/S_0), where S_0 is the single beam intensity of the clean ZnSe ATR crystal and S is that of the dry IL. For humidified spectra, the RH inside the ATR cell was first allowed to equilibrate at the RH of interest, and then several spectra were recorded to ensure that IL–water equilibrium was reached (this typically took ~ 20 min). Spectra of IL–water or IL–H$_2$O/D$_2$O solutions were recorded under dry RH conditions in the ATR cell.

2.12. Molecular Dynamics Simulations

The simulation systems consisted of 512 [C$_2$MIM]$^+$, 512 anions (Cl$^-$ or BF$_4^-$), and 512 water molecules. Initially, ions and water molecules were placed on a cubic lattice and subjected to 200 steps of conjugate-gradient energy minimization, 2 ns molecular dynamics (MD) simulation at constant volume and temperature (373 K), and 4 ns MD simulation at constant pressure (500 bar) and temperature (373 K). The final segments of the [C$_2$MIM][Cl] and [C$_2$MIM][BF$_4$] trajectories were run at a constant pressure of 1 bar and temperature of 373 K for 31.6 and 26 ns, respectively. Simulations were performed with the NAMD 2.8b1 software package.[16] The force field of de Andrade et al.[17] was used for the [C$_2$MIM]$^+$ and BF$_4^-$ ions, the force field of Beglov and Roux[18] was used for Cl$^-$, and the SPC/E model[19] was used for water. The smooth particle-mesh Ewald method[20,21] was used to calculate electrostatic interactions. Short-range real-space interactions were cut off at 11 Å, employing a switching function. A

reversible multiple time-step algorithm[22] was employed to integrate the equations of motion

with a time step of 2 fs for electrostatic forces, 1 fs for short-range non-bonded forces, and 1 fs

for bonded forces. Snapshots were saved at 1 ps intervals for detailed analysis. All bond lengths

involving hydrogen atoms were held fixed using the SHAKE[23] and SETTLE[24] algorithms. A

Langevin dynamics scheme was used for temperature control, and a Nosé–Hoover–Langevin

piston was used for pressure control.[25,26] Molecular graphics and trajectory analyses were

performed using VMD 1.9[27] over the last 10 ns of each trajectory. The electric field and

frequency distribution calculations were performed using the methods described by Smith et al.[28]

References

(1) *Ionic Liquids in Synthesis*; 2nd ed.; Wasserscheid, P.; Welton, T., Eds.; Wiley-VCH: Weinheim, Germany, 2008; Vol. 1.

(2) Huddleston, J. G.; Visser, A. E.; Reichert, W. M.; Willauer, H. D.; Broker, G. A.; Rogers, R. D. Characterization and Comparison of Hydrophilic and Hydrophobic Room Temperature Ionic Liquids incorporating the Imidazolium Cation. *Green Chem.* **2001**, *3*, 156-164.

(3) Gomez, E.; Gonzalez, B.; Dominguez, A.; Tojo, E.; Tojo, J. Dynamic Viscosities of a Series of 1-Alkyl-3-Methylimidazolium Chloride Ionic Liquids and their Binary Mixtures with Water at Several Temperatures. *J. Chem. Eng. Data* **2006**, *51*, 696-701.

(4) Ghatee, M. H.; Zolghadr, A. R. Surface Tension Measurements of Imidazolium-Based Ionic Liquids at Liquid-Vapor Equilibrium. *Fluid Phase Equilib.* **2008**, *263*, 168-175.

(5) Alshawa, A.; Dopfer, O.; Harmon, C. W.; Nizkorodov, S. A.; Underwood, J. S. Hygroscopic Growth and Deliquescence of NaCl Nanoparticles Coated with Surfactant AOT. *J. Phys. Chem. A* **2009**, *113*, 7678-7686.

(6) Harmon, C. W.; Grimm, R. L.; McIntire, T. M.; Peterson, M. D.; Njegic, B.; Angel, V. M.; Alshawa, A.; Underwood, J. S.; Tobias, D. J.; Gerber, R. B.; Gordon, M. S.; Hemminger, J. C.; Nizkorodov, S. A. Hygroscopic Growth and Deliquescence of NaCl Nanoparticles Mixed with Surfactant SDS. *J. Phys. Chem. B* **2010**, *114*, 2435-2449.

(7) Hogan, C. J.; de la Mora, J. F. Ion-Pair Evaporation from Ionic Liquid Clusters. *J. Am. Soc. Mass Spectrom.* **2010**, *21*, 1382-1386.

(8) Hogan, C. J.; de la Mora, J. F. Tandem Ion Mobility-Mass Spectrometry (IMS-MS) Study of Ion Evaporation from Ionic Liquid-Acetonitrile Nanodrops. *Phys. Chem. Chem. Phys.* **2009**, *11*, 8079-8090.

(9) Ku, B. K.; de la Mora, J. F. Relation between Electrical Mobility, Mass, and Size for Nanodrops 1-6.5 nm in Diameter in Air. *Aerosol Sci. Technol.* **2009**, *43*, 241-249.

(10) Larriba, C.; Hogan, C. J.; Attoui, M.; Borrajo, R.; Garcia, J. F.; de la Mora, J. F. The Mobility-Volume Relationship below 3.0 nm Examined by Tandem Mobility-Mass Measurement. *Aerosol Sci. Technol.* **2011**, *45*, 453-467.

(11) Rader, D. J.; McMurry, P. H. Application of the Tandem Differential Mobility Analyzer to Studies of Droplet Growth or Evaporation. *J. Aerosol Sci.* **1986**, *17*, 771-787.

(12) Stolzenburg, M. R.; McMurry, P. H. *TDMAFIT unser's manual (PTL publication No. 653)*, Particle Technology Laboratory, Univeristy of Minnesota, 1988.

(13) Smith, J. D.; Cappa, C. D.; Wilson, K. R.; Cohen, R. C.; Geissler, P. L.; Saykally, R. J. Unified Description of Temperature-Dependent Hydrogen-Bond Rearrangements in Liquid Water. *P. Natl. Acad. Sci. USA* **2005**, *102*, 14171-14174.

(14) Tyler, J. M.; Branton, D. Rotary Shadowing of Extended Molecules Dried from Glycerol. *J. Ultrastruct. Res.* **1980**, *71*, 95-102.

(15) McIntire, T. M.; Brant, D. A. Imaging of Individual Biopolymers and Supramolecular Assemblies Using Noncontact Atomic Force Microscopy. *Biopolymers* **1997**, *42*, 133-146.

(16) Phillips, J. C.; Braun, R.; Wang, W.; Gumbart, J.; Tajkhorshid, E.; Villa, E.; Chipot, C.; Skeel, R. D.; Kale, L.; Schulten, K. Scalable Molecular Dynamics with NAMD. *J. Comput. Chem.* **2005**, *26*, 1781-1802.

(17) de Andrade, J.; Boes, E. S.; Stassen, H. Computational Study of Room Temperature molten Salts Composed by 1-Alkyl-3-Methylimidazolium Cations-Force-Field Proposal and Validation. *J. Phys. Chem. B* **2002**, *106*, 13344-13351.

(18) Beglov, D.; Roux, B. Solvation of Complex Molecules in a Polar Liquid: An Integral Equation Theory. *J. Chem. Phys.* **1996**, *104*, 8678-8689.

(19) Berendsen, H. J. C.; Grigera, J. R.; Straatsma, T. P. The Missing Term in Effective Pair Potentials. *J. Phys. Chem.* **1987**, *91*, 6269-6271.

(20) Darden, T.; York, D.; Pedersen, L. Particle mesh Ewald: An $N \cdot \log(N)$ Method for Ewald Sums in Large Systems. *J. Chem. Phys.* **1993**, *98*, 10089-10092.

(21) Essmann, U.; Perera, L.; Berkowitz, M. L.; Darden, T.; Lee, H.; Pedersen, L. G. A Smooth Particle Mesh Ewald Method. *J. Chem. Phys.* **1995**, *103*, 8577-8593.

(22) Grubmüller, H.; Heller, H.; Windemuth, A.; Schulten, K. Generalized Verlet Algorithm for Efficient Molecular Dynamics Simulations with Long-Range Interactions. *Mol. Simulation* **1991**, *6*, 121-142.

(23) Ryckaert, J.-P.; Ciccotti, G.; Berendsen, H. J. C. Numerical Integration of the Cartesian Equations of Motion of a System with Constraints: Molecular Dynamics of *n*-Alkanes. *J. Comput. Phys.* **1977**, *23*, 327-341.

(24) Miyamoto, S.; Kollman, P. An Analytical Version of the SHAKE and RATTLE Algorithm for Rigid Water Models. *J. Comput. Chem.* **1992**, *13*, 952-962.

(25) Feller, S. E.; Zhang, Y.; Pastor, R. W.; Brooks, B. R. Constant Pressure Molecular Dynamics Simulation: The Langevin Piston Method. *J. Chem. Phys.* **1995**, *103*, 4613-4621.

(26) Martyna, G. J.; Tobias, D. J.; Klein, M. L. Constant-Pressure Molecular-Dynamics Algorithms. *J.Chem.Phys.* **1994**, *101*, 4177-4189.

(27) Humphrey, W.; Dalke, W.; Schulten, K. VMD: Visual Molecular Dynamics. *J. Mol. Graphics* **1996**, *14*, 33-38.

(28) Smith, J. D.; Saykally, R. J.; Geissler, P. L. The Effects of Dissolved Halide Anions on Hydrogen Bonding in Liquid Water. *J. Am. Chem. Soc.* **2007**, *129*, 13847-13856.

Chapter 3: Enhancement of Surfactants in Nanoparticles Produced by an Electrospray Aerosol Generator

3.1. Abstract

Electrospray aerosol generators (EAGs) disperse conducting solutions into air, promptly neutralize the particles to remove the excess charge, and evaporate the residual solvent with a dry air flow. For solutions containing multiple solutes, the particles may become enhanced in the more surface-active solutes. The extent of the enhancement was estimated for nanoparticles electrosprayed from a solution containing sodium chloride (NaCl) and surfactant sodium dodecyl sulfate (SDS) mixed in a 9:1 weight ratio. A tandem particle mobility analyzer was used to quantify the hygroscopic growth factor (GF). The relative fractions of NaCl and SDS in the particles were estimated from the measured GFs assuming that NaCl and SDS take up water independently of each other. The nanoparticles were considerably enhanced in SDS relative to the starting solution, with the NaCl:SDS weight ratio increasing with the distance from the EAG electrified capillary tip to the neutralizer, and reaching ~1:1 at the longest distances probed. The enhancement in SDS likely occurred during particle fission events as particles travelled from the capillary to the neutralizer. This study has practical ramifications for aerosol nanotechnology and aerosol-assisted drug delivery, which rely on EAG as an instrument of choice for nanoparticle generation.

3.2. Introduction

In this chapter, the goal of this work is to investigate the effect of l_s on the enhancement of surface-active species in nanoparticles produced by an electrospray aerosol generator (EAG). The electrospray process is described in Chapter 2. We rely on tandem hygroscopic growth factor (GF) measurements[1] of EAG-generated nanoparticles as an indirect way to probe their chemical composition. The particles contain an ionic surfactant, sodium dodecyl sulfate (SDS) (Figure 2.1), with small hygroscopic GF values and a hygroscopic salt, sodium chloride (NaCl), with large GF values. When exposed to a well-defined relative humidity (RH) the particles grow in size due to uptake of water by NaCl. The particles' GF is measured experimentally as the ratio of the mobility-equivalent diameter of the wet particles, $d_{m,wet}(RH)$, to the mobility-equivalent diameter of the dry particles, $d_{m,dry}$ (eq 1.1).

Assuming that NaCl and SDS take up water independently in proportion to their corresponding volume fractions, the amount of SDS in the particles at any RH can be estimated from the GF and assumed particle morphology. We will show that increasing the distance between the capillary tip and the neutralizer increases the relative amount of SDS in the nanoparticles. These results are consistent with the hypothesis that progeny droplets, formed from the fission events of primary droplets, are enriched with the surface-active species present.

3.3. Experimental

The experimental conditions including the chemicals used, solution preparation, nanoparticle generation, and hygroscopicity measurements can be found in Chapter 2. Specifically, chemicals used can be found in Section 2.2.1. Solution preparation and

nanoparticle generation can be found in Section 2.6.1. Hygroscopic growth measurements can be found in Section 2.7.1.

3.4. Results and Discussion

A typical size distribution of the SDS/NaCl particles exiting the neutralizer is shown in Figure 2.5b. The distribution is plotted as a function of the average mobility-equivalent diameter that penetrates through the nano-DMA2 based on the voltage applied to its central rod. The mean mobility-equivalent diameter for the full particle distribution (~16 nm) is close to the particle diameter of 24 nm predicted from the EAG scaling laws by Chen et al.[2] The mean diameter did not change significantly as the capillary-neutralizer distance l_s was varied. The corresponding distribution for the pure NaCl particles (not included) was similar. We have not verified whether the particles have achieved the equilibrium Boltzmann charge distribution after the neutralizer, but the monomodal shape of the distribution suggests that all particles passing through nano-DMA1 are singly-charged, an important pre-requisite for the TDMA measurements. If multiply-charged particles were present, a multimodal size distribution would have been observed.[3]

In conventional EAG sources, neutralization was accomplished with [210]Po neutralizers.[2,4] This work suggests that [85]Kr neutralizers are also suitable for EAG sources (in fact, we found no significant differences in measured size distributions when the [85]Kr neutralizer was replaced with a [210]Po neutralizer). Figure 2.5c shows an example of a particles' size distribution for the dry SDS/NaCl particles that were size-selected by nano-DMA1 and measured by nano-DMA2. The size distribution corresponding to the size-selected and humidified particles was similar but shifted towards higher mobility diameter by a factor of GF.

Harmon et al.[5] investigated the hygroscopic growth for nanoparticles of pure NaCl, pure SDS, and variable SDS/NaCl content over the RH range of 1 to 95%. The GF values of the particles with variable SDS/NaCl content measured in that study implied that the relative fractions of SDS in the nanoparticles were significantly higher than the corresponding SDS fractions in the initial solution. In order to provide a more definite proof of the SDS enhancement, we performed experiments in which the RH and solution composition were fixed and only l_s was varied. To simplify the quantitative analysis of the measured GF values, the RH was also fixed at 90%, which is above the deliquescence RH of NaCl. At this RH value, all NaCl in the particles should be fully deliquesced.

The change in GF as a function of capillary distance is shown in Figure 3.1a. As expected, the GF of the pure NaCl particles remains unchanged as l_s increases. As noted in the experimental section, the absolute value of the GFs may be slightly off because the initial particles's size distribution generated by the EAG is comparable in width to the transfer function of the nano-DMA.[1] Nevertheless, the measured value is in qualitative agreement with previous GF measurements for NaCl nanoparticles by other research groups.[6–8] For example, the theoretical GF = 1.87 for pure NaCl at 90% RH, calculated using "Model 4" from Biskos et al.,[7] is in good agreement with the experimental results.
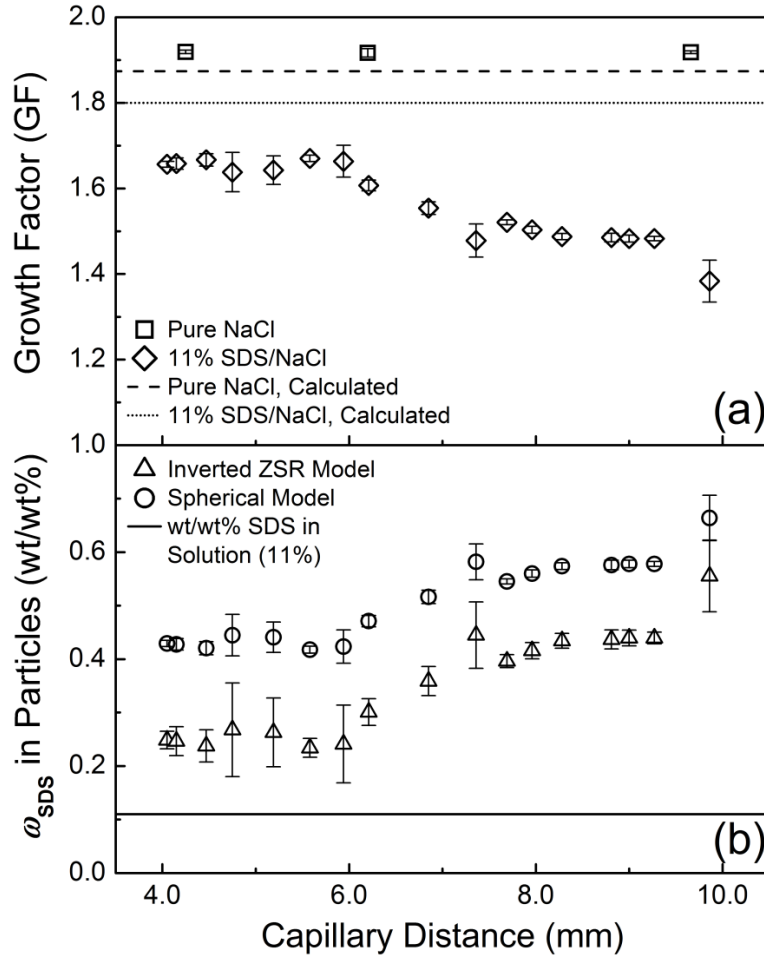
Figure 3.1. (a) Measured GFs of SDS/NaCl particles and pure NaCl particles at 90% RH as a function of the capillary distance. As the capillary distance increases, GFs of SDS/NaCl particles decrease, whereas the GF of pure NaCl remains unchanged. The dashed line represents the GF = 1.87 calculated for pure NaCl using "Model 4" from Biskos et al.[7] The dotted line represents the GF = 1.80 expected for the SDS/NaCl particles from the ZSR model (eq 3.1) assuming that particles have the same SDS/NaCl proportion as the electrosprayed solution. (b) Weight fraction of SDS (ω_{SDS}) in the nanoparticles calculated from the measured GF values using the inverted ZSR model (eq 3.3) and the "Spherical Model". The straight line represents the ω_{SDS} in the initial solute (0.11). The relative amount of SDS in the particle is approximately enhanced by a factor of 4 to 6.

Calculating the theoretical GF for the SDS/NaCl particles at 90% RH is a challenge because of the uncertainty regarding the exact amount of SDS in the final particles. However, it can be estimated using the experimental GF values and the Zdanovskii-Stokes-Robinson (ZSR) mode.[9–11] The ZSR model assumes that the overall growth of a mixed SDS/NaCl particle is entirely due to independent water uptake by the different particle components. As pure SDS does not measurably grow at the RH values probed in this work[5], we can write the following simplified ZSR equation:

$$GF^3 = \varepsilon_{SDS}GF_{SDS}^3 + \varepsilon_{NaCl}GF_{NaCl}^3 \approx 1 + \varepsilon_{NaCl}(GF_{NaCl}^3 - 1) \qquad (3.1)$$

In eq 3.1, GF_{SDS} and GF_{NaCl} are the GF values for the particles made of pure SDS and NaCl, respectively, and ε_{SDS} and ε_{NaCl} are the volume fractions of SDS and NaCl in the mixed particle. The GF = 1.80 value for the SDS/NaCl mixture predicted from eq 3.1 is much larger than the experimentally observed values shown in Figure 3a implying that the particles are depleted in NaCl or, equivalently, enhanced in SDS.

Furthermore, in contrast to the GF of the pure NaCl particles, the GF values of the SDS/NaCl particles reproducibly decrease as l_s increases, despite the fact that particles of the same mobility are selected by nano-DMA1 prior to the humidification. As pure SDS nanoparticles exhibit almost no hygroscopic growth at this RH[5], all of the particle growth in the mixed case must be due to equilibrium water uptake of the NaCl component. To explain the observations, we have to assume that particles formed at larger l_s must have larger weight fractions of SDS (ω_{SDS}), defined as $\omega_{SDS} = m_{SDS}/(m_{NaCl} + m_{SDS})$, where m_{SDS} and m_{NaCl} are the masses of SDS and NaCl in the particles, respectively. These larger values of ω_{SDS} at larger l_s agree with the expected mechanism of particle formation for EAGs (Figure 1.2). The goal of the

following discussion is to estimate ω_{SDS} from the measured GF data, and compare it to the

solution's initial ω_{SDS} of 0.11 (corresponding to the initial dry mole fraction of 0.024 for SDS).

A direct measurement of the amounts of SDS and NaCl in the nanoparticles is difficult

due to the miniscule amount of particulate material produced by EAGs. Under the optimal

conditions, our EAG produces about 10^5 particles cm^{-3} in a 1 SLM flow or about 100 ng of 20

nm particles per hour of operation. Our previous attempts to quantify the Cl to S ratio in these

particles using X-ray photoelectron spectroscopy did not succeed.[5] However, the relative

amounts of SDS and NaCl can be obtained indirectly from the ZSR model (eq 3.1). The

measured GFs at every capillary distance (Figure 3.1a) can be converted into the volume

fractions of NaCl through an inversion of eq 3.2:

$$\varepsilon_{NaCl} \approx \frac{GF^3 - 1}{GF_{NaCl}^3 - 1} \tag{3.2}$$

These can then be converted into the corresponding weight fractions of NaCl (ω_{NaCl}),

$$\omega_{NaCl} \approx \frac{\varepsilon_{NaCl} \cdot \rho_{NaCl}}{\rho_{SDS} + \varepsilon_{NaCl} \cdot \left(\rho_{NaCl} - \rho_{SDS} \right)} \tag{3.3}$$

using the bulk densities of $\rho_{NaCl} = 2163$ kg m^{-3} and $\rho_{SDS} = 1010$ kg m^{-3}. We note that using this

particular density for SDS is a simplification in view of the large number of its possible solid

phases.[12] The estimated values of $\omega_{SDS} = 1 - \omega_{NaCl}$ are shown in Figure 3.1b as a function of l_s.

They are significantly larger than the initial ω_{SDS} of 0.11 in the electrosprayed solution, and

increase with l_s.

The above estimation is rather crude as it does not take into account the difference in the

shapes of the dry NaCl and SDS/NaCl particles and neglects Kelvin effect. Furthermore,

deviations from the ZSR model may occur when the interactions between different phases within

the particle are significant. The ZSR model was found to perform poorly in the case of submicron SDS/NaCl particles interacting with water vapor below the deliquescence transition, in part due to the complicated shapes of the mixed particles.[13]

A more accurate estimation of ω_{SDS} in the SDS/NaCl particles based on the measured hygroscopic GFs is described below. In view of multiple assumptions, the formulas listed here should be treated as approximate. However, they are expected to be more accurate compared to the ZSR model[9–11] described previously.

Following NaCl deliquescence and further hygroscopic growth, a mixed SDS/NaCl nanoparticle can be viewed as an aqueous droplet containing dissolved NaCl coated with an SDS film. Even though SDS does not take up water by itself to a measurable extent,[5] it is expected to lower the surface tension of the droplet and affect the GF indirectly through the Kelvin effect. Furthermore, as SDS has non-zero solubility in solution with NaCl, the presence of dissolved SDS in the aqueous solution changes the water activity. We can correct for the Kelvin effect using the following equation:

$$\frac{RH}{100} = a_{aq}(x) \cdot \exp\left(\frac{4 M_w \sigma_{aq}(x)}{RT \rho_w d_{m,wet}(RH)}\right) \tag{3.4}$$

In eq 3.4, x is the weight percent of NaCl in the aqueous phase (mass of NaCl relative to the mass of the solution expressed in percent), M_w is the molecular weight of water, and ρ_w is the density of water. We take the dependence of the activity of water in the aqueous phase (a_{aq}) on x from Tang et al.[14] ($C_0 = 1$; $C_1 = -6.366 \times 10^{-3}$; $C_2 = 8.624 \times 10^{-5}$; $C_3 = -1.158 \times 10^{-5}$; $C_4 = 1.518 \times 10^{-7}$).

$$a_{aq}(x) = \sum_{i=0}^{4} C_i x^i \tag{3.5}$$

We assume that the amount of SDS dissolved in the aqueous phase is small relative to that of NaCl and, therefore, the presence of SDS does not significantly change a_{aq}. The x-dependent values of the surface tension, $\sigma_{aq}(x)$, for a pure NaCl solution is taken from Pruppacher and Klett.[15]

$$\sigma_{aq}(x) = \left(0.072 + \frac{0.029x}{100-x} \right) \frac{N}{m} \tag{3.6}$$

The x-dependence of the surface tension of an SDS-coated solution of NaCl is not known and a value 0.040 N m^{-1} is adopted, which is appropriate for an SDS-coated water surface.[16]

Before the measured GF can be converted into ω_{SDS} and ω_{NaCl} (the weight fraction of NaCl in the SDS/NaCl particles), we have to make additional assumptions about the shape of the initial particle before it was exposed to water vapor. The most straightforward case to consider is that of a spherical NaCl core surrounded by a uniform shell of SDS (i.e., "Spherical Model"). The calculations are done iteratively. A certain guessed value of ω_{NaCl} is assumed, and the corresponding volume fraction of NaCl (ε_{NaCl}) value is calculated

$$\varepsilon_{NaCl} = \frac{\omega_{NaCl} \cdot \rho_{SDS}}{\rho_{NaCl} - \omega_{NaCl} \cdot \left(\rho_{NaCl} - \rho_{SDS} \right)} \tag{3.7}$$

using the bulk densities of $\rho_{NaCl} = 2163$ kg m^{-3} and $\rho_{SDS} = 1010$ kg m^{-3}. The diameter of the NaCl core in the initial dry particle is then:

$$d_{core,dry} = d_{m,dry} \cdot \left(\varepsilon_{NaCl} \right)^{1/3} \tag{3.8}$$

After the particle interacts with water vapor, the NaCl core dissolves and increases in size by the GF of the NaCl core:

$$GF_{core} = \frac{d_{core,wet}}{d_{core,dry}} = \left(\frac{100 \cdot \rho_{NaCl}}{x \cdot \rho_{aq}(x)} \right)^{\frac{1}{3}} \tag{3.9}$$

The density of the NaCl solution, $\rho_{aq}(x)$, is taken from Tang et al.[14] ($A_0 = 997.1$; $A_1 = 7.41$; $C_2 = -3.741 \times 10^{-2}$; $A_3 = 2.525 \times 10^{-3}$; $A_4 = -2.060 \times 10^{-5}$).

$$\rho_{aq}(x) = \left(\sum_{i=0}^{4} A_i x^i \right) \frac{kg}{m^3} \tag{3.10}$$

Once again, we are making an assumption that SDS does not significantly affect the density of the NaCl solution.

For a given assumed value of ω_{NaCl}, the above system of equations has a unique solution for x which can be found numerically. This makes it possible to predict GF$_{calculated}$,

$$GF_{calculated} = \left(1 + \varepsilon_{NaCl} \left(GF_{core}^3 - 1 \right) \right)^{\frac{1}{3}} \tag{3.11}$$

and compare it to the experimentally measured GF value. The trial ω_{NaCl} is adjusted until the experimental GF is matched to within 0.001, with the conversion typically achieved after 3 to 4 iterations. The resulting values of ω_{NaCl} calculated are shown in Figures 3.1b and 3.2b.

As shown in Figure 3.1b, the values of ω_{SDS} approximated from the ZSR model and from the more refined "Spherical Model" described above suggest a significant enhancement of SDS in the final nanoparticles. The ratio of the weight concentrations of SDS and NaCl in the initial solution is about 1:9 (the corresponding molar ratio is about 1:40). The same proportion of SDS and NaCl in the particles would correspond to a ω_{SDS} of 0.11, a value indicated in Figure 3.1b by a thick horizontal line. While approximate, the calculations suggest that the actual ω_{SDS} values might range from ~0.4 at the smallest l_s (4 mm) to ~0.6 at the largest l_s (10 mm). As discussed in more detail below, this behavior is consistent with the model in which particle fission events

produce progeny droplets enriched with surface-active species. The effect on the particle composition is quite dramatic. At the largest values of the distance between the EAG capillary and the neutralizer (10 mm), the estimated SDS:NaCl weight ratio in the particles exceeds 1:1 (molar ratio 1:5), which is very different from the initial solution.

We also conducted experiments in which the capillary to neutralizer distance was fixed but the initial dry mobility-equivalent diameter of the particles was varied. Figure 3.2a shows the measured GF values at 90% RH and Figure 3.2b shows the corresponding ω_{SDS} values plotted as a function of the initial dry particle mobility-equivalent diameter. We find that smaller particles tend to contain more SDS, although the particles' size dependence is not very pronounced for the probed initial mobility sizes of 11 to 17 nm.

These observations can be rationalized with a simple conceptual model. With the initial solution composition used in this study, the primary droplets formed by the electrospray should have enough surface area to accommodate *all* of the SDS molecules on the surface (all droplets below about 30 µm in size will be under-saturated with respect to the full surface coverage of 4×10^{-10} mol cm^{-2} measured by Iyota and Krastev.[16] If we assume that all of the SDS and NaCl reside on the droplet surface and interior, respectively, and that the SDS surface distribution can instantaneously adjust during droplet distortions, we can expect significant SDS enhancement during an asymmetric droplet fission. For example, if we start with a 1 µm primary droplet with $\omega_{SDS} = 0.11$, and let the primary droplet undergo an asymmetric fission into a 0.1 µm progeny droplet, the new ω_{SDS} in the progeny droplet has the potential to increase by a factor of five. Comparison with the data shown in Figures 3.1b and 3.2b suggest the observed SDS enhancement can result already after a *single asymmetric fission event*. Even larger enhancement in the surface-active compounds can be expected if the progeny droplet itself goes through

65

another fission event. For less surface-active compounds, which distribute more uniformly between the droplet surface and interior, the enhancement will be smaller.
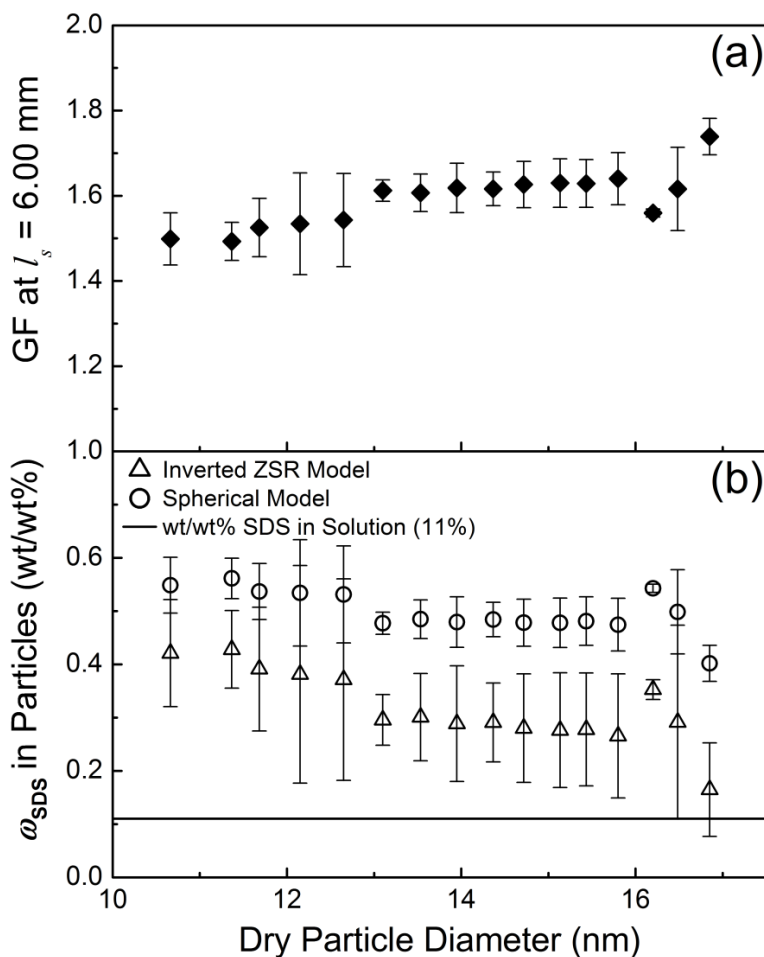
Figure 3.2. (a) Measured GFs of SDS/NaCl particles at a fixed capillary distance (6.00 mm) for various initial dry particle mobility-equivalent diameters (nm) at 90% RH. (b) Calculated weight fraction of SDS (ω_{SDS}) in the nanoparticles using the inverted ZSR model (eq 3.3) and the "Spherical model". The straight line represents the ω_{SDS} in the initial solute (0.11). As the initial particle diameter increases, measured GF increases and the ω_{SDS} in the particle decreases.

3.5. Conclusion

Why are these observations significant? Aerosolization of solutions with EAG devices finds increasing use in various applications including aerosol-assisted nanomaterial synthesis,[17, 18] targeted drug delivery,[19,20] and mobility analysis of colloids,[21,22] proteins,[23] and viruses.[24–27] We have shown that the chemical composition of the nanoparticles produced by an EAG may be quite sensitive to the operation conditions and not necessarily reflect the distribution of solutes in the initial solution. If the spray is not neutralized promptly, the surface-active species may become significantly enriched in the nanoparticles. As the enrichment occurs during fission of the highly charged particles, it is difficult to fully suppress this effect because at least some fission is necessary to break down the droplets produced from the electrospray cone. Therefore, we anticipate that surface-active species will always be enriched to some extent in EAG-generated nanoparticles, regardless of the specifics of the EAG design. EAG users should be mindful of this effect and design their experiments appropriately to compensate for it.

References

(1)   Rader, D. J. and McMurry, P. H. Application of the Tandem Differential Mobility
        Analyzer to Studies of Droplet Growth or Evaporation. *J. Aerosol Sci.* **1986,** *17*, 771-787.

(2)   Chen, D.-R., Pui, D. Y. H. and Kaufman, S. L. Electrospraying of Conducting liquids for
        Monodisperse Aerosol Generation in the 4 nm to 1.8 mm Diameter RANGE. *J. Aerosol
        Sci.***1995**, *26*, 963-977.

(3)   Modesto-Lopez, L. B., Kettleson, E. M. and Biswas, P. Soft X-ray Charger (SXC)
        System for Use with Electrospray for Mobility Measurement of Bioaerosols. *J.
        Electrostatics* **2011,** *69*, 357-364.

(4)   Scalf, M., Westphall, M. S., Krause, J., Kaufman, S. L. and Smith, L. M. Controlling
        Charge States of Large Ions. *Science* **1999**, *283*, 194-197.

(5)   Harmon, C. W., Grimm, R. L., McIntire, T. M., Peterson, M. D., Njegic, B., Angel, V.
        M., Alshawa, A., Underwood, J. S., Tobias, D. J., Gerber, R. B., Gordon, M. S.,
        Hemminger, J. C. and Nizkorodov, S. A. Hygroscopic Growth and Deliquescence of
        NaCl Nanoparticles Mixed with Surfactant SDS. *J. Phys. Chem. B* **2010**, *114*, 2435-2449.

(6)   Biskos, G., Malinowski, A., Russell, L., Buseck, P. and Martin, S. Nanosize Effect on the
        Deliquescence and the Efflorescence of Sodium Chloride Particles. *Aerosol Sci. Technol.*
        2006, *40*, 97-106.

(7)   Biskos, G., Russell, L. M., Buseck, P. R. and Martin, S. T. Nanosize Effect on the
        Hygroscopic Growth Factor of Aerosol Particles. *Geophys. Res. Lett.* **2006**, *33*, L07801,
        doi:07810.01029/02005GL025199.

(8)   Hameri, K., Laaksonen, A., Vakeva, M. and Suni, T. Hygroscopic Growth of Ultrafine Sodium Chloride Particles. *J. Geophys. Res. D* **2001**, *106*, 20749-20757.

(9)   Stokes, R. H. and Robinson, R. A. Interactions in Aqueous Nonelectrolyte Solutions. I. Solute-Solvent Equilibriums. *J. Phys. Chem.* **1966**, *70*, 2126-2131.

(10)   Svenningsson, B., Rissler, J., Swietlicki, E., Mircea, M., Bilde, M., Facchini, M. C., Decesari, S., Fuzzi, S., Zhou, J., Moenster, J. and Rosenoern, T. Hygroscopic Growth and Critical Supersaturations for Mixed Aerosol Particles of Inorganic and Organic Compounds of Atmospheric Relevance. *Atm. Chem. Phys.* **2006**, *6*, 1937-1952.

(11)   Varutbangkul, V., Brechtel, F. J., Bahreini, R., Ng, N. L., Keywood, M. D., Kroll, J. H., Flagan, R. C., Seinfeld, J. H., Lee, A. and Goldstein, A. H. Hygroscopicity of Secondary Organic Aerosols Formed by Oxidation of Cycloalkenes, Monoterpenes, Sesquiterpenes, and Related Compounds. *Atm. Chem. Phys.* **2006**, *6*, 2367-2388.

(12)   Sperline, R. P. Infrared Spectroscopic Study of the Crystalline Phases of Sodium Dodecyl Sulfate. *Langmuir* **1997**, *13*, 3715-3726.

(13)   Zelenyuk, A., Imre, D., Cuadra-Rodriguez, L. A. and Ellison, B. Measurements and Interpretation of the Effect of a Soluble Organic Surfactant on the Density, Shape, and Water Uptake of Hygroscopic Particles. *J. Aerosol Sci.* **2007**, *38*, 903-923.

(14)   Tang, I. N., Tridico, A. C. and Fung, K. H. Thermodynamic and Optical Properties of Sea Salt Aerosols. *J. Geophys. Res.* **1997**, *102*, 23269-23275.

(15)   Pruppacher, H. R. and Klett, J. D. *Microphysics of Clouds and Precipitation*. Kluwer Academic: Boston, USA, 1997; pp 976.

(16)   Iyota, H. and Krastev, R. Miscibility of Sodium Chloride and Sodium Dodecyl Sulfate in the Adsorbed Film and Aggregate. *Colloid Polym. Sci* **2009**, *287*, 425-433-433.

(17)   Jaworek, A. and Sobczyk, A. T. Electrospraying Route to Nanotechnology: An

Overview. *J. Electrostatics* **2008**, *66*, 197-219.

(18)   Lu, Y., Fan, H., Stump, A., Ward, T. L., Rieker, T. and Brinker, C. J. Aerosol-Assisted

Self-Assembly of Mesostructured Spherical Nanoparticles. *Nature* **1999**, *398*, 223-226.

(19)   Chattopadhyay, S., Modesto-Lopez, L. B., Venkataraman, C. and Biswas, P. Size

Distribution and Norphology of Liposome Aerosols Generated by two Methodologies.

Aerosol Sci. Technol. **2010**, *44*, 972-982.

(20)   Tang, K. and Gomez, A. Generation by Electrospray of Monodisperse Water droplets for

Targeted Drug Delivery by Inhalation. *J. Aerosol Sci.* **1994**, *25*, 1237-1249.

(21)   Lenggoro, I. W., Xia, B., Okuyama, K. and Fernandez de la Mora, J. Sizing of Colloidal

Nanoparticles by Electrospray and Differential Mobility Analyzer Methods. *Langmuir*

2002, *18*, 4584-4591.

(22)   Ude, S., Fernandez de la Mora, J., Alexander, J. N. and Saucy, D. A. Aerosol Size

Standards in the Nanometer Size Range. II. Narrow Size Distributions of Polystyrene 3-

11 nm in Diameter. *J. Colloid Interface Sci.* **2006**, *293*, 384-393.

(23)   Szymanski, W. W., Bacher, G. and Allmaier, G. Nano-Aerosol Approach for

Characterization of Proteins and Viruses. *Proceedings of SPIE-The International Society

for Optical Engineering* **2001**, *4590*, 38-44.

(24)   Eninger, R. M., Hogan, C. J., Jr., Biswas, P., Adhikari, A., Reponen, T. and Grinshpun,

S. A. Electrospray Versus Nebulization for Aerosolization and Filter Testing with

Bacteriophage Particles. *Aerosol Sci. Technol.* **2009**, *43*, 298-304.

(25)   Pease, L. F., III, Lipin, D. I., Tsai, D.-H., Zachariah, M. R., Lua, L. H. L., Tarlov, M. J.

and Middelberg, A. P. J. Quantitative Characterization of Virus-Like Particles by

Asymmetrical Flow Field Flow Fractionation, Electrospray Differential Mobility Analysis, and Transmission Electron Microscopy. *Biotech. Bioengineering* **2009**, *102*, 845-855.

(26)   Thomas, J. J., Bothner, B., Traina, J., Benner, W. H. and Siuzdak, G. Electrospray Ion Mobility Spectrometry of Intact Viruses. *Spectroscopy* **2004**, *18*, 31-36.

(27)   Tito, M. A., Tars, K., Valegard, K., Hajdu, J. and Robinson, C. V. Electrospray Time-of-Flight Mass Spectrometry of the Intact MS2 Virus Capsid. *J. Am. Chem. Soc.* **2000**, *122*, 3550-3551.

Chapter 4: Interaction of Water Vapor with the Surfaces of Imidazolium-Based Ionic Liquid Nanoparticles and Thin Films

4.1. Abstract

Understanding the interactions of humid air with ionic liquids (ILs) is critical for predicting how their physicochemical properties are affected by water. Using experimental and theoretical techniques, water vapor's interaction with aerosolized nanoparticles and thin films of 1-ethyl-3-methylimidazolium chloride ([C$_2$MIM][Cl]) and 1-ethyl-3-methylimidazolium tetrafluoroborate ([C$_2$MIM][BF$_4$]) was studied. Solutions were electrosprayed to produce dry particles. Particles' hygroscopic growth was quantified using tandem nanodifferential mobility analysis as a function of relative humidity (RH). This is the first report of the interaction of water with aerosolized IL nanoparticles. The particles' small size allows true IL–water vapor equilibrium achieved quickly. Growth curves for both ILs show steady water uptake with increasing RH. Water vapor uptake by IL thin films was also examined using attenuated total reflection-Fourier transform infrared (ATR-FTIR) spectroscopy. Both experimental methods show [C$_2$MIM][Cl] absorbs more water vapor than [C$_2$MIM][BF$_4$] over the entire RH range. Water molar fractions, calculated from growth curves, agreed well with those estimated from ATR-FTIR data. Molecular dynamics (MD) simulations, used to model IL–water interactions, revealed strong interactions between Cl$^-$ and water and considerably weaker interactions between BF$_4$$^-$ and water. Widths and position of O–H stretching vibrations from MD simulations qualitatively reproduced ATR-FTIR results. These experimental and theoretical data provide a comprehensive picture of the behavior of absorbed water in ILs.

4.2. Introduction

In this chapter, we discuss the interaction of 1-ethyl-3-methylimidazolium chloride ([C_2MIM][Cl]) and 1-ethyl-3-methylimidazolium tetrafluoroborate ([C_2MIM][BF_4]) ionic liquid (IL) nanoparticles with water absorbed from the vapor phase using hygroscopicity measurements, as outlined in chapter 1. The ILs chemical structures are shown in Figure 2.2. By aerosolizing ILs and comparing their dry sizes to their wet sizes, we can quantitatively determine the amount of water that particles can take up from humidified air over a broad range of relative humidity (RH). In addition, attenuated total reflection-Fourier transform infrared (ATR-FTIR) spectra of thin films of [C_2MIM][Cl] and [C_2MIM][BF_4] are measured, and the C–H and O–H band positions and intensities are determined as a function of RH in order to provide information about the nature of interactions between ILs and water molecules. We also carry out molecular dynamics (MD) simulations of equimolar IL–water mixtures to aid in the interpretation of experimental data. These experimental and theoretical data, in combination, provide a comprehensive picture of the behavior of absorbed water in ILs.

4.3. Experimental

The experimental conditions including the chemicals used, solution preparation, nanoparticle generation, hygroscopicity measurements, ATR-FTIR measurements, and MD simulations can be found in Chapter 2. Specifically, chemicals used can be found in Section 2.2.2. Solution preparation and nanoparticle generation can be found in Section 2.6.2. Hygroscopic growth measurements can be found in Section 2.7.2. ATR-FTIR measurements can be found in Sections 2.10 and 2.11. MD simulations can be found in Section 2.12.

4.4. Results and Discussion

4.4.1. Hygroscopic Growth of Ionic Liquid Nanoparticles

The measured hygroscopic growth curves (from ~0 to 92% RH) for [C₂MIM][Cl] and

[C₂MIM][BF₄] nanoparticles with initial mobility-equivalent diameters of 26.9 ± 0.1 nm are

shown in Figure 4.1. Growth curves were obtained by plotting the measured growth factor (GF)

as a function of RH using eq 1.1.

Figure 4.1. Hygroscopic growth curve of mobility-equivalent diameter selected 26.9 ± 0.1 nm
particles of [C₂MIM][Cl] (circles) and [C₂MIM][BF₄] (triangles). Both ionic liquids undergo a
gradual increase in growth factor (GF) as the relative humidity is increased. [C₂MIM][Cl] has a
larger GF compared to [C₂MIM][BF₄] and thus takes up more water.

75

Growth curves were constructed from a large number of separate experiments, with each experimental run typically spanning 10–30% RH units and taking about one day to complete. All available GF values were then averaged into 1 and 3% RH bins for [C$_2$MIM][Cl] and [C$_2$MIM][BF$_4$], respectively, with each bin typically containing ≥12 measurements from several independent experimental runs. The 95% confidence intervals in Figure 4.1 illustrate the degree of reproducibility of these measurements. For both IL growth curves, the data become less reproducible at RH values >85% due to the high sensitivity of RH to temperature at these high RH values.

The nanoparticles were exposed to RH for a period of a few seconds in these experiments. To ensure equilibrium was reached on this time scale, additional measurements were performed wherein the [C$_2$MIM][Cl] and [C$_2$MIM][BF$_4$] nanoparticles were exposed to RH for a longer time of ~70 s. Increasing the interaction time did not change the GF values, suggesting that equilibrium was established after only a few seconds of exposure. The rapid establishment of equilibrium with water is a key advantage of the nanoparticle hygroscopic growth measurements compared to experiments with bulk ILs.

As shown in Figure 4.1, there is a gradual increase in the uptake of water vapor with increasing RH for both $[C_2MIM][Cl]$ and $[C_2MIM][BF_4]$. Over the entire RH range, $[C_2MIM][Cl]$ absorbs more water and has a larger GF compared to $[C_2MIM][BF_4]$. At the highest RH value used for both ILs, ~92% RH, the GFs of $[C_2MIM][Cl]$ and $[C_2MIM][BF_4]$ are 1.39 ± 0.01 and 1.14 ± 0.01, corresponding to an increase in particle volume due to water uptake by a factor of 2.69 and 1.48, respectively. Furthermore, $[C_2MIM][Cl]$ is considerably more efficient at uptake of water vapor at low RH. For example, at 20% RH, there is no noticeable growth of $[C_2MIM][BF_4]$, while the diameter of $[C_2MIM][Cl]$ increases by 5% (GF ~1.05).

It should to be noted that TDMA classifies particles by their mobility-equivalent diameter, which is equal to the true diameter only when the particles are homogeneous and spherical. For non-spherical or heterogeneous particles, a shape-dependent correction to the GF is required.[1-3] $[C_2MIM][BF_4]$ is a liquid at room temperature, and it remains liquid when it is mixed with water; its nanoparticles, in an aerosolized form, should adopt a spherical shape under all RH conditions. Indeed, work by Larriba et al. on mobility of charged $[C_2MIM][BF_4]$ clusters showed that they were well described as spheres with effective densities similar to that of bulk $[C_2MIM][BF_4]$ for cluster sizes in excess of 1.5 nm.[4] $[C_2MIM][Cl]$ is a solid at room temperature, but it becomes a liquid when mixed with even small amounts of water. The shape of the $[C_2MIM][Cl]$ growth curve suggests that the $[C_2MIM][Cl]$ nanoparticles generated by the ES source are either spherical or close to spherical in shape (water-induced restructuring would make the apparent GF be < 1 at low RH otherwise).[5-7] Therefore, we expect that the $[C_2MIM][Cl]$ particles remain spherical throughout the entire RH range, and the GF data in Figure 4.1 reflect the actual increase in the particle diameter. The average GF values for

[C$_2$MIM][BF$_4$] are slightly lower than 1 at RH < 20%, however the error bars encompass the GF = 1.00 value.

In contrast to the smooth increase in GF with RH for the IL nanoparticles, hygroscopic growth curves of typical inorganic, ionic compounds have well-defined deliquescence phase transitions that manifest themselves as an abrupt change in the GF at a certain RH value. For example, sodium chloride (NaCl) and ammonium sulfate [(NH$_4$)$_2$SO$_4$] deliquesce around ~75% and ~80% RH, respectively. No evidence for phase transitions was observed for either IL in this study (Figure 4.1). The absence of a phase transition for [C$_2$MIM][Cl] is surprising, considering that it is a solid at room temperature. If a water vapor induced solid-to-liquid phase transition does occur in [C$_2$MIM][Cl], it must do so without a significant change in the particle size. The smooth increase in the GF with RH is more reminiscent to the behavior of particles composed of hygroscopic liquids. For example, the growth curve for sulfuric acid particles, with $d_{m,dry}$ = ~30 nm, depicts a smooth increase in wet particle size as RH increases, with a GF of ~1.6 at 80% RH.[8]

Although the imidazolium ILs are regarded as hygroscopic, their GFs are actually small in comparison with inorganic salts. For example, Biskos et al. performed systematic measurements of GFs of pure NaCl nanoparticles of different sizes.[6] At 80% RH, NaCl particles with $d_{m,dry}$ = 30 nm had a larger GF of 1.60[6] compared to 1.26 ± 0.01 for [C$_2$MIM][Cl] and 1.08 ± 0.01 for [C$_2$MIM][BF$_4$]. In a separate study, Biskos et al. examined the hygroscopicity of pure (NH$_4$)$_2$SO$_4$ particles with d$_{m,dry}$ values of 20 and 40 nm.[7] At 80% RH, the 20 and 40 nm (NH$_4$)$_2$SO$_4$ particles had GFs of ~1.40,[7] well in excess of the corresponding GF values of the ILs shown in Figure 4.1.

4.4.2. Attenuated Total Reflection-Fourier Transform Infrared Spectra of Ionic Liquid Thin Films

The IR spectra of purified, dry [C$_2$MIM][Cl] and [C$_2$MIM][BF$_4$] on ZnSe ATR crystals are shown in Figure 4.2a and Figure 4.3a, respectively. The spectra are calculated as –log (S/S$_o$), where S$_o$ is the IR beam intensity penetrating through the clean ZnSe ATR crystal and S is the beam intensity penetrating through the crystal coated with a thin film of dry IL. The spectra are consistent with previous IR studies of these ILs.[9-19] Spectral bands in the region from 3200–3000 cm^{-1} are attributed to the coupled aromatic ring C–H stretching vibrations of the imidazolium hydrogen atoms, while those between 3000–2850 cm^{-1} can be assigned to the aliphatic C–H stretches of the CH$_2$ and CH$_3$ groups of the ethyl chain, and of the CH$_3$ group bonded directly to the [C$_2$MIM]$^+$ ring.[9-16,19] In the spectrum of the dry [C$_2$MIM][Cl] salt (Figure 4.2a), the band at ca. 3048 cm^{-1} is the so called "Cl$^-$ interaction band", characteristic of stretching vibrations of C2–H and C4–H or C5–H-bonds interacting with the Cl$^-$ anion.[13,17,18] The dry [C$_2$MIM][BF$_4$] spectrum (Figure 4.3a) exhibits similar C–H stretching bands at 3165 cm^{-1} and 3123 cm^{-1} attributed to bonding of BF$_4^-$ with C4–H (or C5–H) and C2–H, respectively.[9,19] Prominent imidazolium ring stretching modes are seen at 1572 cm^{-1} and 1172 cm^{-1} for [C$_2$MIM][Cl][13] and 1576 cm^{-1} and 1171 cm^{-1} for [C$_2$MIM][BF$_4$].[9,10] Stretching modes of the BF$_4^-$ anion (Figure 4.3a) are the sharp peaks around 1286 cm^{-1} and at 755 cm^{-1} and the broad peak centered at ca. 1070 cm^{-1}.[9,10]

Figure 4.2. (a) ATR-FTIR spectra of dry [C$_2$MIM][Cl] on ZnSe; (b) ATR-FTIR spectra of [C$_2$MIM][Cl] after exposure to increasing RH values of 4, 15, 27, 43, 49, 58, 72, and 79% (the background contribution from the dry [C$_2$MIM][Cl] was subtracted); (c) ATR-FTIR spectra of 1:1 [C$_2$MIM][Cl]–water and 1:1 [C$_2$MIM][Cl]–H$_2$O/D$_2$O mixtures on ZnSe.

Figure 4.3. (a) ATR-FTIR spectra of dry [C$_2$MIM][BF$_4$] on ZnSe; (b) ATR-FTIR spectra of [C$_2$MIM][BF$_4$] after exposure to increasing RH values of 3, 22, 41, 61, 71, 78, and 89% (the background contribution from the dry [C$_2$MIM][BF$_4$] was subtracted); (c) ATR-FTIR spectra of 1:1 [C$_2$MIM][BF$_4$]–water and 1:1 [C$_2$MIM][BF$_4$]–H$_2$O/D$_2$O mixtures on ZnSe.

Figures 4.2b and Figure 4.3b show the IR spectra of [C₂MIM][Cl] and [C₂MIM][BF₄], respectively, after exposure to water vapor at various levels of RH. The extent of water uptake was monitored using ATR-FTIR by exposure of [C₂MIM][Cl] and [C₂MIM][BF₄] thin films to water vapor in the sealed ATR cell at different levels of RH at 295 K. After each RH adjustment, spectra were collected until the band intensities stopped changing to ensure that equilibrium was attained. It typically took ~20 min for the system to equilibrate. The spectra of the corresponding dry IL films were subtracted to emphasize changes induced by the uptake of water vapor. Note that this subtraction does not fully eliminate the bands attributable to IL vibrations because the refractive index of the film changes upon water uptake, thus affecting the penetration depth of the evanescent wave. The stronger bands that grow in the spectra are due to water vibrations. The growth of weaker bands is from an increase in the effective amount of material probed by the IR beam.

For [C₂MIM][Cl], uptake of water vapor produces a broad O–H peak centered at 3378 cm⁻¹ (Figure 4.2b). Other prominent feature from water are recognized as the bending band at 1637 cm⁻¹ and a broad band at ~2109 cm⁻¹ assigned to a combination of the bending mode and a far-IR band associated with a librational motion of sterically-hindered water molecules (Figure 4.2b).[20] As illustrated in Figure 4.2b, the intensity of these bands increases concomitantly with the increase in RH from the added water vapor. The slightly red-shifted [C₂MIM]⁺ ring bands (at 1568 cm⁻¹ and 1167 cm⁻¹) and blue-shifted aromatic C–H stretching bands also increase with RH (Figure 4.2b), though this increase is likely due to the change in the IR beam penetration depth mentioned above.

Compared to [C₂MIM][Cl] (Figure 4.2b), the interaction of water vapor with [C₂MIM][BF₄] (Figure 4.3b) leads to very different IR spectra in the O–H stretching region. At

low RH, there are two well-resolved bands, which can be assigned as the ν_3 asymmetric stretch at 3640 cm^{-1} and the ν_1 symmetric stretch at 3562 cm^{-1} of a water molecule that is H-bonded to two BF_4^- anions, as suggested previously.[19,21-24] As the RH is increased to ~90% RH, the intensities of the ν_3 and ν_1 O–H stretches increase and the positions shift to ~3625 cm^{-1} and ~3568 cm^{-1}, respectively. A "liquid-like" water peak at 3454 cm^{-1} and a shoulder at 3270 cm^{-1} also appear and grow, indicative of formation of water aggregates. At higher RHs, there is also an increase in the ring bands associated with the $[C_2MIM]^+$ cation (at 1576 cm^{-1} and 1171 cm^{-1}).

The O–H stretching region is sensitive to H-bonding and can offer insight into structural information on IL–water interactions. However, a strong coupling between the ν_3 asymmetric stretch and ν_1 symmetric stretches in water complicates interpretation of the spectrum and makes comparison with results from MD simulations difficult. To produce spectra that were free of such coupling effects, ATR-FTIR spectra of ILs mixed with either pure water or a mixture of ultrapure water in excess D_2O (H_2O/D_2O), consisting primarily of D_2O and HOD molecules, were compared. The IR spectra of 1:1 water and H_2O/D_2O solutions of $[C_2MIM][Cl]$ and $[C_2MIM][BF_4]$ are shown in Figures 4.2c and 4.3c, respectively. We note that for the solution of $[C_2MIM][Cl]$ in water, the most prominent peak is a broad O–H stretch at ~3380 cm^{-1}, identical to the band observed in the IL film exposed to water vapor (Figure 4.2b). Therefore, intentional mixing of $[C_2MIM][Cl]$ and water produces the same type of IL–water solution as $[C_2MIM][Cl]$ absorbing water vapor from ambient air.

For the $[C_2MIM][Cl]$–H_2O/D_2O mixture, the O–D stretches of HOD and D_2O appear around 2517 cm^{-1}. The weaker band at ~3400 cm^{-1} corresponds to the decoupled O–H stretch in the $[C_2MIM][Cl]$–H_2O/D_2O mixture. The significant red-shift relative to gas-phase HOD (3707 cm^{-1}) and the width of this band are consistent with a strong H-bonding interaction, most likely

with the Cl⁻ anion (although interaction with other water molecules cannot be ruled out based on the spectrum). In free HOD–Cl⁻ complexes, the O–H stretch is even more red-shifted relative to gas-phase HOD (down to 3156 cm⁻¹).[25] The smaller red-shift observed in the IL suggests that the strength of the interaction between water and Cl⁻ is subdued (Figure 4.2c).

In the case of the [C₂MIM][BF₄]–water solution, there are two discernible O–H stretches seen in Figure 4.3c, attributed to the v_3 asymmetric band at ~3640 cm⁻¹ and v_1 symmetric band at ~3561 cm⁻¹. The bands are identical in appearance to the corresponding bands in the IL film exposed to water vapor. In the [C₂MIM][BF₄]–H₂O/D₂O mixture, the decoupled O–H stretch from HOD appears at 3601 cm⁻¹ and the v_3 and v_1 bands of the D₂O molecules shift to ~2699 cm⁻¹ and ~2605 cm⁻¹, respectively. The narrow width and relatively high vibrational frequency of the decoupled O–H stretch confirms previous suggestion[19,21] that water molecules in [C₂MIM][BF₄] tend to be isolated from each other and interact primarily with the IL components.

Presence of water indirectly affects the C–H stretching modes in the cation, and this effect is seen in Figures 4.2c and 4.3c. The C–H stretching bands in [C₂MIM][Cl] (Figure 4.2c) are blue-shifted from the corresponding bands in the dry IL (Figure 4.2a). This blue-shift reflects weakened interactions between Cl⁻ and the cation. This effect is much smaller in [C₂MIM][BF₄]: the aromatic C–H stretching bands at ~3166 cm⁻¹ and ~3123 cm⁻¹ for both the water and H₂O/D₂O solutions (Figure 4.3c) are essentially not shifted from the dry IL (Figure 4.3a).

4.4.3. Equilibrium Molar Fractions of Water in Ionic Liquids

One of the key advantages of the TDMA measurements is that one can calculate χ_w in the humidified particles exactly if the shapes and densities of the particles are known. Assuming that

the nanoparticles are homogeneous spheres and that their densities are not substantially different

from the densities of the corresponding bulk IL–water mixtures, one can derive the following

relationship between GF and χ_w (eq 4.1):

$$\frac{\chi_w}{1-\chi_w} = \left(\frac{MW_{IL}}{MW_w}\right)\left(\frac{\rho_{solution}(\chi_w)}{\rho_{IL}}GF^3 - 1\right) \quad (4.1)$$

In this equation, MW is molecular weight, ρ is density, and the subscripts IL, w, and solution

refer to IL, water, and their mixture, respectively. The $\rho_{solution}$ data for [C$_2$MIM][BF$_4$] from Rilo

et al.[26] were fitted to an empirical dependence on χ_w, and eq 4.1 was solved numerically for χ_w

for every measured GF. For example, χ_w of [C$_2$MIM][BF$_4$] nanoparticles at 83% RH was 0.725

± 0.004. Literature data for the physical properties of imidazolium-based ILs containing Cl$^-$ are

scarce, so a formula based on an ideal solution behavior (i.e. additive volumes) was also derived

(eq 4.2):

$$\frac{\chi_{w,ideal}}{1-\chi_{w,ideal}} = \left(\frac{MW_{IL}}{MW_w}\right)\left(\frac{\rho_w}{\rho_{IL}}\right)(GF^3 - 1) \quad (4.2)$$

For [C$_2$MIM][BF$_4$], both eqs 4.1 and 4.2 could be used to calculated χ, whereas for [C$_2$MIM][Cl]

particles only $\chi_{w,ideal}$ could be calculated due to the lack of density data for [C$_2$MIM][Cl]–water

solutions. We believe eq 4.2 is a reasonable alternative to the more accurate eq 4.1 because it

produces almost the same result, $\chi_{w,ideal} = 0.739 ± 0.004$ for [C$_2$MIM][BF$_4$] at 83% RH. For

[C$_2$MIM][Cl] nanoparticles, $\chi_{w,ideal}$ was found to be 0.889 ± 0.004 at 83% RH.

Strictly speaking, the equilibrium value of χ_w in a bulk liquid and in a small droplet

exposed to the same RH will not be the same because of the Kelvin effect (reduction in the

equilibrium vapor pressure of a volatile solute above a curved surface). The Kelvin effect makes

the hygroscopic GF of nanoparticles size dependent as demonstrated in previous work on

85

hygroscopic growth of NaCl nanoparticles.[6] However, for particles larger than 20 nm, this effect

is relatively small and quantitatively predictable from bulk thermodynamics properties.[27,28] The

Kelvin correction factor for the IL nanoparticles was estimated using surface tension versus

water content measurements from Rilo et al.[26] For the ~27 nm nanoparticles, the anticipated

reduction in χ_w compared to bulk is less than 5% for $[C_2MIM][BF_4]$. The Kelvin effect

correction could not be calculated for $[C_2MIM][Cl]$ due to lack of available surface tension data

for the $[C_2MIM][Cl]$–water mixtures, but we believe it to be similarly small. In view of the

small size of the Kelvin effect corrections, the reported χ_w values were not corrected for this

effect.

Figure 4.4a shows the dependence of the χ_w in the ILs as a function of the RH, obtained

by a direct inversion of the growth curves using eqs 4.1 and 4.2. With the exception of the small

Kelvin effect correction and the uncertainty introduced by the unknown density of the

$[C_2MIM][Cl]$–water mixtures, the accuracy of the χ_w values should be comparable to that of bulk

measurements. RH is intentionally placed on the vertical axis to discuss this dependence in

terms of Raoult's law (RH can be interpreted as the equilibrium vapor pressure of water above

the IL–water mixture). The behavior of $[C_2MIM][Cl]$ and $[C_2MIM][BF_4]$ are distinctly different.

$[C_2MIM][BF_4]$ exhibits relatively small positive deviations from Raoult's law. This suggests that

the strength of $[C_2MIM][BF_4]$–water interactions is weaker than or comparable in strength to the

interactions of water–water and IL–IL. This is consistent with the narrow widths and small red-

shifts of the O–H stretching bands in ATR-FTIR spectra of $[C_2MIM][BF_4]$ (Figure 4.3), which

show that water molecules are not significantly perturbed by interactions with $[C_2MIM][BF_4]$,

and conversely, they do not significantly affect vibrations of the cation and the anion. In contrast

to $[C_2MIM][BF_4]$, $[C_2MIM][Cl]$–water mixtures exhibit significant negative deviation in terms

of Raoult's law as a result of the very strong interactions between water and Cl⁻. This is again

consistent with the IR spectra of the aqueous [C₂MIM][Cl] solutions (Figure 4.2), which display

a strongly red-shifted and broad O–H stretching band.
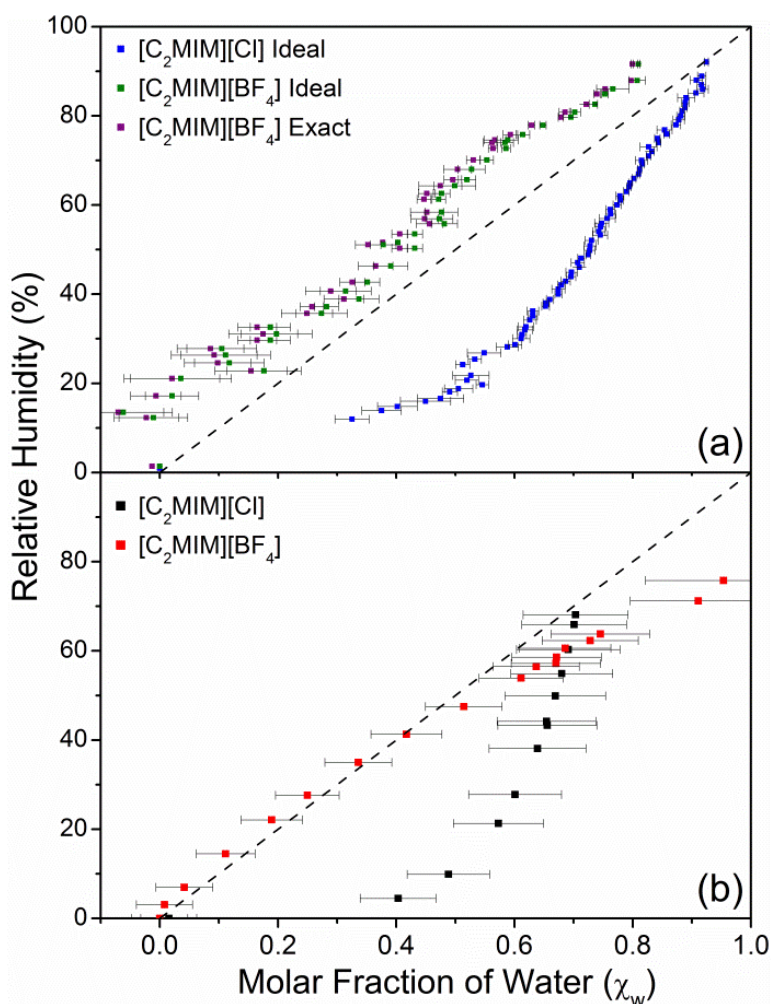
Figure 4.4. Molar fractions of water (χ_w) as a function of RH: (a) calculated from the GF values using eq 4.1 (actual densities) and eq 4.2 (ideal solution approximation); (b) inferred from the ATR-FTIR spectra. The dashed line on both plots represents Raoult's law in terms of an ideal solution.

From the ATR-FTIR measurements, χ_w in the IL film exposed to water vapor can be estimated by comparing the relative areas of the C–H and O–H stretching vibrations. We calibrated this method by recording the ATR-FTIR spectra of pre-mixed aqueous solutions of ILs of known composition. This method is necessarily approximate because presence of water may affect the band strengths of the C–H vibrations, and *vice versa*, the O–H stretch band strengths may be influenced by the IL components to a different extent depending on the extent of dilution. Furthermore, it is difficult to cleanly separate the overlapping C–H and O–H stretches from each other because of the RH-dependent shifts in the positions of the bands. Nevertheless, the RH vs. χ_w curves obtained from the ATR-FTIR measurements (Figure 4.4b) are in good qualitative agreement with the nanoparticle hygroscopicity data. The data shown in both panels of Figure 4.4 complement each other: the ATR-FTIR results are most accurate at low RH, whereas the nanoparticle hygroscopicity results are most accurate at higher RH values (excluding values > 85% RH due to the high sensitivity of RH to temperature).

4.4.4. Molecular Dynamics Simulations of 1:1 Ionic Liquid–Water Mixtures.

MD simulations of [C$_2$MIM][Cl] and [C$_2$MIM][BF$_4$] mixed with water in 1:1 molar ratios were carried out to elucidate the interactions of water with the IL components and help interpret the observed FTIR spectra. Figure 4.5 and Table 4.1 compare water–water and water–anion H-bond distributions in the ILs with those in bulk water. Water–water H-bonding interactions are mostly abolished in [C$_2$MIM][Cl] and replaced by water–anion interactions. In contrast, both water–water and water–anion interactions coexist in [C$_2$MIM][BF$_4$]. Thus, the MD simulations are consistent with the IR spectra of water in ILs, which revealed strong interactions between water and the anion in [C$_2$MIM][Cl], and co-existence of both water–anion and water–water

interactions in [C$_2$MIM][BF$_4$]. Representative snapshots depicting the distribution of water in

the ILs and interactions of water with the IL components are shown in Figure 4.6.
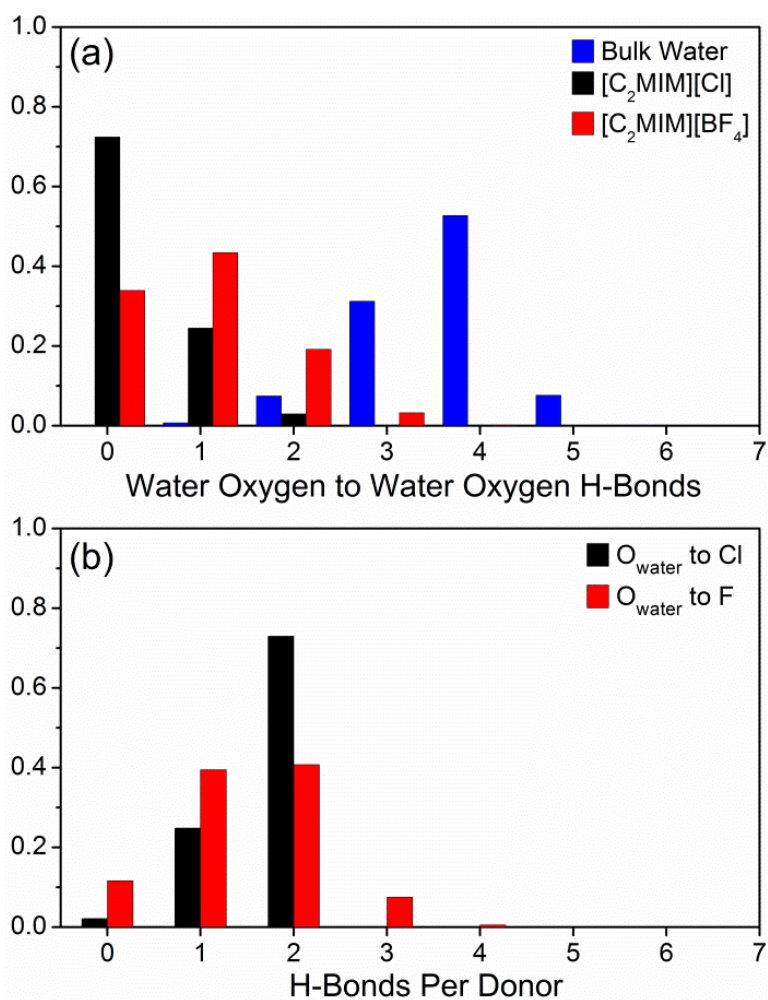
Figure 4.5. Hydrogen bond (H-bond) distribution histograms from MD simulation trajectories of (a) water oxygen (O$_{water}$) to O$_{water}$ H-bonds in 1:1 mixtures of water with either bulk water, [C$_2$MIM][Cl], or [C$_2$MIM][BF$_4$] and (b) O$_{water}$ donor H-bonds to either chloride or fluorine anions.

Table 4.1. Water Solvation Predicted by MD Simulations[†]

Water–Water	First Shell (Å)	c.n.	H-bonds
Bulk Water	3.35	4.7	3.6
[C$_2$MIM][Cl]	3.25	0.36	0.3
[C$_2$MIM][BF$_4$]	3.65	1.15	0.9
Water–Anion	**First Shell (Å)**	**c.n.**	**H-bonds**
O$_{water}$ to Cl$^-$	4.05	1.85	1.7
O$_{water}$ to F$^-$	3.55	0.55	1.5
O$_{water}$ to B$^-$	4.65	1.61	0

[†] First coordination shell location, coordination number (c.n.), and average number of hydrogen bonds (H-bonds) for water–water and water–anion interactions in 1:1 mixtures of water with either bulk water, [C$_2$MIM][Cl], or [C$_2$MIM][BF$_4$].
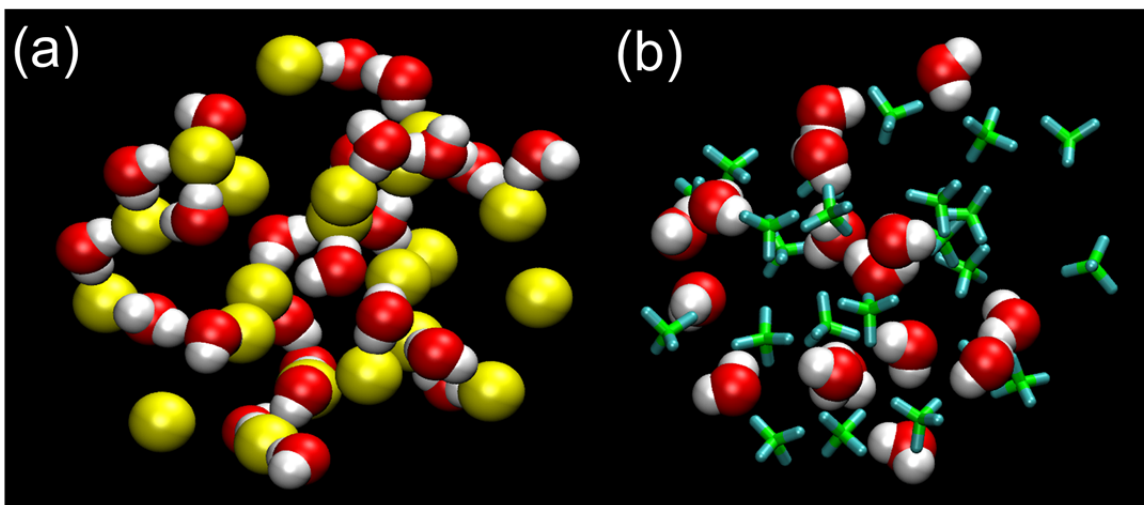
Figure 4.6. Representative MD simulation snapshots of [C$_2$MIM][Cl] (a) and [C$_2$MIM][BF$_4$] (b) mixed with water in 1:1 molar ratios. Water molecule are shown as filled spheres and colored by atom (red: oxygen; white: hydrogen). Cl$^-$ ions are shown as yellow, filled spheres. BF$_4^-$ ions are represented as licorice and colored by atom (green: boron; cyan: fluoride). Cation molecules were removed for clarity.

To identify H-bond configurations in the mixed systems, a geometric criterion commonly used for bulk water was applied (donor-acceptor distance < 3.5 Å and donor-H-acceptor angle > 140 °). The water oxygen radial distribution function (Figure 4.7a) yields similar locations for the first coordination shell and a similar trend in coordination number as the H-bond distributions mean values (Table 4.1), suggesting that this geometric criterion adequately describes H-bond interactions in the mixed system. Figure 4.7b shows the water oxygen to anion (O_{water}–anion) radial distribution functions for the 1:1 IL–water mixtures. Due to the smaller size of the fluorine atom, the average O_{water}–F separation in [C_2MIM][BF_4] is significantly smaller than the O_{water}–Cl^- separation in [C_2MIM][Cl]. However, the interaction strength is larger in the latter because the negative charge in BF_4^- is more spatially distributed. The ionic complex $Cl^-\cdots H_2O$ has been investigated in the gas-phase by a number of experimental and theoretical methods;[29] its binding energy is 59 kJ mol^{-1}. In contrast, no experiments or calculations have been performed on the $BF_4^-\cdots H_2O$ complex to the best of our knowledge. It would be of interest to investigate the nature of H-bonding in this complex in the future.

We also predicted the frequency distributions corresponding to the O–H stretching vibration of water in [C_2MIM][Cl], [C_2MIM][BF_4], and bulk water from the MD simulations, using an empirical relation between the electric field along the O–H bond and the O–H vibrational frequency derived for the SPC/E water model by Smith et al.[30] Figure 4.8 compares these results with the ATR-FTIR data for the O–H stretch of HOD molecules in [C_2MIM][Cl], [C_2MIM][BF_4], and bulk water. The simulations qualitatively reproduce the experimental observations. Specifically, the red-shift in the O–H stretch is predicted to be smaller in [C_2MIM][BF_4] compared to [C_2MIM][Cl], the red-shift in [C_2MIM][Cl] approaches that in bulk water, and the width of the bands in the largest in bulk water. This level of agreement gives us

confidence that the force-fields chosen for the MD simulations correctly capture the essential

interactions in the IL–water mixtures, and validates the differences in ion–water and water–water

interactions in [C$_2$MIM][BF$_4$] vs. [C$_2$MIM][Cl] predicted by the MD simulations.
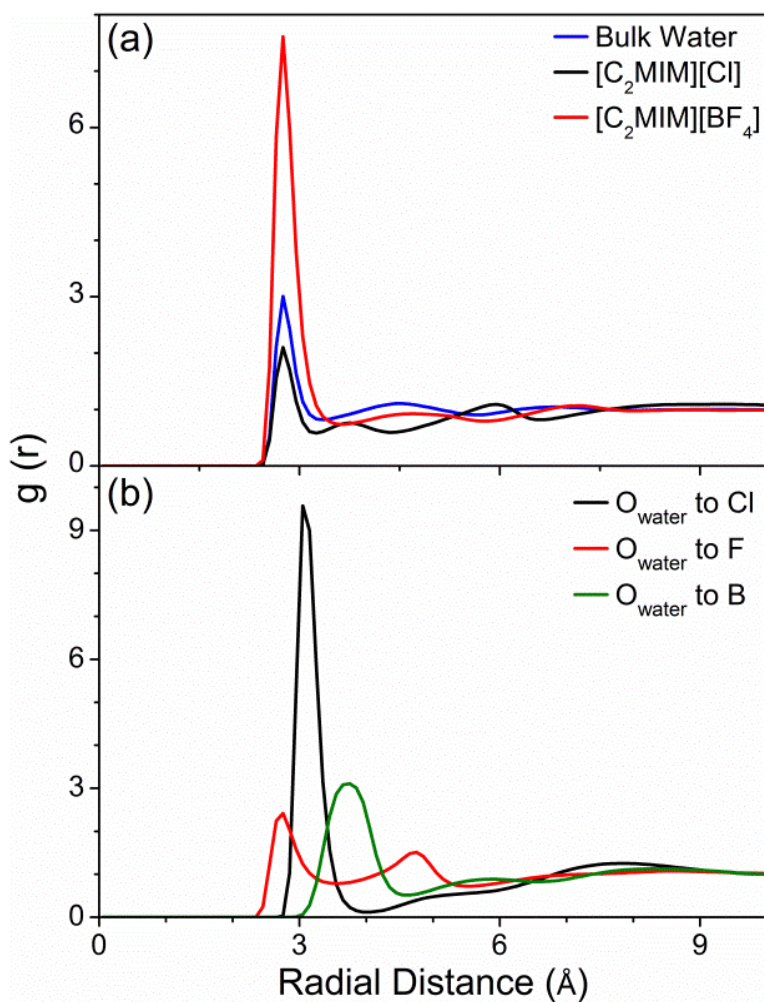
Figure 4.7. Radial distribution functions from MD simulations of (a) water oxygen (O$_{water}$) to O$_{water}$ in 1:1 mixtures of water with either bulk water, [C$_2$MIM][Cl], or [C$_2$MIM][BF$_4$] and (b) O$_{water}$ around ionic liquid anions. Separate radial distribution functions for fluorine and boron were calculated for [C$_2$MIM][BF$_4$].
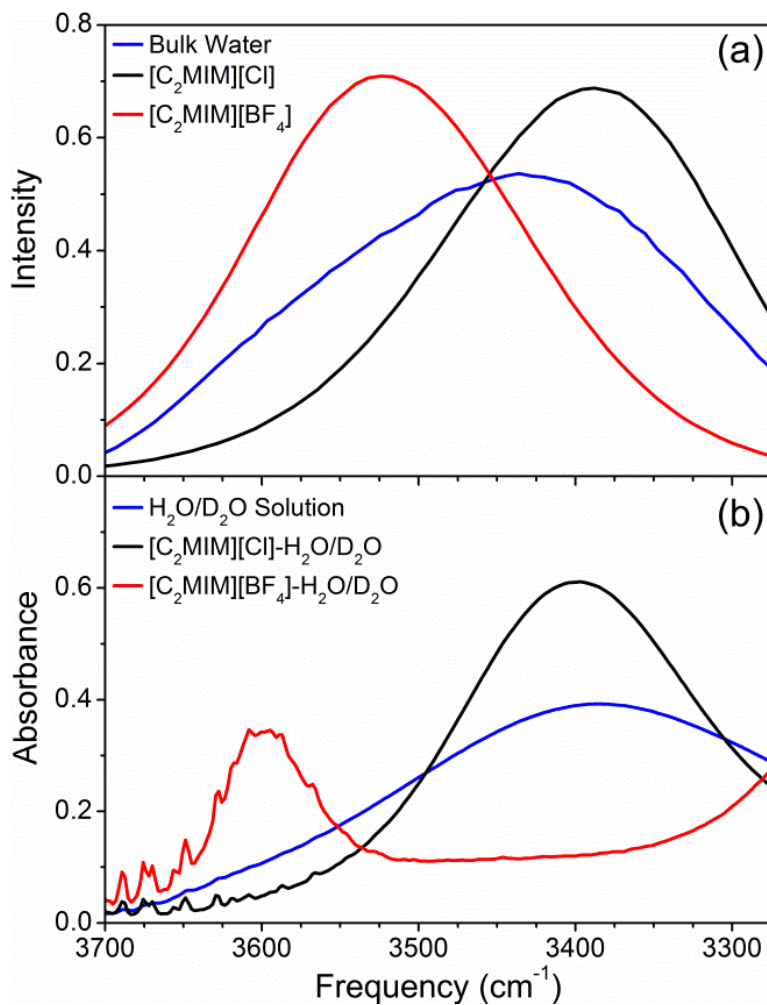
Figure 4.8. (a) Simulated frequency distributions corresponding to the O–H stretching vibration of water in either bulk water, [C₂MIM][Cl], or [C₂MIM][BF₄]. (b) Shown for comparison are the experimental ATR-FTIR spectra of the decoupled O–H stretches in a bulk solution of H_2O in excess D_2O (H_2O/D_2O) and in ionic liquids–H_2O/D_2O mixtures. ATR-FTIR spectra for the ionic liquid–H_2O/D_2O mixtures were baseline corrected for easier comparison.

4.5. Conclusion

In this study, we have combined aerosol hygroscopicity methods, IR spectroscopy, and MD simulations to gain new insights into the interaction of water vapor with IL nanoparticles and thin films. Although the ILs under investigation, [C$_2$MIM][Cl] and [C$_2$MIM][BF$_4$], share the same cation and only differ in the inorganic anion, their interaction with water is remarkably different. First, [C$_2$MIM][Cl] takes up more water under equilibrium conditions than [C$_2$MIM][BF$_4$] at all RH values. This is evident from the larger hygroscopic GFs for the [C$_2$MIM][Cl] nanoparticles and stronger water IR absorption bands for the [C$_2$MIM][Cl] thin films exposed to water vapor. Second, the equilibrium vapor pressure above [C$_2$MIM][Cl] exhibits negative deviation from Raoult's law, whereas that above [C$_2$MIM][BF$_4$] deviates from Raoult's law in a positive sense. Third, the shapes of the O–H stretching bands for water molecules absorbed into ILs are quite different. At low χ_w, the ν_3 and ν_1 bands in [C$_2$MIM][BF$_4$] are narrow, well resolved, and not significantly shifted from the O–H stretches in free water. In contrast, for [C$_2$MIM][Cl], these bands coalesce into one broad O–H stretching band characterized by a significant red-shift. At higher χ_w, additional bands in [C$_2$MIM][BF$_4$] appear in the O–H stretching region characteristic of water aggregates. Fourth, MD simulations predict that water is more strongly associated with the anions than itself, especially so in [C$_2$MIM][Cl]. This is evident from low water–water and high water–anion coordination numbers.

The following picture emerges from this combination of the experimental observations and MD simulations. When ILs are exposed to low levels of RH, absorbed water molecules are primarily interacting with the anion. This interaction is considerably stronger in the case of [C$_2$MIM][Cl], and this accounts for its large hygroscopic GF, significant O–H red-shift, and large deviations from Raoult's law. The behavior of the [C$_2$MIM][BF$_4$]–water mixture is much closer

to that of an ideal solution because of more balanced interactions between the mixture components. At higher RH, when enough water is absorbed by the ILs, the relative role of water–water interaction increases, and small clusters and chains of water molecules exist in the IL–water solution.

The amount of water that ILs can absorb under equilibrium conditions at any given RH is finite but quite substantial. For example, [C$_2$MIM][Cl] and [C$_2$MIM][BF$_4$] forgotten on a shelf at 83% RH will reach equilibrium χ_w of ~0.73 and ~0.89, respectively. The equilibrium values of χ_w attained at other RH values can be estimated from Figure 4.4 in this paper. The amount of time needed to reach this equilibrium will of course depend on the amount of IL. While it takes less than a second for nanoparticles (one of the chief advantages of the hygroscopic growth method described here), and less than 30 min for thin films of ILs, it will take considerably longer for bulk quantities, as previous studies cited in the introduction section suggest. Both the amount of water that can be absorbed from the air, and the timescale of this process, represent important practical knowledge about ILs considering the significant effect of absorbed water on various physicochemical properties of ILs, including density, surface tension, and ability to dissolve other compounds.

References

(1) DeCarlo, P. F.; Slowik, J. G.; Worsnop, D. R.; Davidovits, P.; Jimenez, J. L. Particle Morphology and Density Characterization by Combined Mobility and Aerodynamic Diameter Measurements. Part 1: Theory. *Aerosol Sci. Technol.* **2004**, *38*, 1185-1205.

(2) Zelenyuk, A.; Imre, D. On the Effect of Particle Alignment in the DMA. *Aerosol Sci. Technol.* **2007**, *41*, 112-124.

(3) Zhang, C.; Thajudeen, T.; Larriba, C.; Schwartzentruber, T. E.; Hogan, C. J. Determination of the Scalar Friction Factor for Nonspherical Particles and Aggregates Across the Entire Knudsen Number Range by Direct Simulation Monte Carlo (DSMC). *Aerosol Sci. Technol.* **2012**, *46*, 1065-1078.

(4) Larriba, C.; Hogan, C. J.; Attoui, M.; Borrajo, R.; Garcia, J. F.; de la Mora, J. F. The Mobility-Volume Relationship below 3.0 nm Examined by Tandem Mobility-Mass Measurement. *Aerosol Sci. Technol.* **2011**, *45*, 453-467.

(5) Martin, S. T. Phase Transitions of Aqueous Atmospheric Particles. *Chem. Rev.* **2000**, *100*, 3403-3453.

(6) Biskos, G.; Russell, L. M.; Buseck, P. R.; Martin, S. T. Nanosize Effect on the Hygroscopic Growth Factor of Aerosol Particles. *Geophys. Res. Lett.* **2006**, *33*, L07801, doi:07810.01029/02005GL025199.

(7) Biskos, G.; Paulsen, D.; Russell, L. M.; Buseck, P. R.; Martin, S. T. Prompt Deliquescence and Efflorescence of Aerosol Nanoparticles. *Atmos. Chem. Phys.* **2006**, *6*, 4633-4642.

(8) Biskos, G.; Buseck, P. R.; Martin, S. T. Hygroscopic Growth of Nucleation-Mode Acidic Sulfate Particles. *J. Aerosol Sci.* **2009**, *40*, 338-347.

(9) Katsyuba, S. A.; Dyson, P. J.; Vandyukova, E. E.; Chernova, A. V.; Vidiš, A. Molecular Structure, Vibrational Spectra, and Hydrogen Bonding of the Ionic Liquid 1-Ethyl-3-methyl-1H-imidazolium Tetrafluoroborate. *Helv. Chim. Acta* **2004**, *87*, 2556-2565.

(10) Katsyuba, S. A.; Zvereva, E. E.; Vidis, A.; Dyson, P. J. Application of Density Functional Theory and Vibrational Spectroscopy Toward the Rational Design of Ionic Liquids. *J. Phys. Chem. A* **2007**, *111*, 352-370.

(11) Snyder, R. G.; Strauss, H. L.; Elliger, C. A. Carbon-Hydrogen Stretching Modes and the Structure of n-Alkyl Chains. 1. Long, Disordered Chains. *J. Phys. Chem.* **1982**, *86*, 5145-5150.

(12) MacPhail, R. A.; Strauss, H. L.; Snyder, R. G.; Elliger, C. A. Carbon-Hydrogen Stretching Modes and the Structure of n-Alkyl Chains. 2. Long, All-Trans Chains. *J. Phys. Chem.* **1984**, *88*, 334-341.

(13) Tait, S.; Osteryoung, R. A. Infrared Study of Ambient-Temperature Chloroaluminates as a Function of Melt Acidity. *Inorg. Chem.* **1984**, *23*, 4352-4360.

(14) Talaty, E. R.; Raja, S.; Storhaug, V. J.; Dölle, A.; Carper, W. R. Raman and Infrared Spectra and ab Initio Calculations of C2-4MIM Imidazolium Hexafluorophosphate Ionic Liquids. *J. Phys. Chem. B* **2004**, *108*, 13177-13184.

(15) Heimer, N. E.; Del Sesto, R. E.; Meng, Z.; Wilkes, J. S.; Carper, W. R. Vibrational Spectra of Imidazolium Tetrafluoroborate Ionic Liquids. *J. Mol. Liq.* **2006**, *124*, 84-95.

(16) Höfft, O.; Bahr, S.; Kempter, V. Investigations with Infrared Spectroscopy on Films of the Ionic Liquid [EMIM]Tf2N. *Langmuir* **2008**, *24*, 11562-11566.

(17) Dieter, K. M.; Dymek, C. J.; Heimer, N. E.; Rovang, J. W.; Wilkes, J. S. Ionic Structure and Interactions in 1-Methyl-3-Ethylimidazolium Chloride-Aluminum Chloride Molten Salts. *J. Am. Chem. Soc.* **1988**, *110*, 2722-2726.

(18) Hitchcock, P. B.; Seddon, K. R.; Welton, T. Hydrogen-Bond Acceptor Abilities of Tetrachlorometalate(II) Complexes in Ionic Liquids. *J. Chem. Soc., Dalton Trans.* **1993**, 2639-2643.

(19) Jeon, Y.; Sung, J.; Seo, C.; Lim, H.; Cheong, H.; Kang, M.; Moon, B.; Ouchi, Y.; Kim, D. Structures of Ionic Liquids with Different Anions Studied by Infrared Vibration Spectroscopy. *J. Phys. Chem. B* **2008**, *112*, 4735-4740.

(20) Gurnett, B.; Williams, D. Structure of Water and Aqueous Solutions. In *Proceedings of the International Symposium*; Luck, W. A. P., Ed.; Verlag Chemie/Physik Verlag: Weinheim, Germany, 1974; pp 206.

(21) Cammarata, L.; Kazarian, S. G.; Salter, P. A.; Welton, T. Molecular states of Water in Room Temperature Ionic Liquids. *Phys. Chem. Chem. Phys.* **2001**, *3*, 5192-5200.

(22) Takamuku, T.; Kyoshoin, Y.; Shimomura, T.; Kittaka, S.; Yamaguchi, T. Effect of Water on Structure of Hydrophilic Imidazolium-Based Ionic Liquid. *J. Phys. Chem. B* **2009**, *113*, 10817-10824.

(23) Zhang, L. Q.; Xu, Z.; Wang, Y.; Li, H. R. Prediction of the Solvation and Structural Properties of Ionic Liquids in Water by Two-Dimensional Correlation Spectroscopy. *J. Phys. Chem. B* **2008**, *112*, 6411-6419.

(24) Fazio, B.; Triolo, A.; Di Marco, G. Local Organization of Water and its Effect on the Structural Heterogeneities in Room-Temperature Ionic Liquid/H_2O Mixtures. *J. Raman Spectrosc.* **2008**, *39*, 233-237.

(25) Horvath, S.; McCoy, A. B.; Elliott, B. M.; Weddle, G. H.; Roscioli, J. R.; Johnson, M. A. Anharmonicities and Isotopic Effects in the Vibrational Spectra of X(-) H(2)O, center dot HDO, and center dot D(2)O [X = Cl, Br, and I] Binary Complexes. *J. Phys. Chem. A* **2010**, *114*, 1556-1568.

(26) Rilo, E.; Pico, J.; Garcia-Garabal, S.; Varela, L. M.; Cabeza, O. Density and Surface Tension in Binary Mixtures of CnMIM-BF(4) Ionic Liquids with Water and Ethanol. *Fluid Phase Equilib.* **2009**, *285*, 83-89.

(27) Bahadur, R.; Russell, L. M. Effect of Surface Tension from MD Simulations on Size-Dependent Deliquescence of NaCl Nanoparticles. *Aerosol Sci. Technol.* **2008**, *42*, 369-376.

(28) Bahadur, R.; Russell, L. M. Water Uptake Coefficients and Deliquescence of NaCl Nanoparticles at Atmospheric Relative Humidities from Molecular Dynamics Simulations. *J. Chem. Phys.* **2008**, *129*, 094508.

(29) Ramos-Cordoba, E.; Lambrecht, D. S.; Head-Gordon, M. Charge-Transfer and the Hydrogen Bond: Spectroscopic and Structural Implications from Electronic Structure Calculations. *Faraday Discuss.* **2011**, *150*, 345-362.

(30) Smith, J. D.; Saykally, R. J.; Geissler, P. L. The Effects of Dissolved Halide Anions on Hydrogen Bonding in Liquid Water. *J. Am. Chem. Soc.* **2007**, *129*, 13847-13856.

Chapter 5: Effect of Alkyl Chain Length on Hygroscopicity of Nanoparticles and Thin Films of Imidazolium-Based Ionic Liquids

5.1. Abstract

This work focuses on the interaction of water vapor with ionic liquids (ILs) consisting of $[C_n MIM]^+$ ($n = 2, 4,$ or 6) cations paired with either chloride (Cl^-) or tetrafluoroborate (BF_4^-) anions to examine the effect of alkyl chain length on IL hygroscopicity. Tandem nano-differential mobility analysis (TDMA) and attenuated total reflection-Fourier transform infrared (ATR-FTIR) spectroscopy were used to study IL nanoparticles and thin films. Studying IL nanoparticles overcomes kinetic limitations potentially present in bulk experiments as true IL–water vapor equilibrium is quickly established. Growth curves recorded in TDMA experiments showed steady uptake of water vapor with increasing RH. ILs containing Cl^- absorbed more water than those containing BF_4^- over the entire RH range and IL hygroscopicity decreased with increasing alkyl chain length. The intensities of water stretching vibrations in IL thin films exposed to water vapor measured with ATR-FTIR were in qualitative agreement with the TDMA measurements. Water molar fractions for IL nanoparticles were calculated and the performance of several liquid activity coefficient models were evaluated by fits to the experimental data. These combined experimental and modeling techniques help provide a more complete picture for these two families of ILs in the presence of water.

5.2. Introduction

As discussed in chapter 4, we studied the interaction of water vapor with nanoparticles and thin films of 1-ethyl-3-methylimidazolium chloride ([C_2MIM][Cl]) and 1-ethyl-3-methylimidazolium tetrafluoroborate ([C_2MIM][BF_4]) ionic liquids (ILs). In this chapter, we have extended our previous study to examine the effect of longer alkyl chains (i.e., [C_nMIM]$^+$ (n = 2, 4, or 6) cations paired with Cl$^-$ or BF_4^- anions) on IL hygroscopicity. Their chemical structures are shown in Figure 2.2.

By aerosolizing ILs, exposing them to humidified air over a broad range of relative humidity (RH), and comparing their wet size to their initial dry size, the amount of water taken up by the particles can be quantitatively determined. In a parallel set of experiments, the nature of the interactions between ILs and water in the vapor phase is examined by attenuated total reflection-Fourier transform infrared (ATR-FTIR) measurements. ATR-FTIR spectra of [C_4MIM][Cl], [C_6MIM][Cl], [C_4MIM][BF_4], and [C_6MIM][BF_4] thin films exposed to humidified nitrogen were measured and the C–H and O–H band positions and intensities were determined as a function of RH. Equilibrium molar fractions of water (χ_w) for IL nanoparticles were calculated from hygroscopic growth factors (GFs) and the performance of several one- and two-parameter correlative liquid activity coefficient models were evaluated to fit the experimental data.

These combined experimental and modeling techniques help provide a more comprehensive picture of the behavior of absorbed water in imidazolium-based ILs. The techniques also provide a quantitative parameterization of the amount of water vapor that ILs with different alkyl chain lengths can absorb under equilibrium conditions.

5.3. Experimental Methods

The experimental conditions including the chemicals used, solution preparation, nanoparticle generation, hygroscopicity measurements, and ATR-FTIR measurements can be found in Chapter 2. Specifically, chemicals used can be found in Section 2.2.2. Solution preparation and nanoparticle generation can be found in Section 2.6.2. Hygroscopic growth measurements can be found in Section 2.7.2. ATR-FTIR measurements can be found in Sections 2.10 and 2.11.

5.4. Results and Discussion

5.4.1. Hygroscopic Growth of Ionic Liquid Nanoparticles.

Figure 5.1 shows the measured hygroscopic growth curves (from ~0 to 92% RH) for [C$_4$MIM][Cl], [C$_6$MIM][Cl], [C$_4$MIM][BF$_4$], and [C$_6$MIM][BF$_4$] nanoparticles. Our previous results for [C$_2$MIM][Cl] and [C$_2$MIM][BF$_4$], discussed in chapter 4, are also included for comparison.[1] Under dry conditions, all six ILs had initial mobility-equivalent diameters ($d_{m,dry}$) of 26.9 ± 0.1 nm. Full and size-selected particle mobility distributions for [C$_4$MIM][Cl], [C$_6$MIM][Cl], [C$_4$MIM][BF$_4$], and [C$_6$MIM][BF$_4$] are shown in Figures 5.2 and 5.3. Exposing the particles to a well-defined RH causes the particles to uptake water vapor and increase in size. In these experiments, the mobility-equivalent diameters of the wet particles ($d_{m,wet}$) in equilibrium with water vapor are measured at different RH values. The amount of water uptake by the IL particles is quantified by the GF (eq 1.1). Growth curves are obtained by plotting the measured GF as a function of RH.
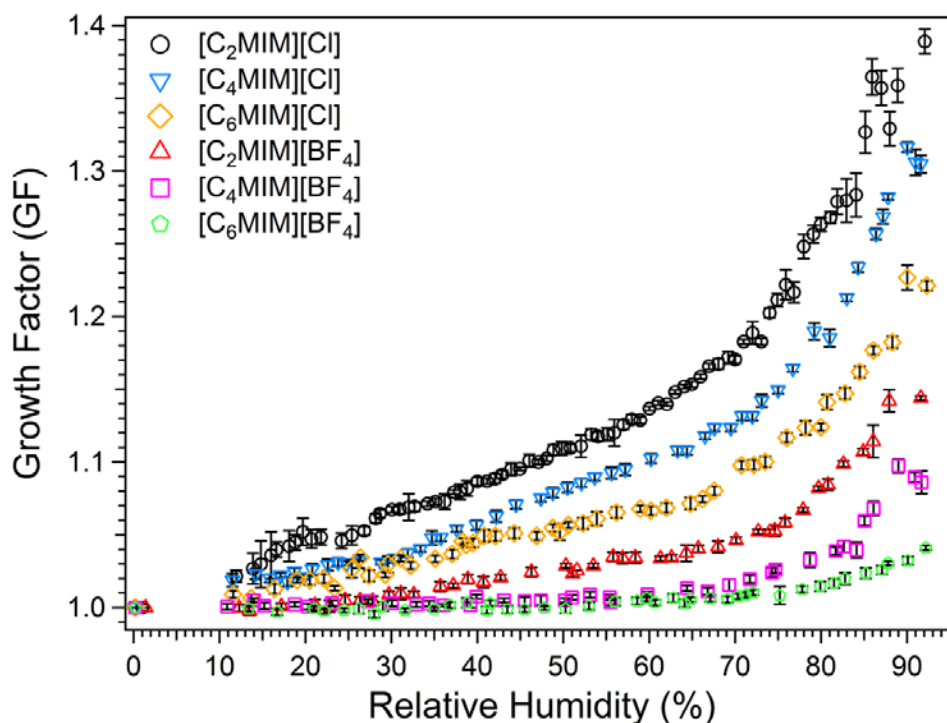
Figure 5.1. Hygroscopic growth curves of mobility equivalent diameter selected 26.9 ± 0.1 nm particles of [C₄MIM][Cl] (blue inverted triangles), [C₆MIM][Cl] (yellow diamonds), [C₄MIM][BF₄] (pink squares), and [C₆MIM][BF₄] (green pentagons). Ionic liquid growth curve data from our previous study[1] of [C₂MIM][Cl] (black circles) and [C₂MIM][BF₄] (red triangles), as discussed in chapter 4, are included for comparison. All ionic liquids exhibit a gradual increase in GF as the RH is increased. Ionic liquids containing Cl⁻ anions have larger GFs compared to those containing BF₄⁻ anions because they take up more water. The amount of absorbed water goes down as the size of the alkyl chain in the ionic liquids increases.
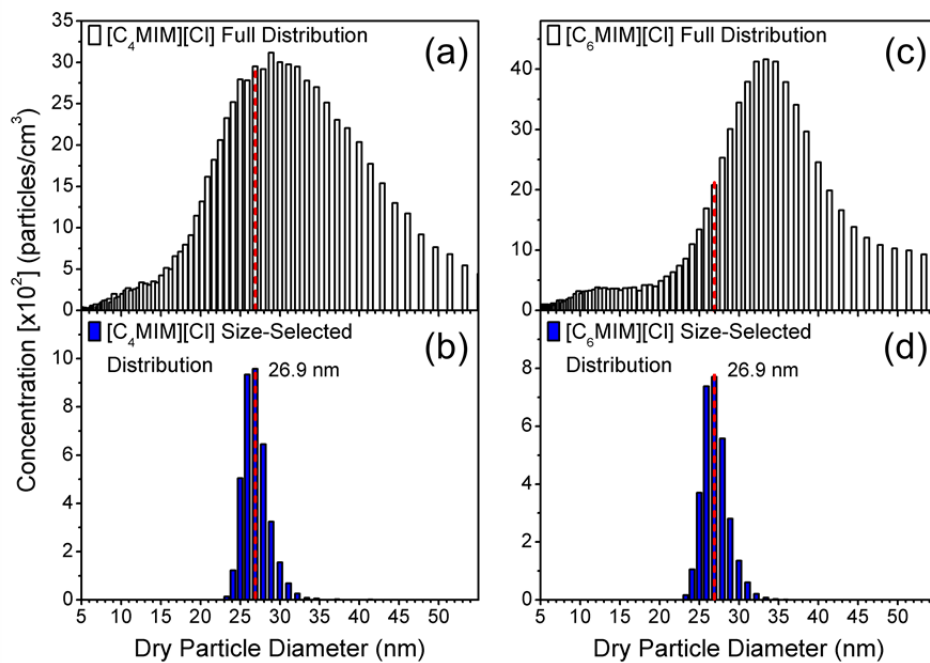
Figure 5.2. Full particle mobility size distributions of the dry [C$_4$MIM][Cl] (a) and [C$_6$MIM][Cl] (c) particles measured by the first nano-differential mobility analyzer (nano-DMA); the mobility size distributions after size selection for 26.9 ± 0.01 nm [C$_4$MIM][Cl] (b) and [C$_6$MIM][Cl] (d) particles measured by the second nano-DMA. The red, dotted lines indicate where the dry size-selected particle distributions were located in the full particle distributions.
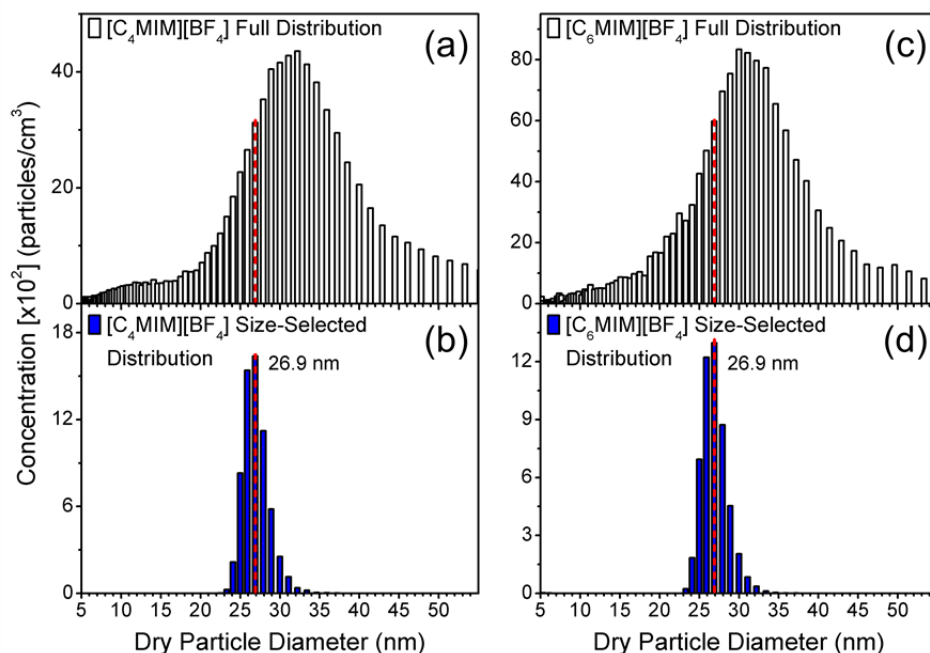
Figure 5.3. Full particle mobility size distributions of the dry [C$_4$MIM][BF$_4$] (a) and [C$_6$MIM][BF$_4$] (c) particles measured by the first nano-differential mobility analyzer (nano-DMA); the mobility size distributions after size selection for 26.9 ± 0.01 nm [C$_4$MIM][BF$_4$] (b) and [C$_6$MIM][BF$_4$] (d) particles measured by the second nano-DMA. The red, dotted lines indicate where the dry size-selected particle distributions were located in the full particle distributions.

The hygroscopicity aerosol measurements were time consuming; a single day typically provided a data set spanning 10–30% RH units. These individual experimental runs were then compiled to construct the growth curves for each IL. All GF values were averaged into 3% RH bins; each bin contained ≥ 7 measurements from several independent experimental runs. These measurements were highly reproducible as indicated by the 95% confidence intervals shown in Figure 5.1. At RH values > 85%, data became less reproducible because of the increased sensitivity of RH to temperature at these values (the RH error bars are not shown in Figure 5.1,

but they increase at higher RH). There are no data from ~ 1–10% RH because this RH range is difficult to achieve with our TDMA set-up.

In these experiments, nanoparticles were exposed to a specific RH for ~ 7 s. We ensured that equilibrium was reached on this time scale by performing additional experiments that exposed the IL nanoparticles to a specific RH for ~ 70 s. The GF values did not change with an increased interaction time. This suggests that the equilibration time was very short, in agreement with the expected fast diffusion of water molecules through IL nanoparticles. For example, using diffusion coefficient data for water in various [BMIM][BF$_4$]–water mixtures,[2] water is expected to diffuse through a 26.9 nm [BMIM][BF$_4$] nanoparticle in microseconds.

As shown in Figure 5.1, all IL growth curves exhibit a gradual increase in GF as the RH increases. Over the entire RH range, as the alkyl chain length of the [C$_n$MIM][Cl] and [C$_n$MIM][BF$_4$] (n = 2, 4, or 6) ILs increases, there is a noticeable decrease in GF (Figure 5.1). Furthermore, all three [C$_n$MIM][Cl] ILs have larger GFs compared to the three [C$_n$MIM][BF$_4$] ILs and thus the [C$_n$MIM][Cl] ILs appear to take up more water (a more quantitative analysis of water uptake accounting for differences in densities of droplets will be given below). At the highest RH values measured for the six ILs (~ 92%), the GFs of [C$_2$MIM][Cl], [C$_4$MIM][Cl], [C$_6$MIM][Cl], [C$_2$MIM][BF$_4$], [C$_4$MIM][BF$_4$], and [C$_6$MIM][BF$_4$] are 1.39 ± 0.01, 1.30 ± 0.01, 1.22 ± 0.01, 1.14 ± 0.01, 1.09 ± 0.01, and 1.04 ± 0.01, respectively. These values correspond to an increase in particle volume from water uptake by a factor of 2.69, 2.20, 1.82, 1.49, 1.30, and 1.12, respectively.

A number of inorganic, ionic compounds have well-defined deliquescence phase transitions that manifest themselves as an abrupt change in the GF at a specific RH value on their hygroscopic growth curves. [C$_2$MIM][Cl] and [C$_4$MIM][Cl] have melting points above room

temperature, and they could be expected to deliquesce at a certain RH. However, in our previous

study, we noted the absence of a deliquescence phase transition for [C$_2$MIM][Cl].[1] Likewise,

[C$_4$MIM][Cl] also showed no sign of deliquescence transition in its growth curve. These

observations could be interpreted in one of three ways. (1) Water is capable of permeating

through solid IL nanoparticles resulting in their gradual expansion, and eventual dissolution,

without a visible volume change. (2) Even trace amounts of water present in solid ILs make

them liquid. (3) Solid IL nanoparticles formed during the electrospray process may actually

behave as supercooled liquid droplets. The rapid solvent evaporation of MeOH from the

electrosprayed droplets, slow nucleation of the IL crystals, and small size of the droplets may not

allow enough time for crystallization in the evaporating droplets. From visual observations made

in our lab, allowing [C$_2$MIM][Cl] and [C$_4$MIM][Cl] to be exposed to ambient air on a lab bench

will result in both ILs to uptake water vapor and liquify. The other four ILs are liquid at room

temperature and thus we would not expect to observe a deliquescence phase transition in their

growth curves, which is borne out by the observations.

5.4.2. Attenuated Total Reflection-Fourier Transform Infrared Spectra of Ionic Liquid Thin Films

The infrared spectra of purified, dry [C$_4$MIM][Cl], [C$_6$MIM][Cl], [C$_4$MIM][BF$_4$], and

[C$_6$MIM][BF$_4$] on ZnSe ATR crystals are shown in Figures 5.4a, 5.5a, 5.6a, and 5.7a,

respectively. The spectra are calculated as $-\log (S/S_0)$, where S_0 is the single beam intensity

through the clean ZnSe ATR crystal and S is the beam intensity through the ATR crystal coated

with a layer of dry IL. IR spectra of these ILs have been collected in multiple studies[1,3-18] and

have been assigned. Spectral bands in the region from 3200–3000 cm^{-1} are attributed to the

coupled aromatic C–H stretching vibrations of the imidazolium ring, while those between 3000–2850 cm^{-1} can be assigned to the aliphatic C–H stretches of the CH_2 and CH_3 groups of the butyl and hexyl chains, and the CH_3 group bonded directly to the $[C_nMIM]^+$ ring.[3-9]
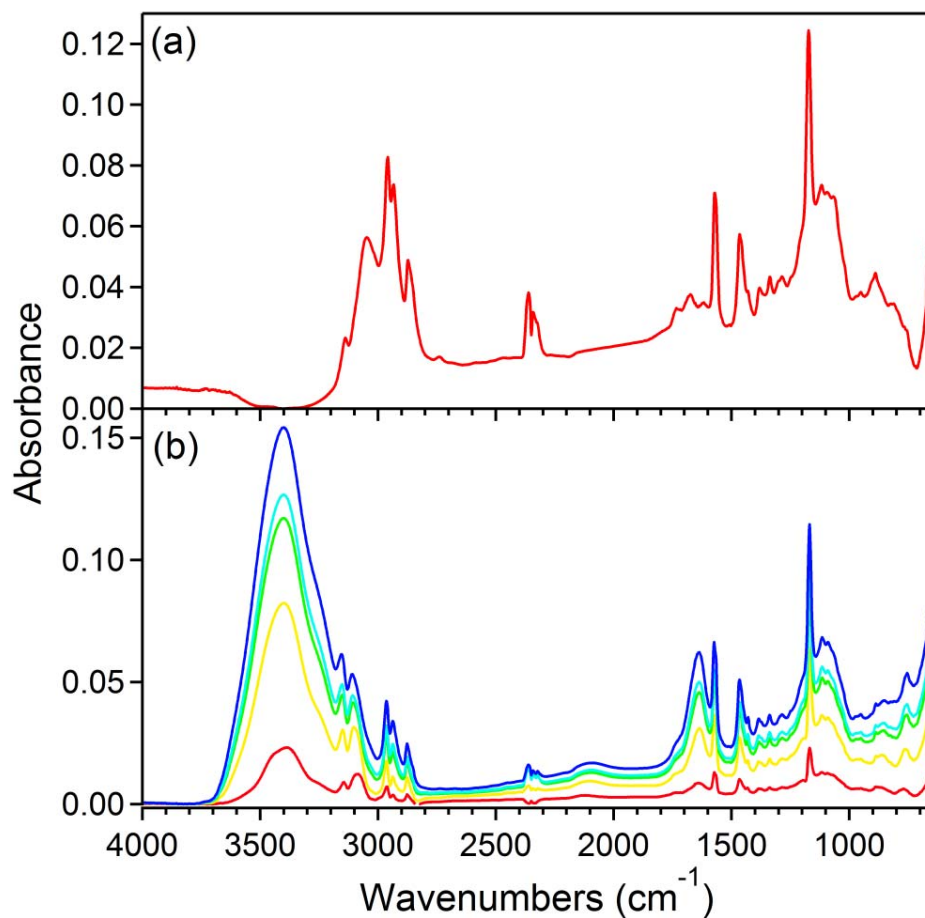
Figure 5.4. (a) ATR-FTIR spectra of dry [C$_4$MIM][Cl] on ZnSe. (b) Changes in ATR-FTIR spectra of [C$_4$MIM][Cl] after exposure to RH values of 3, 36, 62, 72, and 84% (larger RH values correspond to the more intense O–H stretching bands). The spectra after water adsorption onto [C$_4$MIM][Cl] were corrected by subtracting the spectrum of the dry [C$_4$MIM][Cl].
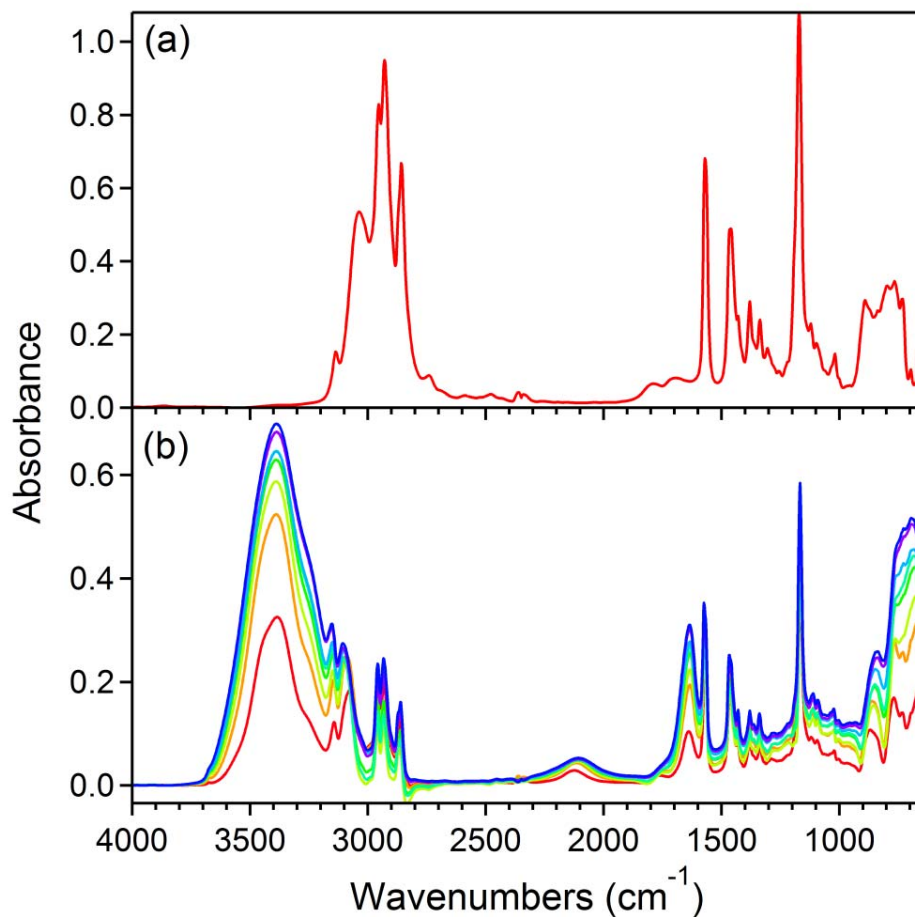
Figure 5.5. (a) ATR-FTIR spectra of dry [C$_6$MIM][Cl] on ZnSe. (b) Changes in ATR-FTIR spectra of [C$_6$MIM][Cl] after exposure to RH values of 4, 18, 43, 48, 57, 63, 80, and 84% (larger RH values correspond to the more intense O–H stretching bands). The spectra after water adsorption onto [C$_6$MIM][Cl] were corrected by subtracting the spectrum of the dry [C$_6$MIM][Cl].
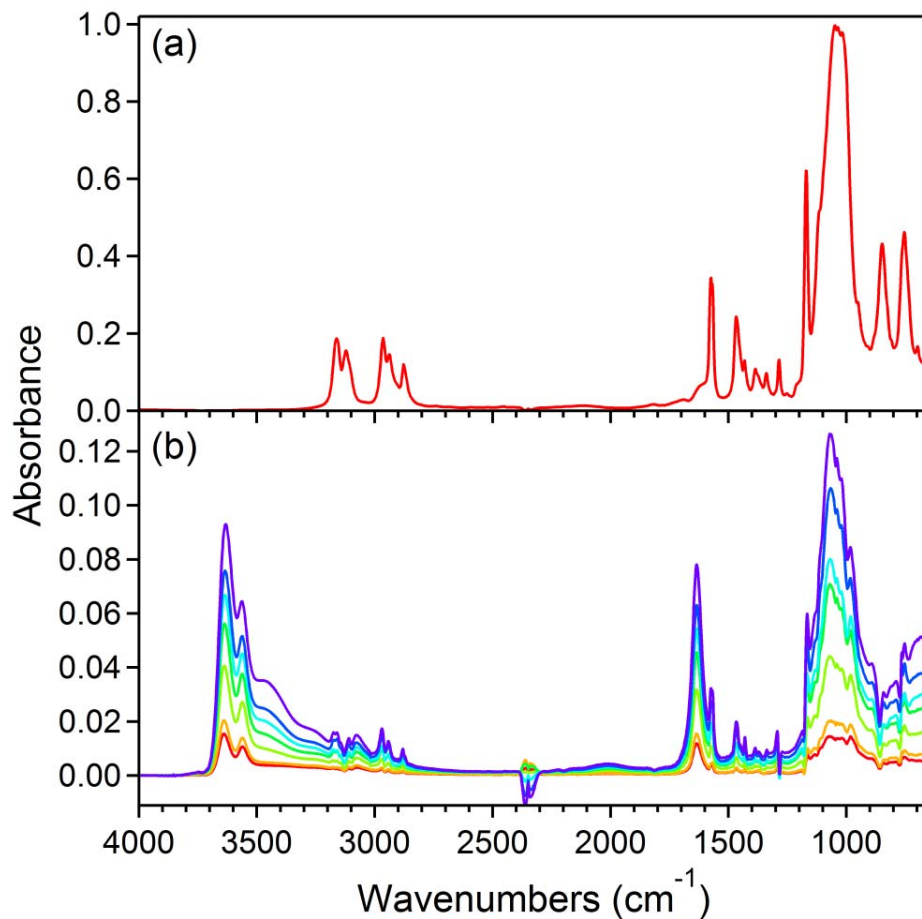
Figure 5.6. (a) ATR-FTIR spectra of dry [C₄MIM][BF₄] on ZnSe. (b) Changes in ATR-FTIR spectra of [C₄MIM][BF₄] after exposure to RH values of 11, 15, 32, 46, 57, 67, and 82% (larger RH values correspond to the more intense O–H stretching bands). The spectra after water adsorption onto [C₄MIM][BF₄] were corrected by subtracting the spectrum of the dry [C₄MIM][BF₄].
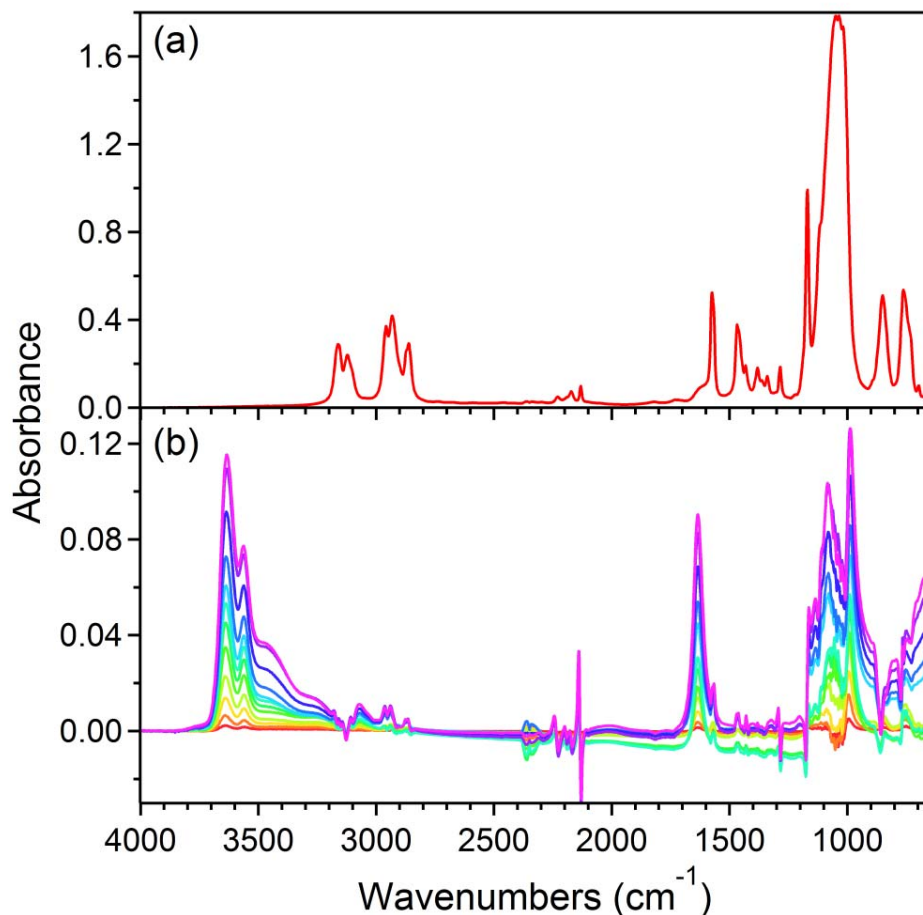
Figure 5.7. (a) ATR-FTIR spectra of dry [C$_6$MIM][BF$_4$] on ZnSe. (b) Changes in ATR-FTIR spectra of [C$_6$MIM][BF$_4$] after exposure to RH values of 2, 4, 9, 15, 24, 31, 36, 40, 48, 64, 77, and 81% (larger RH values correspond to the more intense O–H stretching bands). The spectra after water adsorption onto [C$_6$MIM][BF$_4$] were corrected by subtracting the spectrum of the dry [C$_6$MIM][BF$_4$].

In the spectra of the dry [C$_4$MIM][Cl] and [C$_6$MIM][Cl] (Figures 5.4a and 5.5a, respectively), the band at 3040 cm^{-1} and 3041cm^{-1}, respectively, is the so called "Cl$^-$ interaction band" characteristic of stretching vibrations of C4–H (or C5–H) and C2–H interacting with the Cl$^-$ anion.[6,11,12] The dry [C$_4$MIM][BF$_4$] and [C$_6$MIM][BF$_4$] spectra (Figures 5.6a and 5.7a,

respectively) exhibit two well-resolved aromatic C–H stretching bands at 3164 cm^{-1} and 3118 cm^{-1} (Figure 5.6a) and at 3161 cm^{-1} and 3125 cm^{-1} (Figure 5.7a). These bands are attributed to hydrogen bonding between BF$_4$$^-$ and C4–H (or C5–H) and C2–H, respectively.[10,13]

Prominent imidazolium ring stretching modes are seen at 1569 cm^{-1} and 1172 cm^{-1} for [C$_4$MIM][Cl] (Figure 5.4a),[6] 1568 cm^{-1} and 1170 cm^{-1} for [C$_6$MIM][Cl] (Figure 5.5a),[6] 1572 cm^{-1} and 1170 cm^{-1} for [C$_4$MIM][BF$_4$] (Figure 5.6a),[11] and 1572 cm^{-1} and 1170 cm^{-1} for [C$_6$MIM][BF$_4$] (Figure 5.7a).[6] Stretching modes of the BF$_4$$^-$ anion are the broad peak centered at ~1049 cm^{-1} (Figure 5.6a) and ~1059 cm^{-1} (Figure 5.7a) and the sharp peaks around 1285 cm^{-1} and 753 cm^{-1} (Figure 5.6a) and 1285 cm^{-1} and 759 cm^{-1} (Figure 5.7a).[3]

Although imidazolium-based ILs containing longer-chained alkyl groups are less miscible with water compared to those containing shorter alkyl groups, these ILs still readily absorb moisture from the air. The extent of water adsorption was monitored using ATR-FTIR by exposure of [C$_4$MIM][Cl], [C$_6$MIM][Cl], [C$_4$MIM][BF$_4$], and [C$_6$MIM][BF$_4$] ILs to water vapor in the sealed ATR cell as a function of RH at 295 K. Figures 5.4b, 5.5b, 5.6b, and 5.7b show IR spectra of [C$_4$MIM][Cl], [C$_6$MIM][Cl], [C$_4$MIM][BF$_4$], and [C$_6$MIM][BF$_4$], respectively, deposited on a ZnSe ATR crystal after exposure to increasing RH. These spectra, after water adsorption onto the IL, were corrected by subtracting the background contribution from the dry IL from the absorbance spectra of the hydrated sample. Since the refractive index of an IL–H$_2$O mixture changes as a function of water content, there is an increase in the effective depth of penetration of the evanescent wave. In addition, the sample may spread differently in the ATR window due to the changes in the viscosity and surface tension of the IL–H$_2$O mixture. Because of these two effects, the intensities of all bands associated with the ILs increased in the presence

of water vapor. In addition, new prominent bands associated with water vibrations appeared in the spectrum.

The adsorption of water by [C$_4$MIM][Cl] produced a broad O–H peak centered at 3384 cm^{-1} at low RH (3% RH) that blue-shifts to 3399 cm^{-1} as the RH is increased up to 84% RH (Figure 5.4b), similar to that for bulk liquid water. Other prominent bands from water are recognized as the water bend at 1640 cm^{-1} and a broad band at ~2102 cm^{-1} assigned to a combination of the bending mode and a far-IR band associated with a librational mode of sterically hindered water molecules.[14] The intensity of these bands increased concomitantly with the increase in the RH of the added water vapor. In addition, the [C$_4$MIM]$^+$ ring bands at 1571 cm^{-1} and 1169 cm^{-1} are slightly blue-shifted and red-shifted, respectively. Blue-shifted aromatic C–H stretching bands also increase with increasing RH. The interaction of water vapor with [C$_6$MIM][Cl] produced results similar to [C$_4$MIM][Cl] with a broad O–H peak centered at ~3377 cm^{-1} at low RH (4% RH) that blue-shifts to 3392 cm^{-1} as the RH is increased to 84% RH (Figure 5.5b). Additionally, a water bend at 1638 cm^{-1} and a broad band at ~2112 cm^{-1} also appear as the RH is increased (Figure 5.5b). [C$_6$MIM]$^+$ ring bands at 1571 cm^{-1} and 1166 cm^{-1} (Figure 5.5b) are also slightly blue-shifted and red-shifted, respectively.

The interaction of water vapor with [C$_4$MIM][BF$_4$] (Figure 5.6b) at low RH (11% RH) produced a very different O–H region with peaks assigned as the ν_3 asymmetric stretch at 3638 cm^{-1} and the ν_1 symmetric stretch at 3561 cm^{-1} and from single water molecules hydrogen bonded by two BF$_4^-$ anions, as observed previously.[9,15-18] At low RH, the interaction of water vapor with [C$_6$MIM][BF$_4$] (Figure 5.7b) exhibited behavior similar to [C$_4$MIM][BF$_4$] with peaks in the O–H region assigned as the ν_3 asymmetric stretch at 3639 cm^{-1} and the ν_1 symmetric stretch at 3561 cm^{-1} (at 2% RH).[9,15-18]

As the RH increased to ~82% for [C$_4$MIM][BF$_4$] (Figure 5.6b), the intensity of the ν_3 symmetric and ν_1 asymmetric O–H stretches increased and shifted to ~3633 cm^{-1} and ~3564 cm^{-1}, respectively. At the same time there is growth of a liquid-like water peak at 3454 cm^{-1} and a shoulder at 3262 cm^{-1}, that dominates when water forms a well-ordered hydrogen bonding network as in ice. Other bands from water are recognized as the water bend at 1632 cm^{-1} and a broad band at ~2024 cm^{-1} is assigned to a combination of the bending mode and a far-IR band associated with a librational mode of sterically hindered water molecules.[14] Also evident, at higher RH (82% RH), is an increase of ring bands associated with the [C$_4$MIM]$^+$ cation at 1570 cm^{-1} and 1166 cm^{-1}. The increase in water content and the associated blue-shifts in the C–H stretches are indicative of water having an influence on the C–H interactions.[18]

Similar results were observed for [C$_6$MIM][BF$_4$] (Figure 5.7b). The intensity of the ν_3 symmetric and ν_1 asymmetric O–H stretches increased and shifted to ~3634 cm^{-1} and ~3563 cm^{-1}, respectively. The growth of a liquid-like water peak was observed at 3482 cm^{-1} and a shoulder at 3256 cm^{-1}. Additionally, a water bend at 1634 cm^{-1} and a broad band at ~2017 cm^{-1} also appeared as the RH was increased (Figure 5.7b). At higher RHs, ring bands associated with the [C$_6$MIM]$^+$ cation, at 1572 cm^{-1} and 1163 cm^{-1}, also increased.

To more systematically evaluate the effect of alkyl chain length on water uptake of the IL thin films as a function of RH, we calculated the ratio of the peak area of the O–H stretching region to that of the imidazolium aromatic ring stretch in the dry IL spectra for all six ILs (Figure 5.8). The ring stretch peak, centered at approximately 1572 cm^{-1} in all the dry IL spectra, was chosen because it is dominated by the motion of the C=C bonds of the imidazolium ring, which should not be strongly affected by the increase in the alkyl chain length or addition of water. Therefore, this normalization should provide a good metric for the relative amount of water

uptake for each of the ILs; a larger ratio value indicates that more water is taken up by the ILs. It should be noted that [C$_4$MIM][Cl] was omitted from Figure 5.8 because the low intensity of the dry IL spectrum resulted in unreliable O–H:aromatic peak area ratios compared to the remaining ILs.
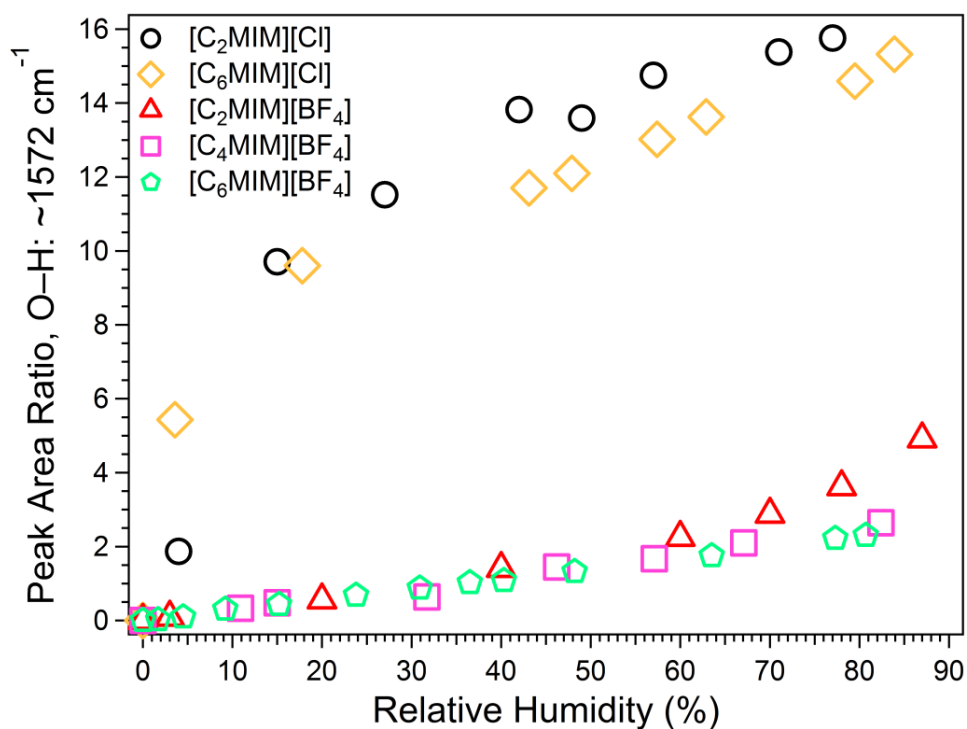
Figure 5.8. Peak area ratio of the O–H stretching region to the ~ 1572 cm^{-1} imidazolium ring stretch in the dry ionic liquid spectra as a function of RH. Re-analyzed ionic liquid ATR-FTIR data from our previous study,[1] [C$_2$MIM][Cl] (black circles) and [C$_2$MIM][BF$_4$] (red triangles), are included for comparison. Ionic liquids containing Cl$^-$ anions have larger O–H:aromatic peak areas compared to those containing BF$_4^-$ anions. As the alkyl chain length of the cation is increased, the O–H:aromatic peak area decreases. [C$_4$MIM][Cl] was omitted because of low absorbance in the dry ionic liquid spectrum.

The [C$_n$MIM][Cl] ILs have a considerably larger O–H:aromatic peak area ratio compared to the [C$_n$MIM][BF$_4$] ILs (Figure 5.8). Part of the increase may be due to higher O–H stretching band intensities in the Cl$^-$-based ILs, but the majority of the increase reflects higher hygroscopicity of [C$_n$MIM][Cl] ILs compared to [C$_n$MIM][BF$_4$] ILs. As the alkyl chain length of the cation decreases, the O–H:aromatic peak area ratio increases, a trend consistent with the hygroscopic growth measurements. We note that Jeon et al. performed ATR-FTIR measurements on various [C$_4$MIM][BF$_4$]–H$_2$O mixtures and plotted O–H vibrational peak areas versus molar water concentration of the solutions.[9] Unfortunately, we are unable to directly compare our results to theirs because our molar water concentrations are significantly smaller.

5.4.3. Equilibrium Molar Fractions of Water in Ionic Liquids

As described in Chapter 4, hygroscopic GFs of the IL nanoparticles can be converted quantitatively into the respective equilibrium molar fractions of water, $\chi_w = n_w/(n_w+n_{IL})$, in the IL–H$_2$O mixtures using eq 4.1. Equation 4.1 was derived based on the assumption that the nanoparticles are homogeneous spheres and have densities similar to the densities of the corresponding bulk IL–H$_2$O mixtures (a good assumption for particles this size). In Chapter 4, we compared χ_w data calculated from water uptake by both nanoparticles and IR thin films and found their χ_w values to be very similar, thus strengthening our argument that nanoparticles can serve as a model system for bulk measurements.

For [C$_4$MIM][Cl], [C$_6$MIM][Cl], and all three [C$_n$MIM][BF$_4$] (n = 2, 4, or 6) ILs, eq 4.1 was solved numerically for χ_w for every measured GF by using a fit of $\rho_{solution}$ data from Yang et al.,[19] Gomez et al.,[20] and Rilo et al.,[21] respectively, to an empirical dependence on χ_w. For example, χ_w of [C$_4$MIM][Cl], [C$_6$MIM][Cl], [C$_2$MIM][BF$_4$], [C$_4$MIM][BF$_4$], and [C$_6$MIM][BF$_4$]

nanoparticles at 83% RH was 0.878 ± 0.001, 0.848 ± 0.004, 0.725 ± 0.004, 0.569 ± 0.024, and 0.414 ± 0.049, respectively. For [C$_2$MIM][Cl], literature data for its physical properties are scarce. Therefore, in Chapter 4, we simplified eq 4.2 by assuming zero excess volume in the mixture (i.e., additive volumes) to achieve eq 4.2.

Both eqs 4.1 and 4.2 were used to calculate χ_w for [C$_4$MIM][Cl], [C$_6$MIM][Cl], and the [C$_n$MIM][BF$_4$] ILs. Equation 4.2 appears to be a reasonable alternative to the more accurate eq 4.1 for [C$_4$MIM][Cl], [C$_6$MIM][Cl], and the [C$_n$MIM][BF$_4$] ILs because it produces almost the same results. For example, at 83% RH $\chi_{w,ideal}$ for [C$_4$MIM][Cl], [C$_6$MIM][Cl], [C$_2$MIM][BF$_4$], [C$_4$MIM][BF$_4$], and [C$_6$MIM][BF$_4$] was 0.875 ± 0.002, 0.846 ± 0.004, 0.739 ± 0.004, 0.578 ± 0.024, and 0.428 ± 0.048, respectively; these values are very close to those cited in the previous paragraph. The [C$_n$MIM][Cl] IL–H$_2$O mixtures do not behave ideally – they exhibit significant negative deviations from Raoult's law over the entire RH range measured (Figure 5.9). However, the zero excess volume approximation (eq 4.2) appears to work well for such mixtures for the purposes of converting hygroscopic growth data into χ_w.

The dependence of χ_w (for [C$_4$MIM][Cl], [C$_6$MIM][Cl], and the [C$_n$MIM][BF$_4$] ILs) and $\chi_{w,ideal}$ (for [C$_2$MIM][Cl]) in the IL nanoparticles as a function of RH is shown in Figure 5.9. The dependence of $\chi_{w,ideal}$ in the IL nanoparticles as a function of RH for [C$_4$MIM][Cl], [C$_6$MIM][Cl], and the [C$_n$MIM][BF$_4$] ILs is shown in Figure 5.10. In order to discuss the dependence in terms of Raoult's law, RH values are purposely placed on the y-axis. Molar water fraction values were not corrected for the Kelvin effect (an increase in the equilibrium vapor pressure of water over the droplet relative to the vapor pressure of water over bulk solution) because the effect is small in nanoparticles of this size ($< 8\%$ for a ~ 27 nm water droplet). The Kelvin effect becomes even

smaller for IL–H₂O droplets because they have lower surface tension, which decreases when the

IL solution concentration or the alkyl chain length is increased.
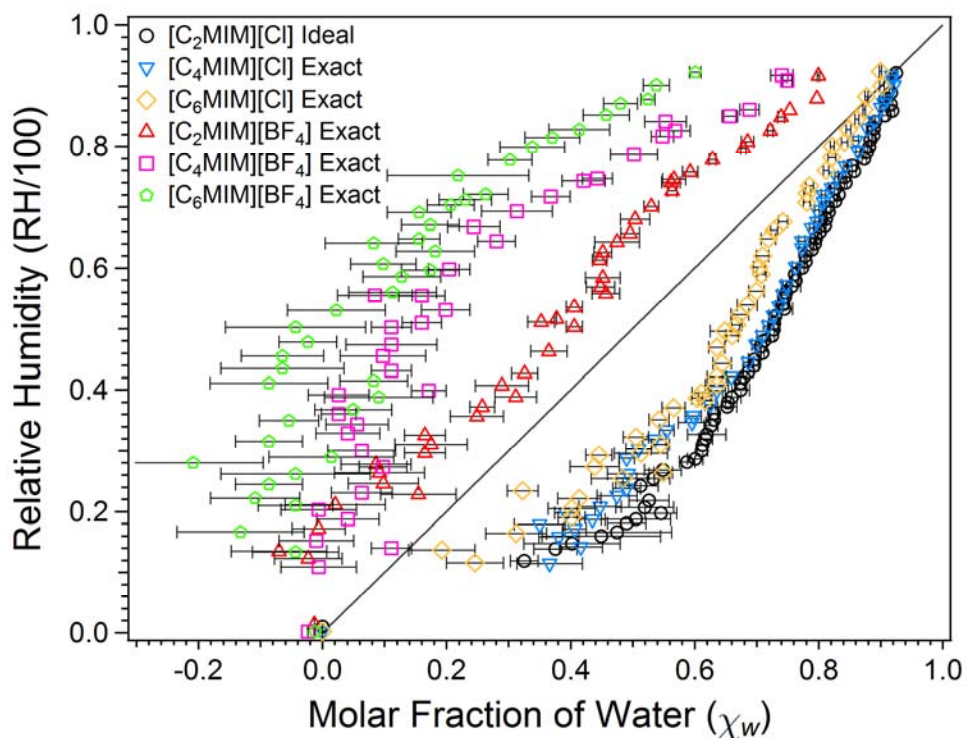
Figure 5.9. Water activity (RH/100) as a function of the molar fraction of water (χ_w) calculated from the GF values using eq 4.1 (actual densities) and eq 4.2 (ideal solution approximation). χ_w data from our previous study,[1] [C₂MIM][Cl] (black circles) and [C₂MIM][BF₄] (red triangles), are included for comparison. Raoult's law for an ideal solution is represented by the dark grey, solid line.
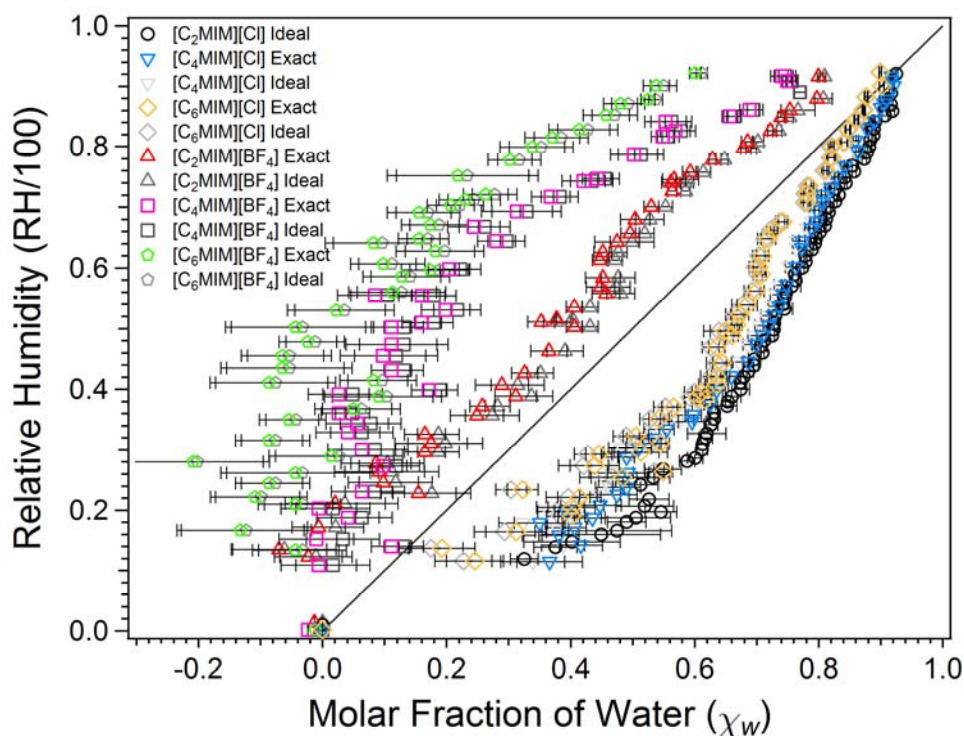
Figure 5.10. Water activity (RH/100) as a function of the molar fraction of water (χ_w), calculated from the growth factor values using eq 4.1 (actual densities) and eq 4.2 (ideal solution approximation). The χ_w data from our previous study,[1] [C$_2$MIM][Cl] (black circles) and [C$_2$MIM][BF$_4$] (red triangles), are included for comparison. Raoult's law for an ideal solution is represented by the dark grey, solid line.

Disregarding the Kelvin effect, the RH/100 values correspond to the equilibrium water activity in the IL–H$_2$O mixture.[1] The ILs containing the same anion (i.e., either Cl$^-$ or BF$_4^-$) exhibit qualitatively similar behavior in terms of deviations from Raoult's law. All [C$_n$MIM][BF$_4$] ILs exhibit positive deviations, with the magnitude of the deviation increasing as the alkyl chain length increases. The positive sign of the deviations suggests that the strength of the [C$_n$MIM][BF$_4$]–water interactions are weaker than the average of the strengths of the water–water and IL–IL interactions. Furthermore, as the length of the alkyl chain increases, the

120

disparity in the interactions grows. These observations are qualitatively consistent with the increased level of hydrophobicity of the $[C_n MIM]^+$ cation for larger n values. These weak interactions are also consistent with the narrow widths and small red-shifts of the O–H stretching bands in the ATR-FTIR spectra of these two ILs (shown in Figures 5.6 and 5.7 for $[C_4 MIM][BF_4]$ and $[C_6 MIM][BF_4]$, respectively).

$[C_n MIM][Cl]$–water mixtures all exhibit significant negative deviations from Raoult's law (Figure 5.9). Since the cation is the same as in the corresponding $[C_n MIM][BF_4]$ ILs, this suggest much stronger interaction between water and Cl^- versus water and BF_4^-. These results are consistent with strongly red-shifted and broad O–H stretching bands in the IR spectra of all $[C_n MIM][Cl]$–water mixtures examined here and in our previous study.[1] The negative deviations for $[C_2 MIM][Cl]$ are large, however, as the alkyl chain length increases up to hexyl $([C_6 MIM][Cl])$, the negative deviations are less significant, suggesting that the interaction strength between water and Cl^- decreases with increasing alkyl chain length.

Additionally, when comparing the $[C_n MIM][Cl]$ ILs and $[C_n MIM][BF_4]$ ILs in Figure 5.9, the alkyl chain length appears to matter more for $[C_n MIM][BF_4]$ than $[C_n MIM][Cl]$. We believe this is because the type of anion present in the IL has the dominant effect on water uptake and the χ_w present in the IL nanoparticles. The interaction strength between water and Cl^- is much larger than the interaction strength between water and BF_4^-, as shown in our previous MD simulations.[1] This larger interaction strength results in the differences between the χ_w values for the $[C_n MIM][Cl]$ ILs to be much smaller than the $[C_n MIM][BF_4]$ ILs. The larger differences in the χ_w values for $[C_n MIM][BF_4]$ are a direct indication that the type of cation present is only a secondary factor in regards to water uptake and the χ_w present in the IL nanoparticles.

It should be noted that, for eqs 4.1 and 4.2, we calculated χ_w by treating the IL as a single component, i.e., by defining χ_w as $n_w/(n_w+n_{IL})$. However, the cation and anion of the IL can alternatively be treated as separate particles, resulting in a different definition of the molar fraction of water, $\chi'_w = n_w/(n_w+2n_{IL})$. The two values of the molar fraction of water can be related to each other by means of the following equation (eq 5.1):

$$\chi'_w = \frac{\chi_w}{2 - \chi_w} \tag{5.1}$$

We re-plotted χ'_w as a function of RH for all six ILs in Figure 5.11. The plot looks qualitatively similar to Figure 5.9, however the [C$_n$MIM][Cl] ILs appear to better obey Raoult's law compared to the [C$_n$MIM][BF$_4$] ILs when χ'_w is used as the coordinate. This is consistent with the more inter-compatible interactions in the case where H$_2$O interacts with Cl$^-$ as opposed to BF$_4{}^-$.

We evaluated the performance of several correlative liquid activity coefficient models to fit the experimental data. In the case of ideal vapor-phase behavior, equating the fugacity of water in the liquid and vapor phase yields the following expression (eq 5.2):

$$\chi_w \cdot \gamma_w (\chi_w) = \frac{p_w}{p_w^{sat}} = \frac{RH}{100} \tag{5.2}$$

where p_w and p_w^{sat} are the partial pressure of water and the saturation vapor pressure of water, respectively. Non-ideal solution behavior is captured with the activity coefficient of water (γ_w).
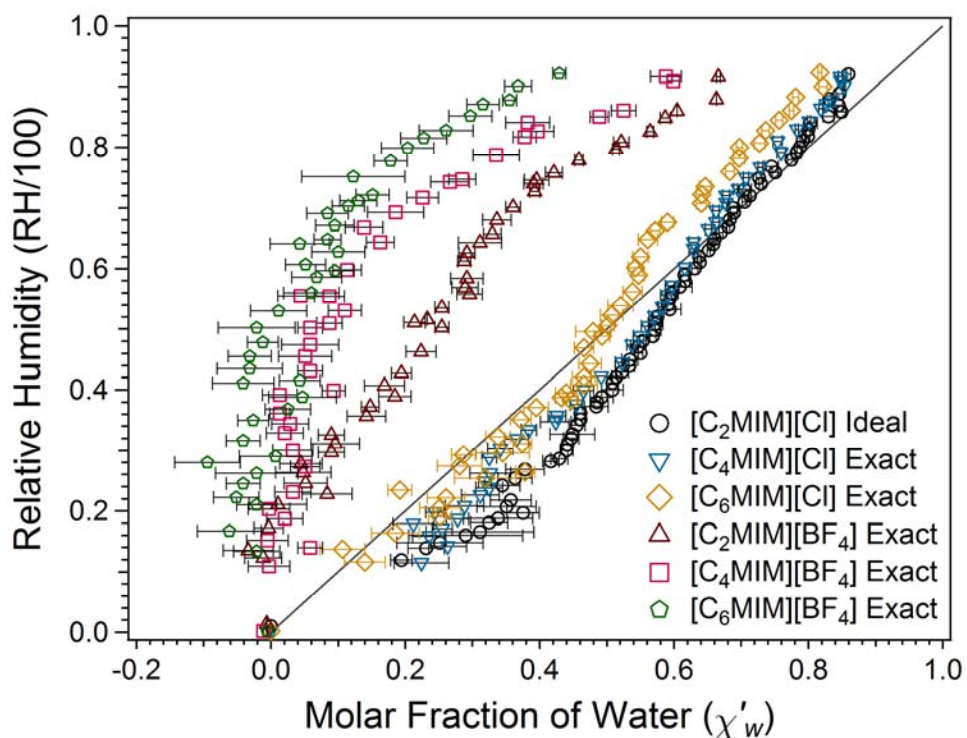
Figure 5.11. The water activity vs. molar faction of water (χ'_w) plot for the ionic liquids discussed in this study. The other plots of this type (Figures 5.9 and 5.10) used the molar fraction of water (χ_w) calculated by treating each ionic liquid molecule as a single entity. In this plot, the cation and anion of the ionic liquid were treated as separate particles, which effectively reduces the molar fraction of water. χ'_w can be straightforwardly calculated from χ_w as shown in the text (eq 5.1). Raoult's law for an ideal solution is represented by the dark grey, solid line.

We evaluated the following commonly-used one- and two-parameter correlative liquid activity coefficient models:[22] one-constant Margules equation (eq 5.3), two-constant Margules equation (eq 5.4), van Larr equation (eq 5.5), Wilson equation (eq 5.6), and the Flory-Huggins equation (eq 5.7).

$$\frac{RH}{100} = \chi_w \exp\left(\frac{A\chi_{IL}^2}{RT}\right) \tag{5.3}$$

$$\frac{RH}{100} = \chi_w \exp\left(\frac{\alpha\chi_{IL}^2 + \beta\chi_{IL}^3}{RT}\right) \tag{5.4}$$

$$\frac{RH}{100} = \chi_w \exp\left(\frac{\alpha}{\left[1 + \dfrac{\alpha}{\beta}\dfrac{\chi_w}{\chi_{IL}}\right]^2}\right) \tag{5.5}$$

$$\frac{RH}{100} = \chi_w \exp\left(-\ln\left(\chi_w + \Lambda_{12}\chi_{IL}\right) + \chi_{IL}\left[\frac{\Lambda_{12}}{\chi_w + \Lambda_{12}\chi_{IL}} - \frac{\Lambda_{21}}{\Lambda_{21}\chi_w + \chi_{IL}}\right]\right) \tag{5.6}$$

$$\frac{RH}{100} = \chi_w \exp\left(\ln\frac{\phi_w}{\chi_w} + \left(1 - \frac{1}{m}\right)\phi_{IL} + \chi_{Flory}\phi_{IL}^2\right) \tag{5.7}$$

For eq 5.7, χ_{Flory} is the Flory interaction parameter and is not related to the molar fraction of water values, $\phi_w = \dfrac{\chi_w}{\chi_w + m\chi_{IL}}$, $\phi_{IL} = \dfrac{m\chi_{IL}}{\chi_w + m\chi_{IL}}$, $m = \dfrac{v_{IL}}{v_w}$, v_w is molar volume of water, and v_{IL} is molar volume of IL. Fitting parameters, determined with non-linear least squares optimizations, are shown in Table 5.1. For clarity, only the fitting parameters for χ_w (eq 4.1) for [C$_4$MIM][Cl], [C$_6$MIM][Cl], and the [C$_n$MIM][BF$_4$] ILs and $\chi_{w,ideal}$ (eq 4.2) for [C$_2$MIM][Cl] are presented. Fitting parameters for χ_w and $\chi_{w,ideal}$ for all ILs can be found in Appendix A (Table A1). To use these fitting parameter in situations when the molar fraction of water is defined as $\chi'_w = n_w/(n_w + 2n_{IL})$, one must first calculate χ_w from χ'_w by reversing eq 5.1.
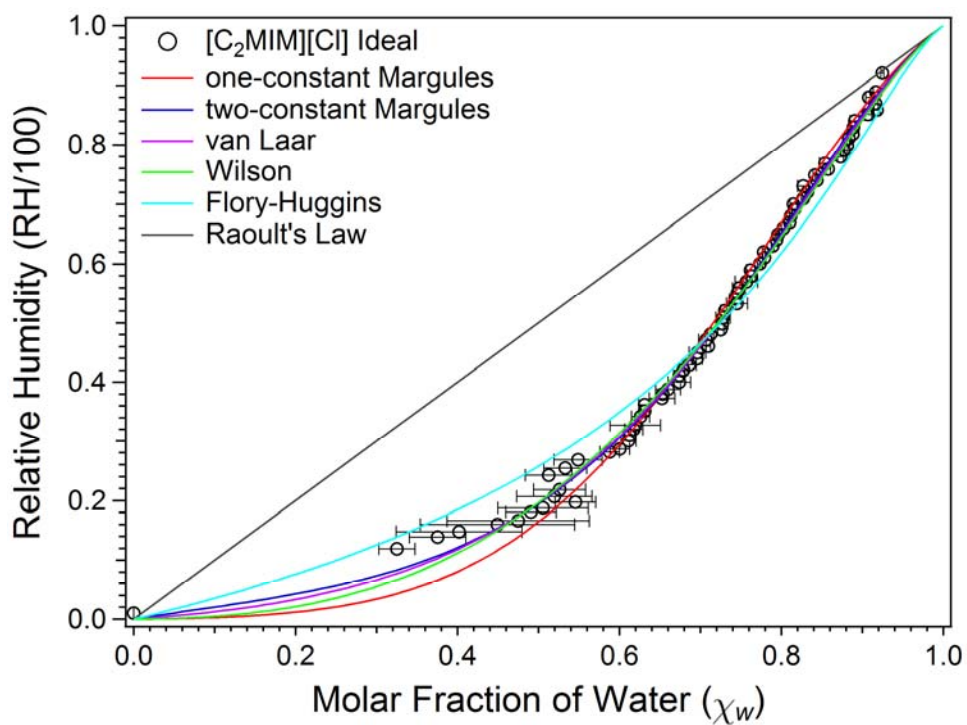
Table 5.1. Liquid Activity Coefficient Models Fitting Parameters

	one-constant Margules		two-constant Margules			van Laar			Wilson			Flory-Huggins	
	A/RT	R^2	α/RT	β/RT	R^2	α	β	R^2	Λ_{12}	Λ_{21}	R^2	φ_w	R^2
[C$_2$MIM][Cl] Ideal	−11035 ± 205	0.990	−14900 ± 376	11125 ± 976	0.996	−2.36 ± 0.12	−4.02 ± 0.05	0.995	4.17 ± 0.10	3.75 ± 0.75	0.994	0.00201 ± 0.01967	0.956
[C$_4$MIM][Cl] Exact	−7690 ± 310	0.982	−11944 ± 597	10256 ± 1264	0.992	−1.50 ± 0.11	−3.06 ± 0.08	0.992	3.87 ± 0.19	1.34 ± 0.23	0.991	0.299 ± 0.017	0.981
[C$_6$MIM][Cl] Exact	−5300 ± 269	0.970	−7354 ± 823	4720 ± 1741	0.971	−1.49 ± 0.28	−2.09 ± 0.10	0.971	2.67 ± 0.30	1.61 ± 0.50	0.968	0.601 ± 0.017	0.969
[C$_2$MIM][BF$_4$] Exact	2254 ± 172	0.907	3484 ± 790	−1891 ± 1190	0.922	0.528 ± 0.095	1.36 ± 0.26	0.934	1.31 ± 0.25	0.176 ± 0.094	0.934	1.27 ± 0.04	0.898
[C$_4$MIM][BF$_4$] Exact	4260 ± 175	0.823	4325 ± 1106	−81 ± 1357	0.824	1.71 ± 0.13	1.734 ± 0.18	0.825	0.314 ± 0.068	0.284 ± 0.084	0.834	1.68 ± 0.10	0.601
[C$_6$MIM][BF$_4$] Exact	5030 ± 279	0.624	4490 ± 2109	679 ± 2600	0.616	2.10 ± 0.25	1.94 ± 0.31	0.615	0.181 ± 0.088	0.220 ± 0.124	0.624	2.17 ± 0.11	0.360
Average R^2		0.882			0.887			0.889			0.891		0.794
R^2 of [C$_n$MIM][Cl]		0.980			0.987			0.986			0.984		0.969
R^2 of [C$_n$MIM][BF$_4$]		0.784			0.787			0.791			0.798		0.620

125

For the one-constant Margules equation, the fitting parameter "A" has a simple physical interpretation. Positive and negative values of "A" correspond to positive and negative excess free energy for a binary mixture, respectively. The positive deviation from Raoult's law for the BF_4^--containing ILs results in positive "A" values which increase in magnitude with the alkyl chain length, implying increasing deviations from the ideal behavior. The Cl^--containing ILs with negative deviations from Raoult's law have negative values of "A", but in contrast to the BF_4^--containing ILs, the magnitudes of "A" decrease with the alkyl chain length. Of the ILs examined in this work, $[C_2MIM][Cl]$ and $[C_6MIM][BF_4]$ deviate from ideality the most, in two opposing directions.

The performance of each activity coefficient model in representing the $[C_2MIM][Cl]$ data is presented in Figure 5.12. Similar plots detailing the other IL–H_2O systems we investigated are shown in Appendix A (Figures A1–A10). Overall, all models performed better when describing the behavior of $[C_nMIM][Cl]$ ILs compared to $[C_nMIM][BF_4]$ ILs. But, the two-constant Margules, van Larr, and Wilson models (all two-parameter equations) performed somewhat better than the one-parameter models when describing the behavior of both the $[C_nMIM][Cl]$ ILs and $[C_nMIM][BF_4]$ ILs. Accurately representing the ILs containing BF_4^- anions was considerably more difficult. The Flory-Huggins model, typically used to model polymer systems containing species of dissimilar sizes, requires the liquid molar volumes of the constituents. It then relies on a single fitting parameter to represent the data. The Flory-Huggins model has been used previously to describe a $[C_4MIM][PF_6]$ + water mixture[23] and a $[C_4MIM][BF_4]$ + water mixture.[24] However, with liquid molar volumes from MacMillan et al.[1] as inputs and an empirical fitting parameter designed to scale the enthalpic contribution to the excess Gibbs free energy, this model could not accurately reproduce systems with positive deviations from

Raoult's law. The Flory-Huggins' model performance was especially poor for the BF_4^--containing ILs (see Apendix A). Thermodynamic mixing behavior of the IL mixtures containing BF_4^- anions was best represented with the Wilson model. The van Larr and Margules models performed similarly.

Figure 5.12. One- and two-parameter correlative liquid activity coefficient models used to fit the equilibrium molar fractions of water (χ_w) calculated from the ionic liquid nanoparticle GF values. $\chi_{w,ideal}$ data for [C$_2$MIM][Cl] nanoparticles[1] (calculated using eq 4.2) are used here to represent the performance of each activity coefficient model. The two-parameter equations (i.e., two-constant Margules, van Larr, and Wilson models) performed better than the one-parameter equations (i.e., one-constant Margules and Flory-Huggins models). Raoult's law for an ideal solution is represented by the dark grey, solid line.

5.5. Conclusion

We have examined the effect of alkyl chain length on IL hygroscopicity for a subset of two families of ILs (i.e., $[C_nMIM][Cl]$ and $[C_nMIM][BF_4]$ ($n = 2$, 4, or 6)). Using the combined experimental techniques of TDMA hygroscopicity measurements and ATR-FTIR spectroscopy, the results show that all ILs containing Cl^- anions were more hygroscopic than those containing BF_4^- anions over the entire RH range and that uptake of water vapor decreases with increasing alkyl chain length on the $[C_nMIM]^+$ cation. The hygroscopicity of the ILs, in order of the most to least hygroscopic, are as follows: $[C_2MIM][Cl]$, $[C_4MIM][Cl]$, $[C_6MIM][Cl]$, $[C_2MIM][BF_4]$, $[C_4MIM][BF_4]$, and $[C_6MIM][BF_4]$. Overall, all liquid activity coefficient models performed better to describe the behavior of $[C_nMIM][Cl]$ ILs compared to $[C_nMIM][BF_4]$ ILs. The two-parameter models performed best in describing the behavior of both the $[C_nMIM][Cl]$ ILs and $[C_nMIM][BF_4]$ ILs.

References

(1) MacMillan, A. C.; McIntire, T. M.; Freites, J. A.; Tobias, D. J.; Nizkorodov, S. A. Interaction of Water Vapor with the Surfaces of Imidazolium-Based Ionic Liquid Nanoparticles and Thin Films. *J. Phys. Chem. B* **2012**, *116*, 11255-11265.

(2) Murgia, S.; Monduzzi, M.; Lopez, F.; Palazzo, G. Mesoscopic Structure in Mixtures of Water and 1-Butyl-3-Methyl Imidazolium Tetrafluoborate: A Multinuclear NMR Study. *J. Solution Chem.* **2013**, *42*, 1111-1122.

(3) Katsyuba, S. A.; Zvereva, E. E.; Vidis, A.; Dyson, P. J. Application of Density Functional Theory and Vibrational Spectroscopy Toward the Rational Design of Ionic Liquids. *J. Phys. Chem. A* **2007**, *111*, 352-370.

(4) Snyder, R. G.; Strauss, H. L.; Elliger, C. A. Carbon-Hydrogen Stretching Modes and the Structure of n-Alkyl Chains. 1. Long, Disordered Chains. *J. Phys. Chem.* **1982**, *86*, 5145-5150.

(5) MacPhail, R. A.; Strauss, H. L.; Snyder, R. G.; Elliger, C. A. Carbon-Hydrogen Stretching Modes and the Structure of n-Alkyl Chains. 2. Long, All-Trans Chains. *J. Phys. Chem.* **1984**, *88*, 334-341.

(6) Tait, S.; Osteryoung, R. A. Infrared Study of Ambient-Temperature Chloroaluminates as a Function of Melt Acidity. *Inorg. Chem.* **1984**, *23*, 4352-4360.

(7) Talaty, E. R.; Raja, S.; Storhaug, V. J.; Dölle, A.; Carper, W. R. Raman and Infrared Spectra and ab Initio Calculations of C2-4MIM Imidazolium Hexafluorophosphate Ionic Liquids. *J. Phys. Chem. B* **2004**, *108*, 13177-13184.

(8) Heimer, N. E.; Del Sesto, R. E.; Meng, Z.; Wilkes, J. S.; Carper, W. R. ibrational Spectra of Imidazolium Tetrafluoroborate Ionic Liquids. *J. Mol. Liq.* **2006**, *124*, 84-95.

(9) Jeon, Y.; Sung, J.; Kim, D.; Seo, C.; Cheong, H.; Ouchi, Y.; Wawa, R.; Hamaguchi, H. O. Structural Change of 1-Butyl-3-Methylimidazolium Tetrafluoroborate Plus Water Mixtures Studied by Infrared Vibrational Spectroscopy. *J. Phys. Chem. B* **2008**, *112*, 923-928.

(10) Jeon, Y.; Sung, J.; Seo, C.; Lim, H.; Cheong, H.; Kang, M.; Moon, B.; Ouchi, Y.; Kim, D. Structures of Ionic Liquids with Different Anions Studied by Infrared Vibration Spectroscopy. *J. Phys. Chem. B* **2008**, *112*, 4735-4740.

(11) Dieter, K. M.; Dymek, C. J.; Heimer, N. E.; Rovang, J. W.; Wilkes, J. S. Ionic Structure and Interactions in 1-Methyl-3-Ethylimidazolium Chloride-Aluminum Chloride Molten Salts. *J. Am. Chem. Soc.* **1988**, *110*, 2722-2726.

(12) Hitchcock, P. B.; Seddon, K. R.; Welton, T. Hydrogen-Bond Acceptor Abilities of Tetrachlorometalate(II) Complexes in Ionic Liquids. *J. Chem. Soc., Dalton Trans.* **1993**, 2639-2643.

(13) Katsyuba, S. A.; Dyson, P. J.; Vandyukova, E. E.; Chernova, A. V.; Vidiš, A. Molecular Structure, Vibrational Spectra, and Hydrogen Bonding of the Ionic Liquid 1-Ethyl-3-methyl-1H-imidazolium Tetrafluoroborate. *Helv. Chim. Acta* **2004**, *87*, 2556-2565.

(14) Gurnett, B.; Williams, D. Structure of Water and Aqueous Solutions. In *Proceedings of the International Symposium*; Luck, W. A. P., Ed.; Verlag Chemie/Physik Verlag: Weinheim, Germany, 1974; pp 206.

(15) Cammarata, L.; Kazarian, S. G.; Salter, P. A.; Welton, T. Molecular states of Water in Room Temperature Ionic Liquids. *Phys. Chem. Chem. Phys.* **2001**, *3*, 5192-5200.

(16) Fazio, B.; Triolo, A.; Di Marco, G. Local Organization of Water and its Effect on the Structural Heterogeneities in Room-Temperature Ionic Liquid/H$_2$O Mixtures. *J. Raman Spectrosc.* **2008**, *39*, 233-237.

(17) Takamuku, T.; Kyoshoin, Y.; Shimomura, T.; Kittaka, S.; Yamaguchi, T. Effect of Water on Structure of Hydrophilic Imidazolium-Based Ionic Liquid. *J. Phys. Chem. B* **2009**, *113*, 10817-10824.

(18) Zhang, L. Q.; Xu, Z.; Wang, Y.; Li, H. R. Prediction of the Solvation and Structural Properties of Ionic Liquids in Water by Two-Dimensional Correlation Spectroscopy. *J. Phys. Chem. B* **2008**, *112*, 6411-6419.

(19) Yang, Q. W.; Zhang, H.; Su, B. G.; Yang, Y. W.; Ren, Q. L.; Xing, H. B. Volumetric Properties of Binary Mixtures of 1-Butyl-3-methylimidazolium Chloride plus Water or Hydrophilic Solvents at Different Temperatures. *J. Chem. Eng. Data* **2010**, *55*, 1750-1754.

(20) Gómez, E.; Calvar, N.; Domínguez, I.; Domínguez, A. Physical Properties of the Ternary Mixture Ethanol + Water + 1-Hexyl-3-Methylimidazolium Chloride at 298.15 K. *Phys. Chem. Liq.* **2006**, *44*, 409-417.

(21) Rilo, E.; Pico, J.; Garcia-Garabal, S.; Varela, L. M.; Cabeza, O. Density and Surface Tension in Binary Mixtures of CnMIM-BF(4) Ionic Liquids with Water and Ethanol. *Fluid Phase Equilib.* **2009**, *285*, 83-89.

(22) Sandler, S. I. *Chemical and Engineering Thermodynamics*; John Wiley & Sons, Inc.: New York, 1999.

(23) Bendová, M.; Wagner, Z.; Moučka, M. Liquid-liquid Equilibrium in a Binary System 1-Butyl-3-Methylimidazolium Hexafluorophosphate + Water: Experiment and Data Correlation. *Int. J. Thermodyn.* **2008**, *11*, 109-114.

(24) Rebelo, L. P. N.; Najdanovic-Visak, V.; Visak, Z. P.; da Ponte, M. N.; Szydlowski, J.; Cerdeirina, C. A.; Troncoso, J.; Romani, L.; Esperanca, J.; Guedes, H. J. R.; de Sousa, H. C. A Detailed Thermodynamic Analysis of [C(4)mim][BF4] Plus Water as a Case Study to Model Ionic Liquid Aqueous Solutions. *Green Chem.* **2004**, *6*, 369-381.

Chapter 6: CO$_2$ Sequestration in Aerosolized Ionic Liquid Nanoparticles

6.1. Abstract

The emission of carbon dioxide (CO_2), a greenhouse gas, into the atmosphere has dramatically increased since the industrial age. This increase has helped to contribute to the warming of our planet. Sequestration of CO_2 in the environment using ionic liquids (ILs) is a potential long-term storage option for CO_2, with the goal of mitigating climate change. ILs may have the ability to uptake large amounts of CO_2 and can be used for CO_2 sequestration in the environment. Solutions of the IL 1-ethyl-3-methylimidazolium bis(trifluoromethylsulfonyl)-imide and ammonium sulfate (used as a control) were electrosprayed to produce dry nanoparticles. Aerosolized nanoparticles were exposed to 100% CO_2 and tandem nano-differential mobility analysis was used to study change in particle diameter before and after exposure to CO_2. The increase in growth factor after CO_2 exposure showed little change for both chemicals studied. The results suggest that CO_2 uptake does not lend to significant molar volume change for this IL.

6.2. Introduction

As discussed in Chapter 1, ionic liquids (ILs) have a bright future in Green Chemistry and Environmental Sustainability.[1] Popular for their unique physical and chemical properties, they are finding increased use in environmentally friendly applications.[1] The solubility of various gases in ILs is of particular interest.[2–8] A significant amount of research is currently being conducted to study the solubility and selectivity of gasses, such as carbon dioxide (CO_2), in ILs,[2–8] Imidazolium-based IL cations have been found to be especially soluble for CO_2.[2,3,6] Though, when comparing the cation-anion pair, studies suggest the anion has more influence on gas solubility.[2–5]

ILs may have the ability to absorb large amounts of CO_2 and can be used for CO_2 sequestration in the environment. The emission of CO_2, a greenhouse gas, into the atmosphere has dramatically increased since the industrial age. This increase has helped to contribute to the warming of our planet. Sequestration of CO_2 in the environment using ILs is a potential long-term storage option for CO_2, with the goal of mitigating climate change.

The pure IL nanoparticles were size-selected using tandem nano-differential mobility analysis (TDMA), exposed to 100% CO_2, and their size distributions after CO_2 exposure were measured. The IL CO_2 growth factor (GF), the ratio of the 100% CO_2 to 0% CO_2 particle diameters (eq 1.1), was calculated and compared to the GF of a control nanoparticle that was also exposed to CO_2. In this study, ammonium sulfate ((NH_4)$_2SO_4$) was used as the control because it forms spherical particles upon atomization and is not expected to take up any CO_2. The following sections discuss the results from the preliminary study and outline the Future Work for this project.

6.3. Experimental

The experimental conditions including the chemicals used, solution preparation, nanoparticle generation, CO_2 uptake measurements can be found in Chapter 2. Specifically, chemicals used can be found in Section 2.2.2. Solution preparation and nanoparticle generation can be found in Section 2.6.2. CO_2 uptake measurements can be found in Section 2.8.

6.4. Results and Discussion

The measured size-selected particle distributions, before and after exposure to 100% CO_2, for [C$_2$MIM][Tf$_2$N] and $(NH_4)_2SO_4$ nanoparticles with initial mobility-equivalent diameters ($d_{m,initial}$) centered at ~ 31 nm are shown in Figure 6.1. The individual size-selected particle distributions (exposed to 0 or 100% CO_2) are an average of ~ 7 experimental runs. The nanoparticles were exposed to CO_2 for a period of a few seconds in the experiments. The initial mobility-equivalent diameter of ~ 31 nm was chosen because it was near the peak of the full size-distribution for the [C$_2$MIM][Tf$_2$N] IL nanoparticles generated by the electrospray aerosol generator, thus maximizing the particle concentration. The same initial particle diameter of ~ 31 nm was chosen for the control ($(NH_4)_2SO_4$).
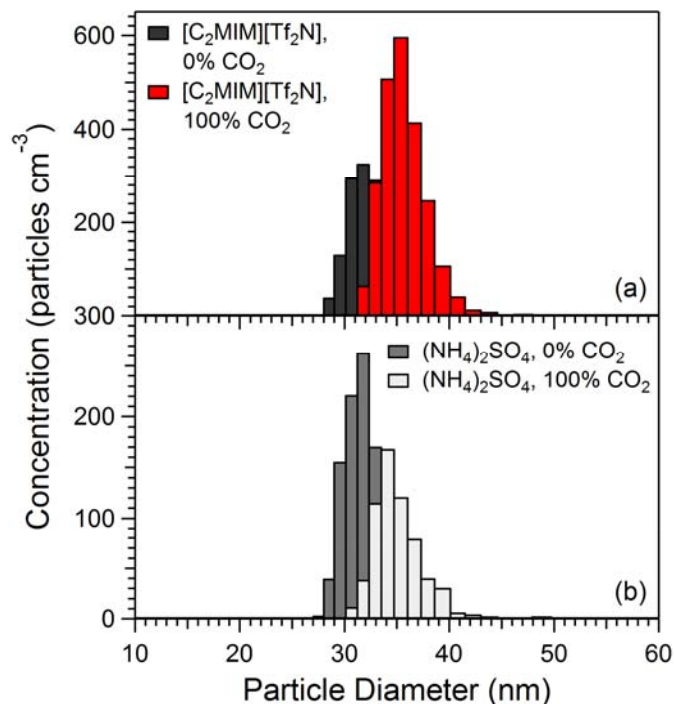
Figure 6.1. Size-selected particle distributions for $[C_2MIM][Tf_2N]$ (a) and $(NH_4)_2SO_4$ (b) exposed to 0 and 100% CO_2 at STP. There was no significant difference between the two samples.

Qualitatively examining Figure 6.1 shows that the 100% CO_2 size-distributions measured for $[C_2MIM][Tf_2N]$ and $(NH_4)_2SO_4$ are centered around the same particle diameter. $(NH_4)_2SO_4$ is not known to take up CO_2 so there should not be any increase in its particle diameter after exposure to 100% CO_2. The apparent increase is an artifact of the SMPS measurement. SMPS measures the mobility-equivalent particle diameter and relies on the Einstein–Smoluchowski relation to convert the measured mobility in particle size. The mobility (Z) of particle with radius (r) and charge (q) is proportional to the particle diffusion coefficient (D), which is related to the gas viscosity (η):

$$Z = \frac{qD}{kT} = \frac{q}{6\pi\eta r}$$

since the mobility of particles depends on the viscosity of the medium, and viscosity is different

for air without CO_2 (1.82×10^{-5} Pa s at 20 °C) and 100% CO_2 (1.47×10^{-5} Pa s 20 °C). In the

experiment, the particle is first mobility-size-selected in air by nano-DMA1 and then sized in

100% CO_2 by nano-DMA2. The software that inverts the nano-DMA2 measurements assumes

that the particles were mobility-separated in air, and therefore it reports an apparent radius that is

higher than the actual radius:

$$\eta_{air} r_{DMA1} = \eta_{CO_2} r_{DMA2} \quad \text{or} \quad \frac{r_{DMA2}}{r_{DMA1}} = \frac{\eta_{air}}{\eta_{CO_2}} = 1.24$$

Therefore, in our measurements we have to take the measured GF for $(NH_4)_2SO_4$ as a base

measurement. If the IL experiences any CO_2 uptake that increases its particle size, the apparent

GF should be higher than the apparent GF for $(NH_4)_2SO_4$. The slightly more right-shifted 100%

particle distribution for [C$_2$MIM][Tf$_2$N] indicates that those IL nanoparticles did take up a very

small amount of CO_2 compared to the $(NH_4)_2SO_4$ control, but the effect appears to be small.

To more quantitatively determine the amount of CO_2 taken up by the nanoparticles, the

GF was calculated using eq 1.1. Table 6.1 shows the $d_{m,initial}$, $d_{m,CO2}(100\%)$ (i.e., the mobility-

equivalent diameter of particles in equilibrium with 100% CO_2), and calculated GFs for

[C$_2$MIM][Tf$_2$N] and $(NH_4)_2SO_4$ nanoparticles.

Table 6.1. The measured mean mobility-equivalent particle diameters at 0 and 100% CO_2 and calculated GFs for [C$_2$MIM][Tf$_2$N] and (NH$_4$)$_2$SO$_4$ nanoparticles

Nanoparticles	$d_{m,initial}$ *(nm)*	$d_{m,CO2}$*(100%) (nm)*	GF
[C$_2$MIM][Tf$_2$N] (IL)	31.1 ± 0.1	34.8 ± 0.2	1.12 ± 0.01
(NH$_4$)$_2$SO$_4$ (control)	30.9 ± 0.2	34.2 ± 0.3	1.10 ± 0.01

The small GF calculated for (NH$_4$)$_2$SO$_4$ nanoparticle (1.10 ± 0.01) is different from the expected value of 1.24, likely because of miscalibration of nano-DMA2 with respect to DMA1. However, what is important is the relative values of GFs for (NH$_4$)$_2$SO$_4$ and [C$_2$MIM][Tf$_2$N]. The GF for [C$_2$MIM][Tf$_2$N] falls within error of the control's GF, showing that the [C$_2$MIM][Tf$_2$N] IL nanoparticles used in this preliminary study either did not take up any appreciable amount of CO_2 or the uptake of CO_2 did not produce any change in the particle volume.[2,3] While no change in the GF can still be considered a result, it is not as useful as we hoped to observe. Our initial intention was to measure the GF over a range of CO_2 concentrations in air, but since even the highest concentration of CO_2 produced no growth, measurements at lower CO_2 concentrations were not attempted. Fortunately, this work is only a preliminary study in our lab of CO_2 uptake by IL nanoparticles. There are several modifications that can be made to this study (including studying other ILs, experimental set-up modifications, etc.). These modifications will be discussed in detail in the Future Work section (Section 6.6) below.

6.5. Conclusion

In this study, we have examined the ability of $[C_2MIM][Tf_2N]$ IL nanoparticles to uptake CO_2 in an effort to explore the potential for $[C_2MIM][Tf_2N]$ IL nanoparticles to be a viable technology for CO_2 sequestration in the environment. By measuring the nanoparticles using method of TDMA and calculating the particles GF (the ratio of the particle diameters before and after exposure to 100% CO_2), we were able to determine how much the particles grow in size after exposure to 100% CO_2. After exposure to 100% CO_2, the $[C_2MIM][Tf_2N]$ IL nanoparticles experienced an apparent GF of 1.12 ± 0.01, which did not differ from the apparent GF of $(NH_4)_2SO_4$ nanoparticles (chosen because the compound is not known to uptake CO_2 at ambient temperature and pressure). Therefore it could be concluded that this IL either does not absorb CO_2 or does not change its molar volume upon CO_2 absorption. However, this is only a preliminary study of CO_2 sequestration of IL nanoparticles at ambient temperature and pressure. There are several modifications that can be made to optimize the study; which are described below.

6.6. Future Work

While the preliminary results for CO_2 uptake by IL nanoparticles are disappointing, this project is still very promising. The good news is that only one IL ($[C_2MIM][Tf_2N]$) has been studied, thus far. There are hundreds of different types of ILs that exist. Several have already been tested and found to have varying degrees of CO_2 solubility.[2–8] There are also many where CO_2 solubility has yet to be studied.

Additionally, Future Work should examine the length of exposure time to CO_2. The current TDMA set-up has the nanoparticles exposed to CO_2 for only a few seconds and might be

too short for the IL nanoparticles to reach equilibrium with CO_2. Longer exposure to CO_2 (e.g., 60 s or longer) might allow for equilibrium to be achieved and increase the amount that IL nanoparticles take up. Several size-selected particle diameters should also be examined to determine if there is any correlation between particle size and CO_2 uptake. Finally, if all goes well, the experimental set-up can be modified to study CO_2 at fixed levels other than 100% CO_2. The change in GF as a function of % CO_2 level can be plotted, generating a Growth Curve, which then can be converted into equilibrium amount of CO_2 taken up by IL, as we did for water in Chapters 4 and 5.

References

(1) *Ionic Liquids in Synthesis*; 2nd ed.; Wasserscheid, P.; Welton, T., Eds.; Wiley-VCH: Weinheim, Germany, 2008; Vol. 1.

(2) Anthony, J. L.; Anderson, J. L.; Maginn, E. J.; Brennecke, J. F. Anion Effects on Gas Solubility in Ionic Liquids. *J. Phys. Chem. B* **2005**, *109*, 6366-6374.

(3) Anthony, J. L.; Maginn, E. J.; Brennecke, J. F. Solubilities and Thermodynamic Properties of Gases in the Ionic Liquid 1-n-Butyl-3-Methylimidazolium Hexafluorophosphate. *J. Phys. Chem. B* **2002**, *106*, 7315-7320.

(4) Cadena, C.; Anthony, J. L.; Shah, J. K.; Morrow, T. I.; Brennecke, J. F.; Maginn, E. J. Why Is CO_2 So Soluble in Imidazolium-Based Ionic Liquids? *J. Am. Chem. Soc.* **2004**, *126*, 5300-5308.

(5) Blanchard, L. A.; Hancu, D.; Beckman, E. J.; Brennecke, J. F. Green Processing using Ionic Liquids and CO_2. *Nature* **1999**, *399*, 28-29.

(6) Chen, Y.; Mutelet, F.; Jaubert, J.-N. Solubility of Carbon Dioxide, Nitrous Oxide and Methane in Ionic Liquids at Pressures Close to Atmospheric. *Fluid Phase Equilib.* **2014**, *372*, 26-33.

(7) Finotello, A.; Bara, J. E.; Camper, D.; Noble, R. D. Room-Temperature Ionic Liquids: Temperature Dependence of Gas Solubility Selectivity. *Ind. Eng. Chem. Res.* **2008**, *47*, 3453-3459.

(8) Brennecke, J. F.; Maginn, E. J. Ionic liquids: Innovative Fluids for Chemical Processing. *Aiche J.* **2001**, *47*, 2384-2389.

Chapter 7: Ionic Liquids as Suitable Seed Particles for Secondary Organic

Aerosol Formation and Growth

7.1. Abstract

The use of seed particles to facilitate the formation and growth of secondary organic aerosol (SOA) is a common practice in studying aerosol chamber experiments. Traditionally, seed particles are solid, inorganic salts that volatile organic compound (VOC) photooxidation products can condense onto and form SOA. However, liquid seed particles may be better for SOA formation because they promote partitioning of organic compounds into the particle phase. Seed particles should be as unreactive as possible with the VOC oxidation products, and only act as an efficient solvent towards them. Ionic liquids (ILs) could represent a suitable choice for use as a seed particle for SOA because of the unique ability of ILs to act as a universal solvent for organic compounds. In this study, several types of ILs were investigated as suitable seed particles for SOA formation from ozonolysis of α-pinene. IL solutions were atomized and size-selected using a scanning mobility particle sizer (SMPS) spectrometer. Particles were injected into a 5 m^3 environmental smog chamber. SOA formation and particle evolution was monitored with a second SMPS and a high resolution time of flight aerosol mass spectrometer. IL seed particles for SOA formation were compared to a more traditional seed particle (polyethylene glycol). The results show promise in using ILs as aerosol seed particles, although further experiments are needed to optimize the conditions.

144

7.2. Introduction

Formation and composition of secondary organic aerosol (SOA) in the atmosphere is complex and still poorly understood. To better understand these processes, SOA can be generated in an environmental smog chamber. The desired organic precursors (e.g., α-pinene, limonene, isoprene) and oxidants (e.g., O_3, NOx, OH) are added and reacted together to generate SOA, which can then be analyzed using a variety of methods. Seeding is the technique of using a starting aerosol seed particle for the organic precursor(s).[1] Seed particles act as nuclei for SOA formation to help overcome the Kelvin barrier associated with homogeneous nucleation.[2] The seed particles are introduced into the chamber before the other SOA precursors are added. In some experiments, it is advantageous for the seed particles to have the same size; in this case, the seed particles are size-selected before injecting them in the chamber.

Chemicals best suited for use as seed particles are those with similar properties to the organic precursor(s) (e.g., phase state and pH) because it allows for the greatest amount of interaction to occur between the seed and precursor(s).[1] While not abundant in the atmosphere, ionic liquids (ILs) have physiochemical properties that make them very promising for use as seed particles. As discussed in Chapter 1, they have negligible vapor pressures, are liquid at room temperature, and dissolve a wide range of organic compounds.[3,4] Because of this, it is believed that they would react less with the VOC photooxidation products compared to previous seeds studied, while at the same time promoting partition of these products in the particle phase because of their high solubility in ILs. Use of ILs in various applications continues to increase rapidly. If successful, this project might allow for ILs to be used in an even wider range of applications than those mentioned in Chapter 1.

The ILs studied as suitable seed particles for SOA growth and formation were 1-hexyl-3-methylimidazolium ($[C_6MIM][BF_4]$), 1-ethyl-3-methylimidazolium bis(trifluoromethylsulfonyl)-imide ($[C_2MIM][Tf_2N]$), and 1-ethyl-3-methylimidazolium dicyanamide ($[C_2MIM][dca]$). These ILs were chosen because they are all liquid at room temperature and were readily available in our laboratory. (Poly)ethylene glycol (PEG) was used as the control seed particle. Ozone (O_3) was used as the oxidant; it is not expected to be reactive with respect to ILs or PEG.

7.3. Experimental

The experimental conditions including the chemicals used, solution preparation, seed particle atomization, and SOA formation and growth can be found in Chapter 2. Specifically, chemicals used can be found in Section 2.2.2. Solution preparation for atomization can be found in Section 2.9.1. IL seed particle atomization can be found in Section 2.6.2. SOA formation and growth with IL seed particles in the **small** and **large** smog chambers can be found in section 2.9.3.

7.4. Results and Discussion

The overarching goal of this project was to study the suitability of size-selected ILs as seed particles for SOA formation and growth. To achieve this, several parameters were tested to optimize the study. For the Results and Discussion section, only the more and mostly successful attempts are included here. The less successful attempts, along with how to improve them, will be discussed in the Future Work section below.

The initial studies were done without size-selection of IL seed particles, to ensure our seed material does not react with O_3 and α-pinene. Three ILs and the control (PEG) were

146

atomized and studied as suitable seed particles for oxidation of α-pinene with O_3. Figure 7.1

shows the total particle mass concentrations as a function of time, measured by the SMPS,

throughout the duration of the large chamber experiments. The initial solution concentrations,

dissolved in MeOH, used to generate the seed particles were ~ 1 g L^{-1} (Table 7.1). The seed

particles and 600 ppb O_3 were individually introduced into the chamber and allowed to

equilibrate for a total of 2 h. After addition of O_3, the IL seeds and O_3 were mixed for 1 h to

determine if O_3 and the ILs reacted with each other, as indicated by a sharp increase in particle

number concentration (Figure 7.1). Waiting 1 h after addition of O_3 was not done for PEG

because PEG does not react with O_3 and is also a liquid at room temperature (Figures 7.1). After

mixing, 2 μL of α-pinene were evaporated into the large chamber (mass concentration of ~ 400

μg m^{-3}) to the large chamber. The reactions were then allowed to proceed for ~ 3 h.

The seed particles had similar starting mass concentrations before addition of O_3 or α-

pinene (Figure 7.1a). The sharp increases in slope seen in Figure 7.1a, starting around SMPS

sample run number 18 for PEG and 35 and later for the three IL seed particle experiments,

indicates when α-pinene was added and SOA started to form. Compared to the control (PEG),

the three IL seed particle experiments all have substantially larger increases in SOA particle

mass concentration after the organic precursor, α-pinene, was added. After 3 h of ozonolysis, the

final SOA mass concentration using PEG seed particles was only 170 μg m^{-3} (Table 7.1); a 20%

increase compared to PEGs' initial seed particle mass concentration.

147
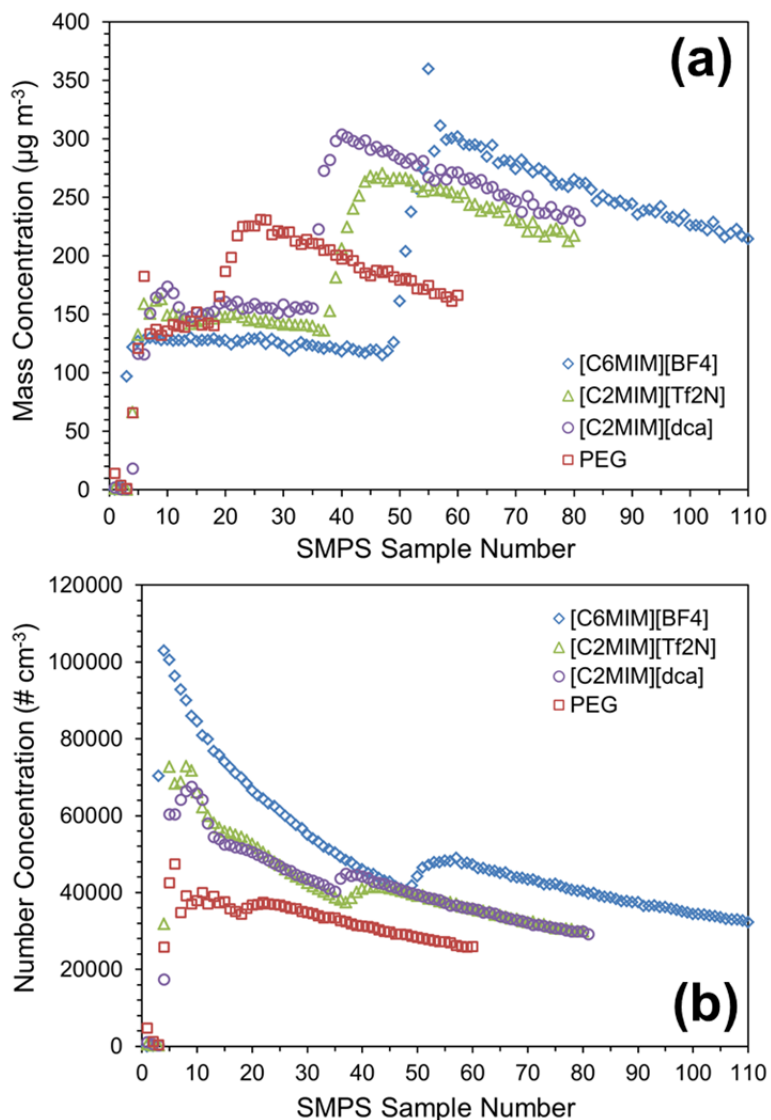
Figure 7.1 Particle mass (a) and number (b) concentration as a function of time in the large smog chamber for the seed particles studied. Overall, there were no drastic increases in mass of number concentration when SOA was forming for any of the four experiments. The small increase in particle number concentration (b) seen around 18 for PEG and 35–50 for the ionic liquid seeds indicates when the α-pinene was added to the large chamber. For these experiments, too much α-pinene was added; something that will be addressed in future experiments.

The final SOA mass concentrations after 3 h of ozonolysis using [C$_6$MIM][BF$_4$], [C$_2$MIM][Tf$_2$N], and [C$_2$MIM][dca] IL seed particles were 220, 220, and 230 µg m^{-3}, corresponding to an increase in mass concentration from α-pinene ozonolysis of ~ 69, 47, and 53%, respectively (Table 7.1).

Table 7.1. Seed solution concentrations for atomized seed particles that were not size-selected and particle diameters and mass concentration before addition of 2 µL α-pinene and after 3 h of α-pinene ozonolysis in the large smog chamber

Seed Particle	Solution Conc. (g L^{-1})	Particle Diameter (nm)		Particle Mass Conc. (µg m^{-3})	
		Seed†	SOA‡	Seed†	SOA‡
[C$_6$MIM][BF$_4$]	1.1	110	120	120	170
[C$_2$MIM][Tf$_2$N]	1.2	120	140	140	170
[C$_2$MIM][dca]	1.3	120	150	150	170
PEG	1.0	120	140	140	150

† Seed particle size and/or mass concentration in the large chamber before α-pinene was added.
‡ SOA particle size and/or mass concentration in the large chamber after ~ 3 h ozonolysis of α-pinene.

When working with seed particles, an increase in particle mass concentration after addition of the organic precursor indicates that the organic precursor is using the seed particles as nuclei for SOA formation, as intended. However, for particle number concentration, there should be a slight decrease as a function of time (indicative of particle conglomeration and wall loss) after the precursors are added, and no effect of α-pinene addition on the if the products of α-pinene oxidation exclusively condense on seed particles and do not participate in competing homogeneous condensation. We did observe an increase in the particle number concentration suggesting that homogeneous condensation occurred to some extent (Figure 7.1b). We note that comparison between different experiments is complicated because of the different initial size

distribution of seed particles. While the mass concentrations of the seeds before addition of α-pinene were roughly the same (Figure 7.1a), the number concentrations for all four seeds studied varied widely (Figure 7.1b).

Figure 7.2 shows the geometric mean particle number size as a function of time for the seed particles. Upon addition of α-pinene, the average particle size increased and stabilized at a new level consistent with the expectation that α-pinene oxidation products were condensing on the seed particles. The increase in the particle size is systematically larger for the three ILs tested in this study compared to PEG suggesting that ILs represent better seed materials for particle formation.
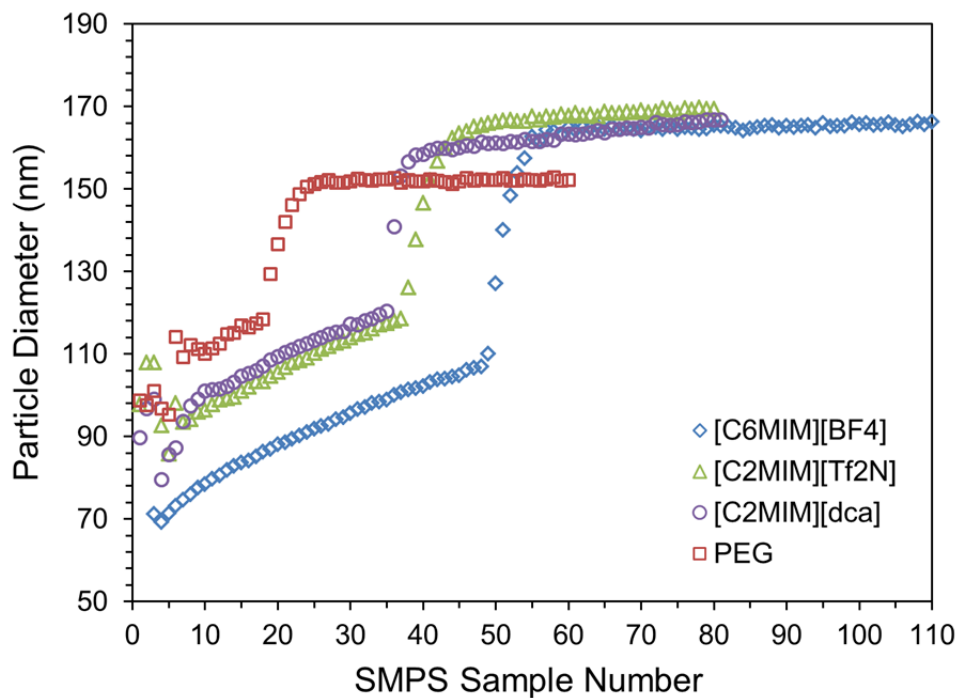
Figure 7.2. Geometric mean particle number size as a function of time in the large smog chamber for the seed particles studied. The three ionic liquids all had larger increases in particle diameter after the addition of α-pinene compared to PEG.

Figure 7.3 illustrates the evolution of the particle number concentrations and particle diameter as a function of time. When studying nucleation events in ambient air these types of three-dimensional plots are commonly used to observe the number concentration and particle diameter as a function of time.[5,6] As seen in Figure 7.3, the large number concentration of particles at the start of the experiment is due to introduction of the seed particles into the chamber. The seed particles are then allowed to stabilize in the chamber before the addition of O_3 and α-pinene. While the particles are stabilizing they slowly coagulate, thus decreasing their number concentration and increasing their particle size (Figure 7.3). All four seeds studied stated out with ~ 100 nm diameter particles, though number concentrations varied (Figures 7.1 and 7.2). Once α-pinene was added (as seen by the sharp jump in particle diameter on the plots in Figure 7.3) and SOA particles started to form, the three IL seed particle experiments all had larger increases in particle diameter (~ 170 nm) compared to PEG (~ 150 nm).

6.6. Conclusion

The overall goal of this project was to study the utility of ILs are used as seed particles for SOA formation and growth. For this preliminary study, we have investigated the use of ILs as seed particles for SOA formation and growth from oxidation of α-pinene in an environmental smog chamber. For the studies where aerosolized seeds were not size-selected before introduced into the chamber, the ILs all had larger increases in mass concentration from SOA formation compared to PEG. The IL seed studies also all had larger increases in particle diameter after the addition of α-pinene compared to PEG. The desired goal of this project is to size-select the seed particles, however, much work remains to accomplish this. The Future Work section above outlines the major areas that need to be addressed to make this study successful.
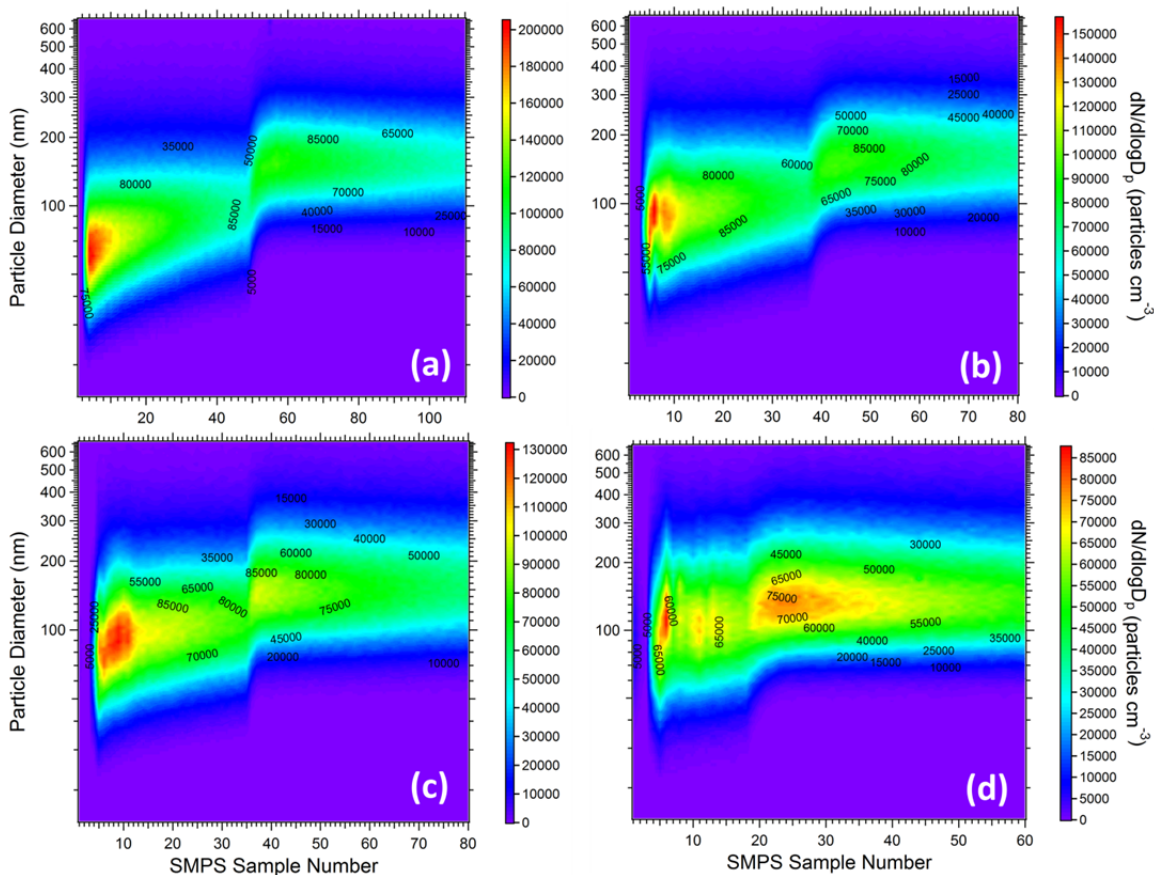
Figure 7.3. Aerosol number concentration as a function of time and particle diameter for SOA particle formation and growth from ozonolysis of α-pinene and various seed particle nuclei. After addition of α-pinene, the SOA particle evolutions using [C$_6$MIM][BF$_4$] (a), [C$_2$MIM][Tf$_2$N] (b), and [C$_2$MIM][dca] (c) as ionic liquid seed nuclei have larger SOA mass concentrations compared to PEG (d). The sharp increase in slope, starting around sample run number 20 for PEG and 35–50 for the three ionic liquid seed nuclei experiments, shown on all four plots indicates when α-pinene was added and SOA started to form.

6.5. Future Work

It was relatively straightforward to conduct the experiments for SOA formation and

growth with seed particles that were not size-selected. The process of testing parameters (i.e.,

solution concentration, atomizer run time, flow rates, etc.) to generate seed particles in the small

smog chamber and extrapolating those results to the large smog chamber were fairly straightforward and accurate. This was not the case for the size-selected studies. Several IL solutions at varying solution concentrations with different initial particle diameters were studied.

Several, mostly unsuccessful, attempts at size-selecting the seed particles were made. Those experiments are discussed below as well as why the majority of them were unsuccessful (i.e., seed particle mass concentrations in the chamber were too low to inject α-pinene to generate SOA). Extrapolating the results from the small to large chamber was, overall, not successful. The following section highlights some of the attempts made at optimizing the study and includes suggestions for improvement.

Twelve attempts at size-selecting seed particles in the large chamber have been conducted. All 12 size-selection experiments examined various types of seeds, solution concentrations, and selected seed sizes. Selected sizes were chosen based on the mean size of the seed particles' measured full distribution. Out of those 12, only four had O_3 and α-pinene added. Their experimental parameters are shown in Table 7.2. Furthermore, only two of those four had seed particle mass concentrations, before addition of O_3 and α-pinene, higher than 100 $\mu g\ m^{-3}$ (90 $\mu g\ m^{-3}$ for the 10.2 g L^{-1} [C_6MIM][BF_4] and 115 $\mu g\ m^{-3}$ for the 50.1 g L^{-1} [C_2MIM][Tf_2N]). As mentioned in Chapter 2, the initial seed particle mass concentration goal for the size-selected experiments was 100–150 $\mu g\ m^{-3}$. The other two experiments where O_3 and α-pinene were added had starting seed particle mass concentrations in the large chamber that did not exceed 10 $\mu g\ m^{-3}$ (Table 7.2). The 1.1 g L^{-1} [C_6MIM][BF_4] solution experiment selecting for 100 nm particles (Table 7.2) most likely had a low SOA mass concentration because the starting solution concentration was too low. The 1.1 g L^{-1} [C_6MIM][BF_4] solution experiment selecting for 10 nm particles (Table 7.2) had a low SOA mass concentration because the

atomizer became pressurized and caused the solution bottle to leak out. Final SOA mass

concentrations for the four experiments where α-pinene and O_3 were added are also listed in

Table 7.2. The final SOA mass concentrations are highly dependent on the starting seed mass

concentrations in the chamber.

Table 7.2. Experimental parameters for size-selected atomized seed particle experiments before addition of α-pinene and after 3 h of α-pinene ozonolysis in the large smog chamber

Seed Particle	Sol'n Conc. (g L^{-1})	Selected Size (nm)	α-pinene (μL)	O_3 (ppb)	Particle Diameter (nm)		Mass Conc. (μg m^{-3})	
					Seed[a]	SOA[b]	Seed[a]	SOA[b]
[C$_6$MIM][BF$_4$][c]	10.2	115	5	800	200	270	82	150
[C$_6$MIM][BF$_4$][c]	1.2	100	0.3	130	113	134	8	6
[C$_6$MIM][BF$_4$][d]	5.0	105	0.3	110	118	152	7	12
[C$_2$MIM][Tf$_2$N][d]	50.1	95	1.5	200	153	205	103	143

[a] Seed particle size and/or mass concentration in the large chamber before α-pinene was added.
[b] SOA particle size and/or mass concentration in the large chamber after ~ 3 h ozonolysis of α-pinene.
[c] EC sheath/aerosol flow ration when size-selecting: 3/0.3 SLM
[d] EC sheath/aerosol flow ration when size-selecting: 15/1.5 SLM

Several seed particle solution concentrations were explored (Table 7.2). Finding the

"best" solution concentration is a major priority for future experiments. It is also worth noting

that initial attempts at size selecting seed particles used electrostatic classifier (EC) sheath and

aerosol flow rates of 3.0 and 0.3 SLM, respectively (Table 7.2). The sheath and aerosol flow

rates were increased to 15 and 1.5 SLM, respectively, (Table 7.2) in an effort to increase the

particle mass concentration in the chamber. So far, we are unable to tell if increase the flow rates

has improved the mass concentration; not enough successful experiments have been performed.

Though, it is clear that future experiments should only use the 15:1.5 ratio to ensure that enough seed particles are generated, regardless of selected size.

For all 12 experiments attempted, none of the seed particle diameters selected with the EC and long-DMA were correctly selected and measured by the SMPS (Table 7.2). The experiment that came the closest, using a 5.0 g L^{-1} [C$_6$MIM][BF$_4$] solution, attempted to select for 105 nm particles and ended up with 118 nm. While, the EC recommends which long-DMA voltages to use for selecting specific particle sizes, these parameters are merely suggestions. If seed size-selection remains a goal for the project, future work should focus on correctly size-selecting particles with the EC and long-DMA.

When sizing particles with an SMPS, a unimodal (i.e., one hump) size distribution is normally expected. For this study, trimodal particle distributions were a common occurrence for several experiments. The three modes likely result from particle charge changing between the size selection and detection steps. Specifically, the size selector will transmit particles of the correct size with charge of -1 and particles with a large size with they carry a charge of -2. In the chamber, the charge distribution can re-equilibrate resulting in 3 peaks corresponding to particle charge during size-selection/measurement of $-2/-1$, -1, -1, and -1, -2, respectively. While not desirable (a unimodal distribution would be preferable), results from experiments with trimodal distributions are still salvageable, as long as their peaks are clearly separated from each other throughout the experiment. Unfortunately, clearly defined peaks and large enough initial seed particle mass concentrations do not go hand in hand. Increasing the atomizer solution concentration increases the starting seed particle mass concentration, but it can also lead to poorly defined distributions. Attempts so far at achieving a well-defined particle distribution

inside the large chamber while simultaneously producing a high enough seed particle mass concentration for the experiment have not been successful.

The effect the atomizer solution concentration has on trimodal particle distributions for $[C_6MIM][BF_4]$ is shown in Figure 7.4a,b. It is clear from the distribution snap shots that increasing the solution concentration by a factor of ten significantly decreased the peak resolution. Poorly defined trimodal distributions are readily apparent when comparing the particle evolutions for 10.2 g L^{-1} and 1.1 g L^{-1} $[C_6MIM][BF_4]$ (Figure 7.4c,d). The difference is striking.
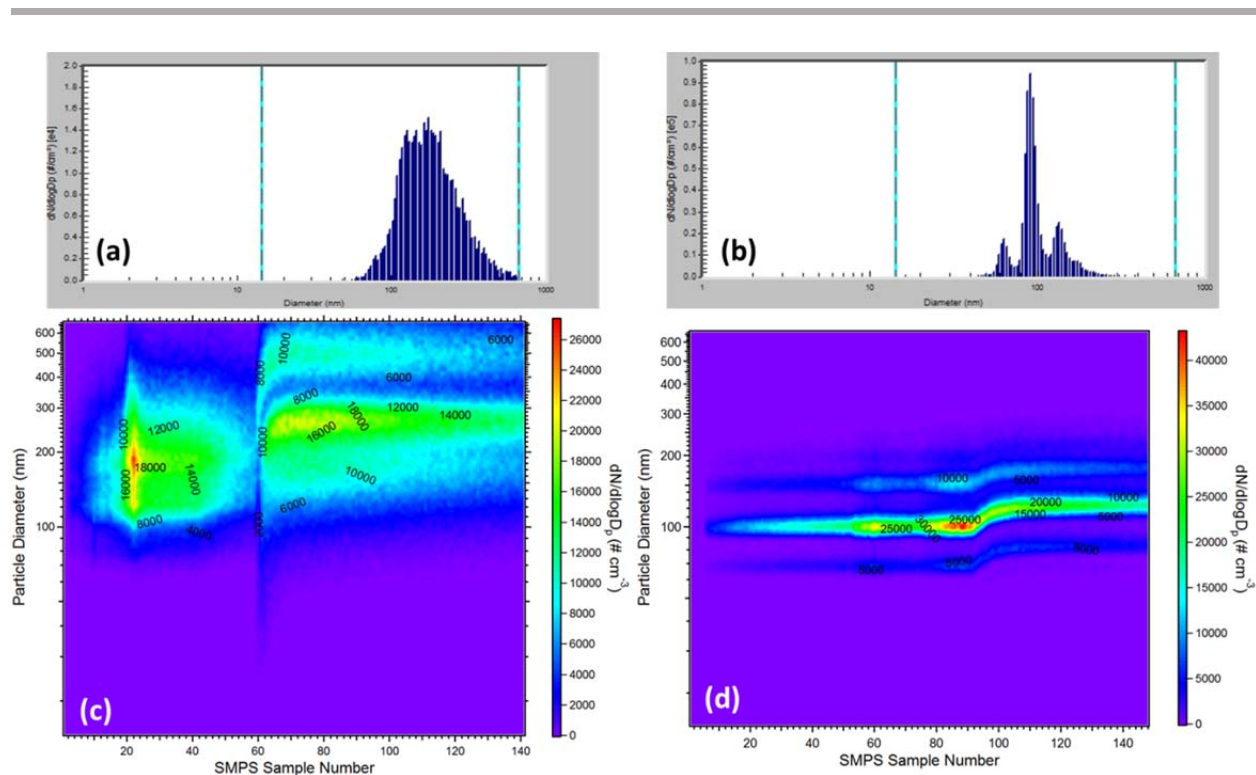
Figure 7.4. Comparison of size-selected number distribution snapshots for 10.2 g L^{-1} (a) and 1.1 g L^{-1} (b) $[C_6MIM][BF_4]$ seed particles in the large chamber. Increasing the solution concentration caused the trimodal number distribution to be poorly defined. The particle evolutions for 10.2 g L^{-1} (c) and 1.1 g L^{-1} (d) $[C_6MIM][BF_4]$ seeds provide an alternative view of solution concentrations effect on distribution definition.

Trimodal distributions were observed in both the small and large smog chamber.

However, the distributions were remarkably different considering the same solution was

atomized (made fresh daily) and the same seed particle size was selected (Figure 7.5). The same

seed material, solution concentration, and selected size (10.2 g L^{-1}, [C$_6$MIM][BF$_4$], and 115 nm,

respectively) were used in both the small and large chamber. Even when the mass concentration

in the small chamber is more than twice the concentration in the large chamber, the trimodal

number distribution remains remarkably well defined with very clear peaks (Figure 7.5b).
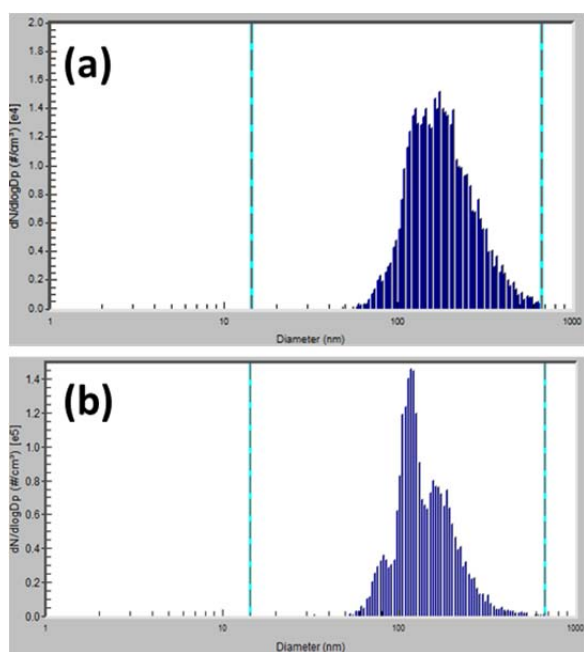
Figure 7.5. Particle number size distribution snapshots for 10.2 g L^{-1} [C$_6$MIM][BF$_4$] atomized
and size-selected for 115 nm in the large (a) and small (b) smog chamber.

The following displays the results from the best experiment conducted to date. A 50.1 g

L^{-1} solution of [C$_2$MIM][Tf$_2$N] was atomized and 95 nm seed particles were size-selected and

introduced to the large chamber. The particle mass concentration (a), number concentration (b), particle diameter (c), and particle evolution (d) are shown in Figure 7.6. Several aspects of this experiment went as planned. The seed solution was a good concentration to atomize enough particles into the chamber (Figure 7.6a). The starting seed particle size remained steady (Figure 7.6c). Though, 149 nm seed particles were actually size-selected by the EC instead of 95 nm particles) indicating that the atomizer worked correctly and there was minimal wall lose or conglomeration. There was a jump in number concentration after α-pinene was added, indicating probably too much was added (Figure 7.6b), and the trimodal distribution was not clearly defined, indicating the solution concentration was probably too high (Figure 7.6d). Though, both of those things will be improved in future experiments.
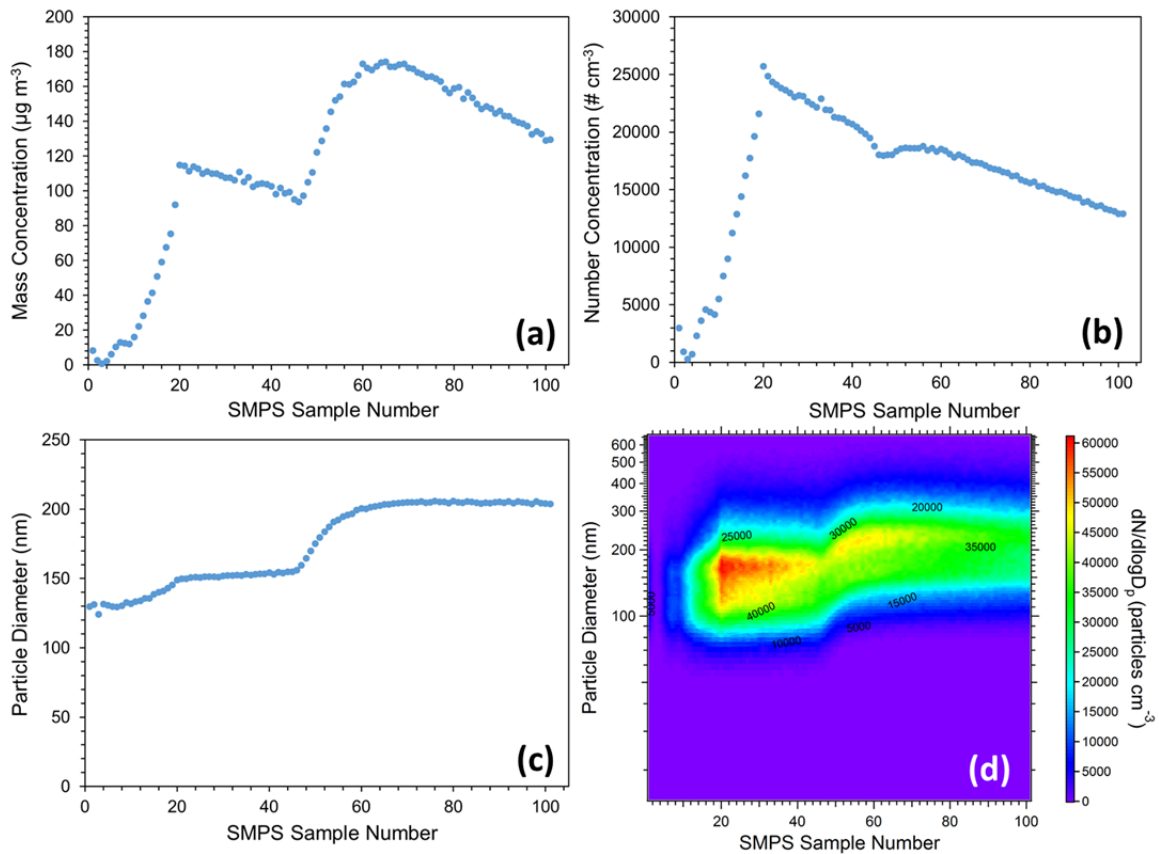
Figure 7.6. The particle mass concentration (a), number concentration (b), particle diameter (c), and particle evolution (d) for a 50.1 g L^{-1} solution of [C$_2$MIM][Tf$_2$N] that was atomized and size-selected for 95 nm seeds in the large chamber.

References

(1) Hamilton, J. F.; Rami Alfarra, M.; Wyche, K. P.; Ward, M. W.; Lewis, A. C.; McFiggans, G. B.; Good, N.; Monks, P. S.; Carr, T.; White, I. R.; Purvis, R. M. Investigating the Use of Secondary Organic Aerosol as Seed Particles in Simulation Chamber Experiments. *Atmos. Chem. Phys.* 2011, *11*, 5917-5929.

(2) Seinfeld, J. H.; Pandis, S. N. *Atmospheric Chemistry and Physics: From Air Pollution to Climate Change*; J. Wiley: Hoboken, N.J., 2006.

(3) *Ionic Liquids in Synthesis*; 2nd ed.; Wasserscheid, P.; Welton, T., Eds.; Wiley-VCH: Weinheim, Germany, 2008; Vol. 1.

(4) *Ionic Liquids as Green Solvents: Progress and Prospects*; Rogers, R. D.; Seddon, K. R., Eds.; American Chemical Society Symposium Series 856; American Chemical Society; Distributed by Oxford University Press: Washington, DC; [Cary, N.C.], 2003.

(5) Stanier, C. O.; Khlystov, A. Y.; Pandis, S. N. Nucleation Events During the Pittsburgh Air Quality Study: Description and Relation to Key Meteorological, Gas Phase, and Aerosol Parameters Special Issue of Aerosol Science and Technology on Findings from the Fine Particulate Matter Supersites Program. *Aerosol Sci. Technol.* 2004, *38*, 253-264.

(6) Kim, Y.; Yoon, S.-C.; Kim, S.-W.; Kim, K.-Y.; Lim, H.-C.; Ryu, J. Observation of New Particle Formation and Growth Events in Asian Continental Outflow. *Atmos. Environ.* 2013, *64*, 160-168.

Appendix

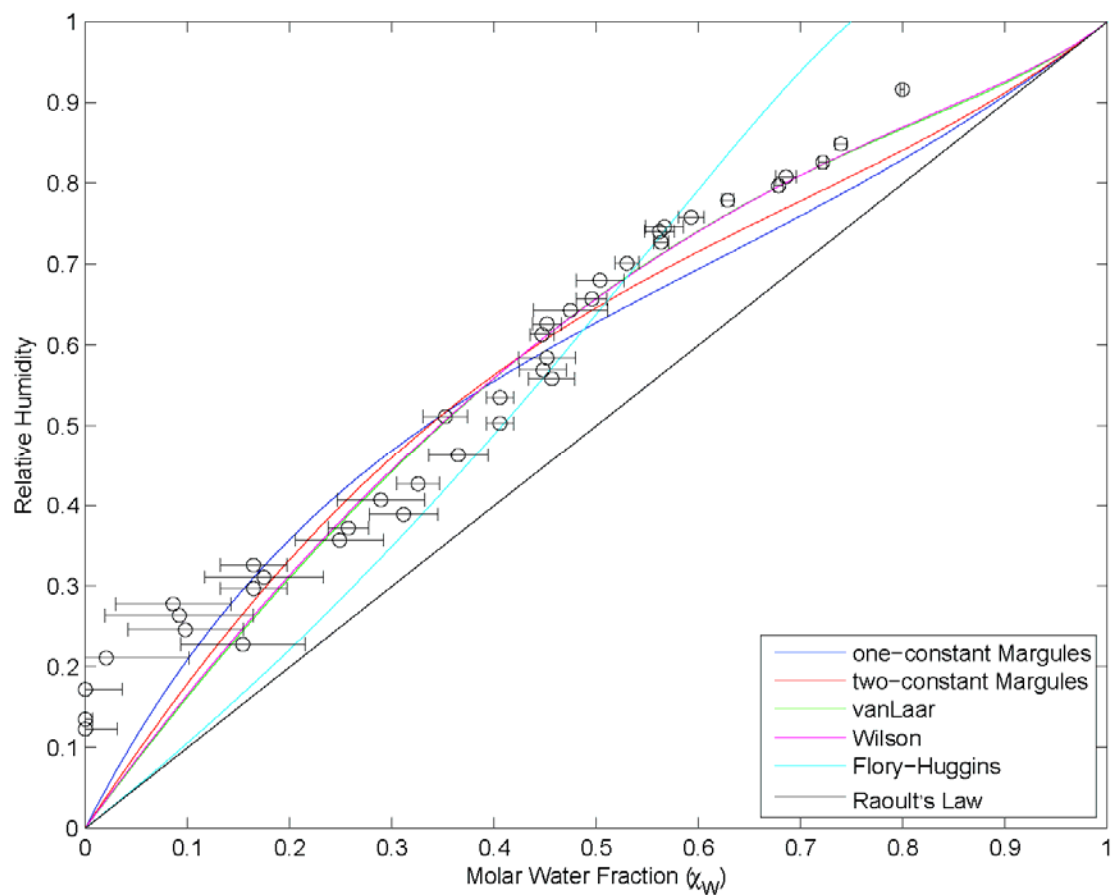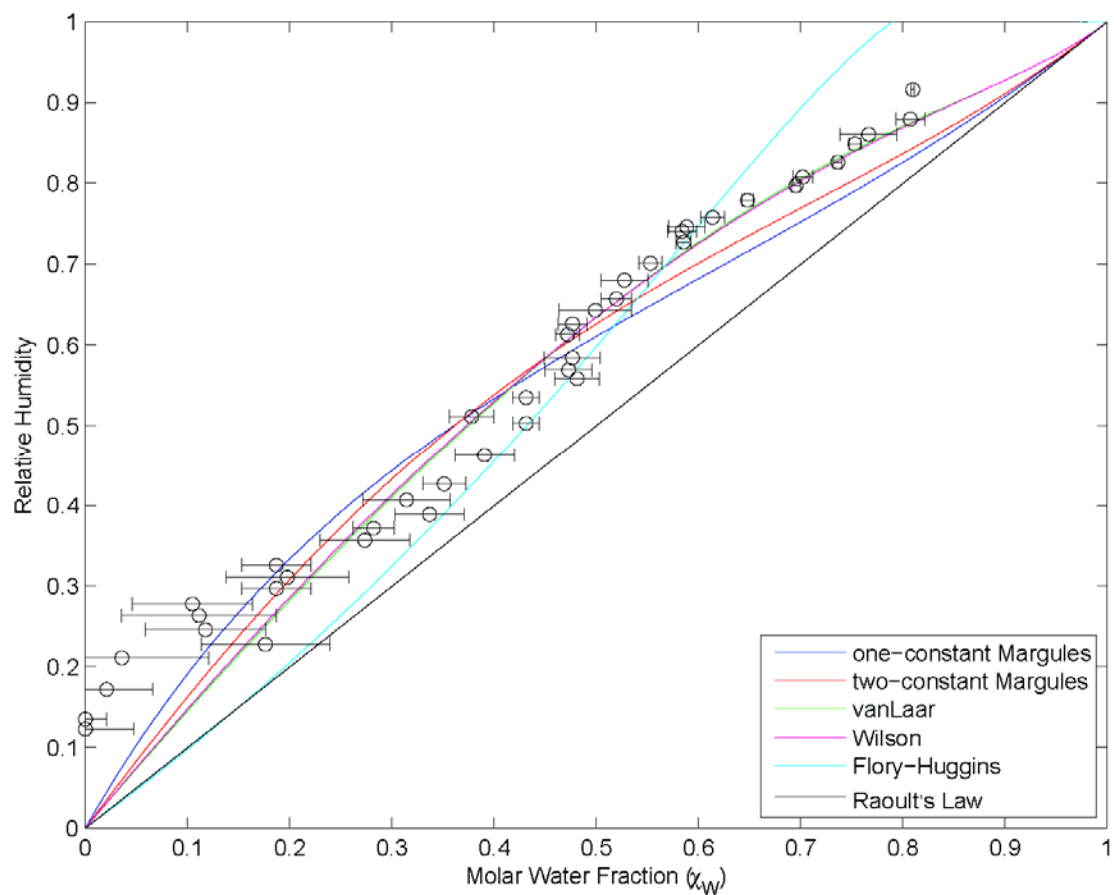# Appendix A: One- and Two-Parameter Correlative Liquid Activity

Coefficient Models
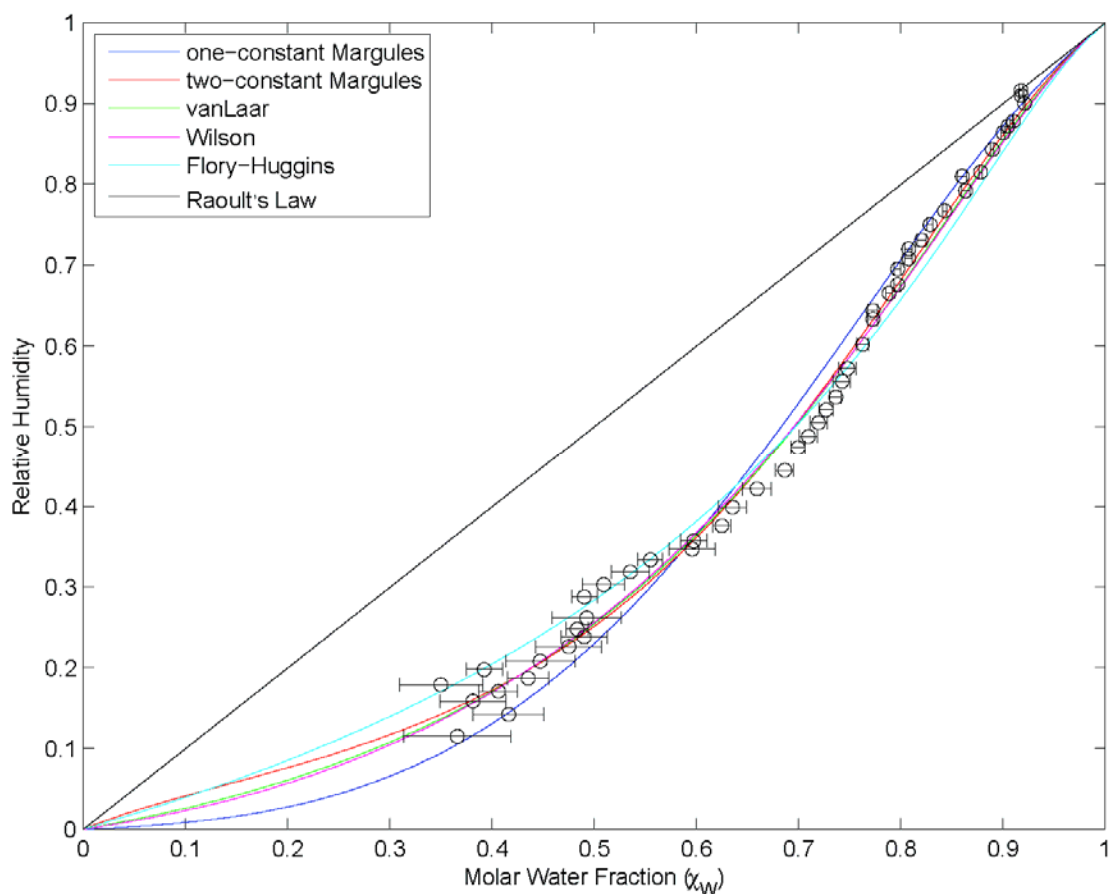
Figure A1. One- and two-parameter correlative liquid activity coefficient models used to fit the equilibrium molar fractions of water (χ_w) calculated from the [C$_4$MIM][Cl] ionic liquid nanoparticle growth factor values using eq 4.1 (actual densities). The two-parameter equations (i.e., two-constant Margules, van Larr, and Wilson models) performed better than the one-parameter equations (i.e., one-constant Margules and Flory-Huggins models). Raoult's law for an ideal solution is represented by the dark grey, solid line.
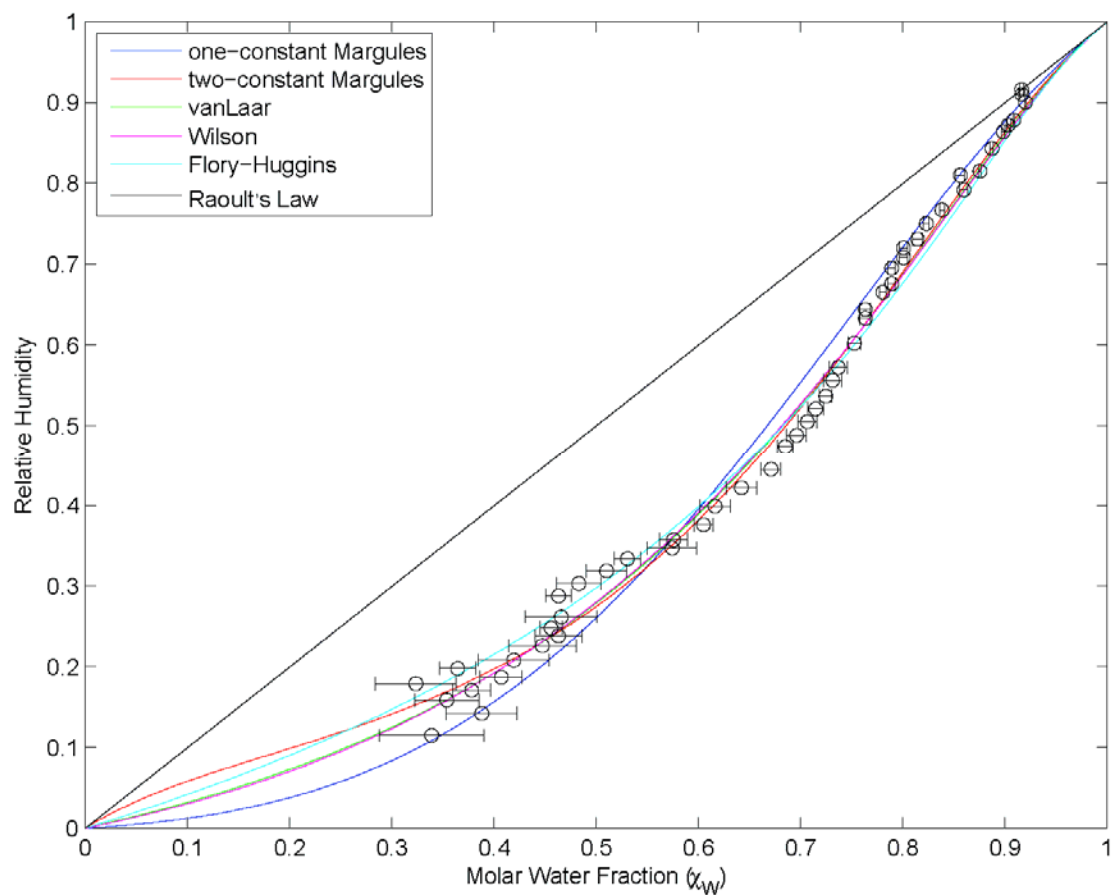
Figure A2. One- and two-parameter correlative liquid activity coefficient models used to fit the equilibrium molar fractions of water (χ_w) calculated from the [C$_4$MIM][Cl] ionic liquid nanoparticle growth factor values using eq 4.2 (ideal solution approximation). The two-parameter equations (i.e., two-constant Margules, van Larr, and Wilson models) performed better than the one-parameter equations (i.e., one-constant Margules and Flory-Huggins models). Raoult's law for an ideal solution is represented by the dark grey, solid line.
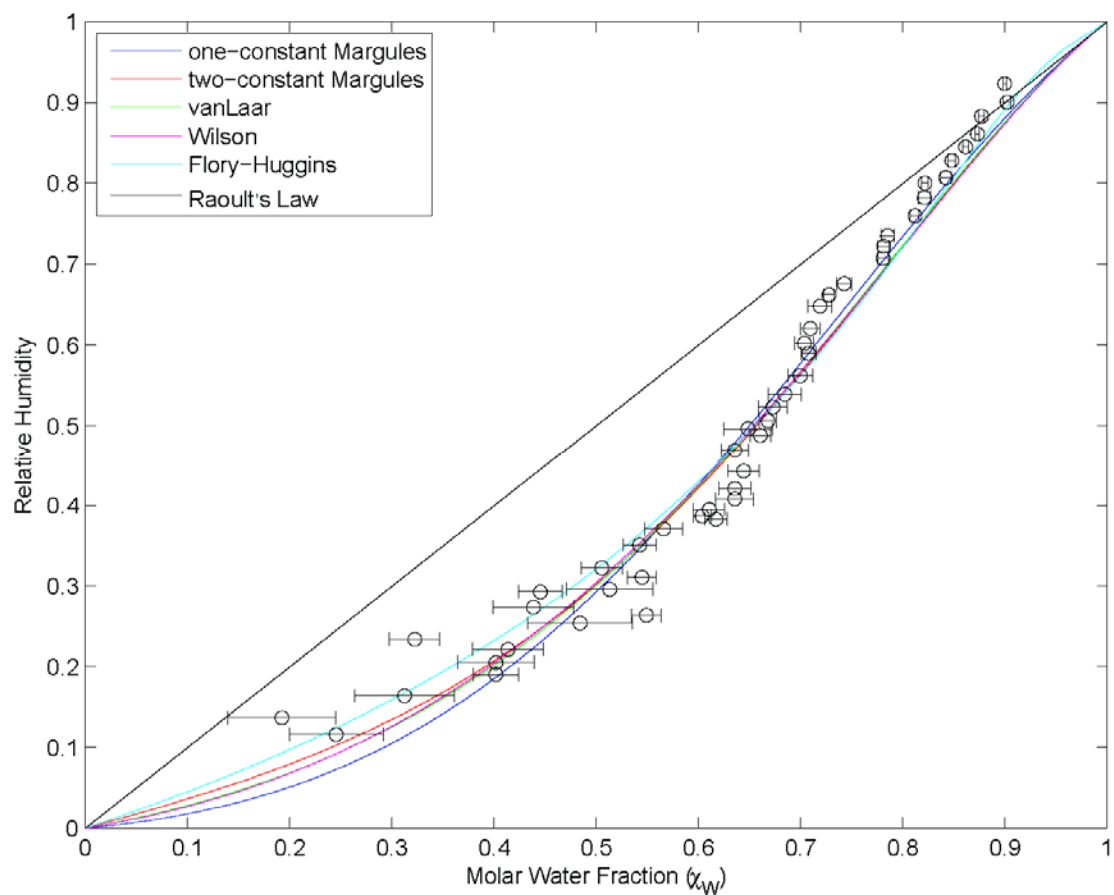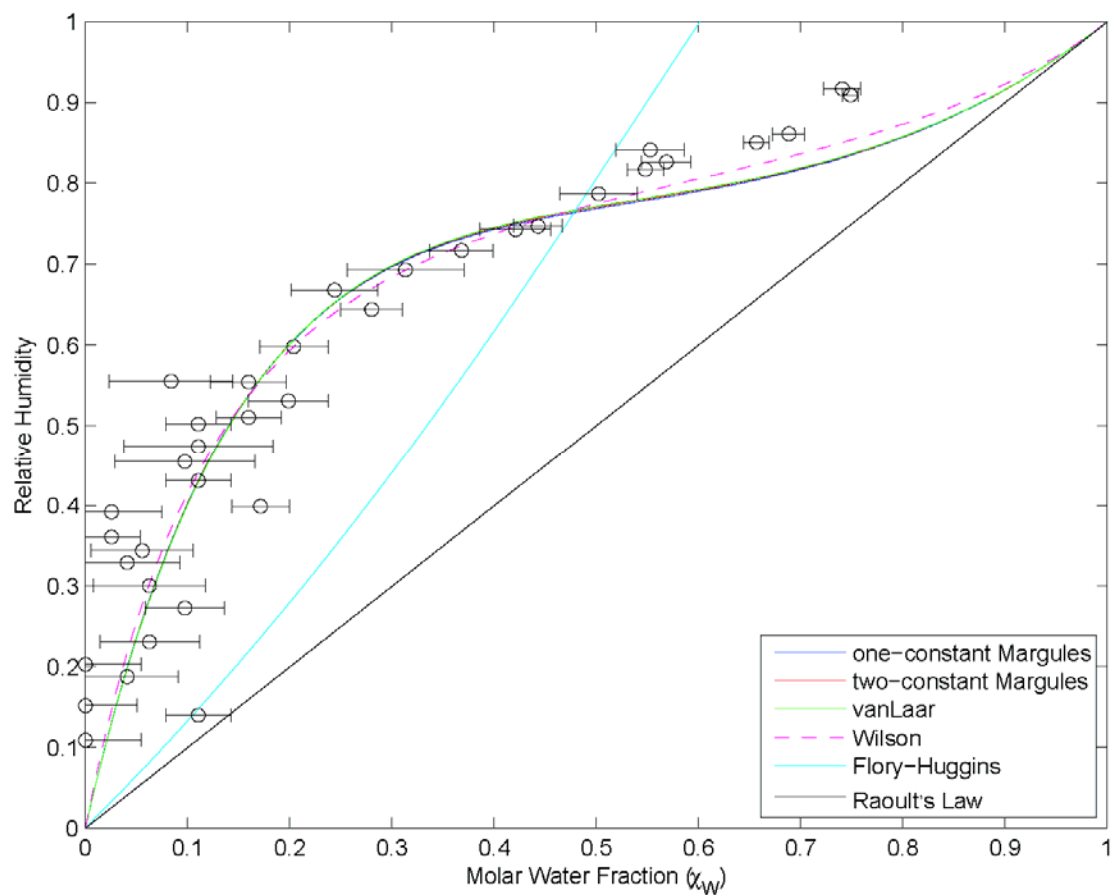
Figure A3. One- and two-parameter correlative liquid activity coefficient models used to fit the equilibrium molar fractions of water (χ_w) calculated from the [C$_6$MIM][Cl] ionic liquid nanoparticle growth factor values using eq 4.1 (actual densities). The two-parameter equations (i.e., two-constant Margules, van Larr, and Wilson models) performed better than the one-parameter equations (i.e., one-constant Margules and Flory-Huggins models). Raoult's law for an ideal solution is represented by the dark grey, solid line.
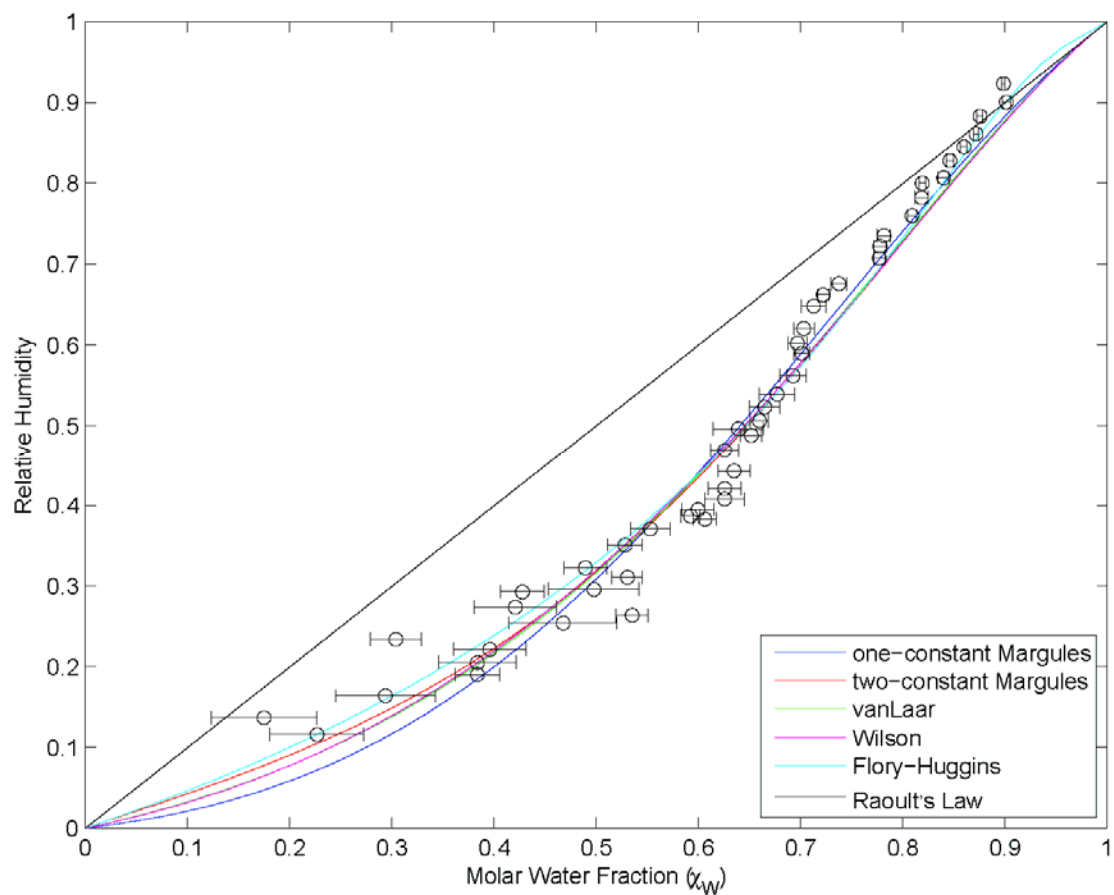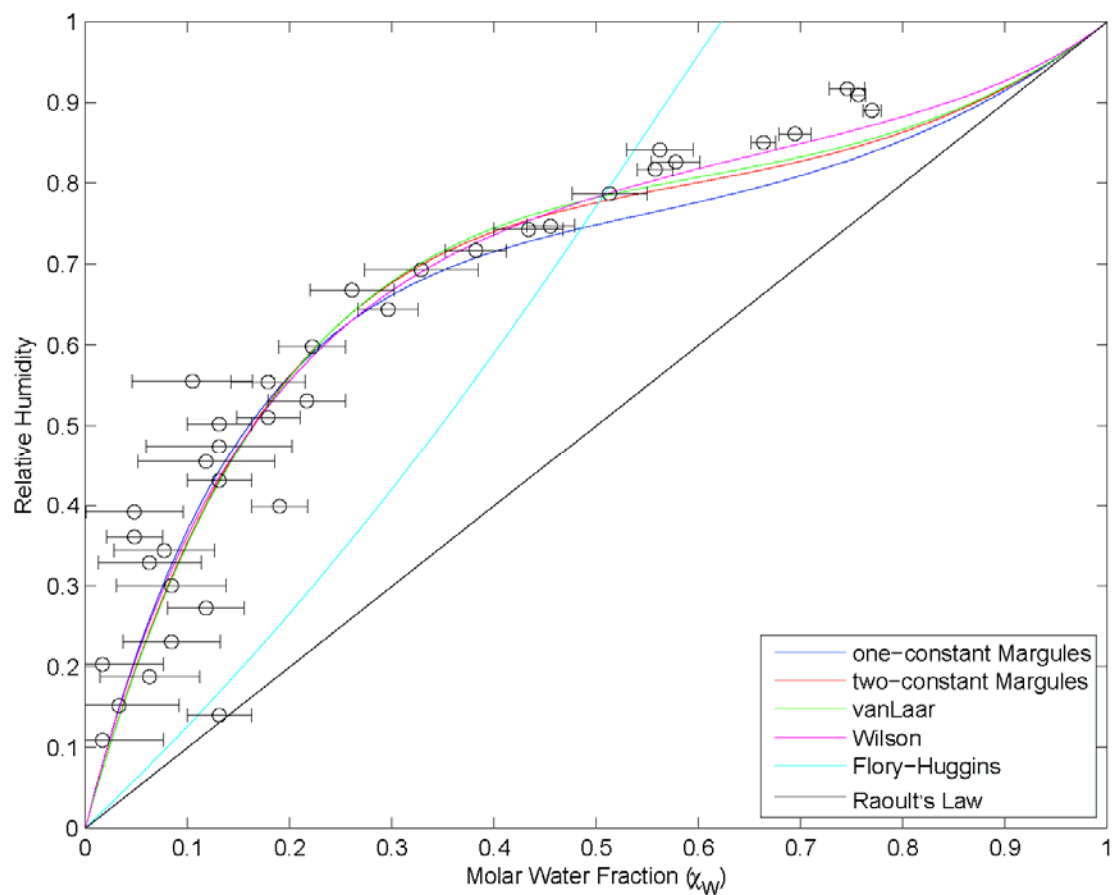
Figure A4. One- and two-parameter correlative liquid activity coefficient models used to fit the equilibrium molar fractions of water (χ_w) calculated from the [C$_6$MIM][Cl] ionic liquid nanoparticle growth factor values using eq 4.2 (ideal solution approximation). The two-parameter equations (i.e., two-constant Margules, van Larr, and Wilson models) performed better than the one-parameter equations (i.e., one-constant Margules and Flory-Huggins models). Raoult's law for an ideal solution is represented by the dark grey, solid line.
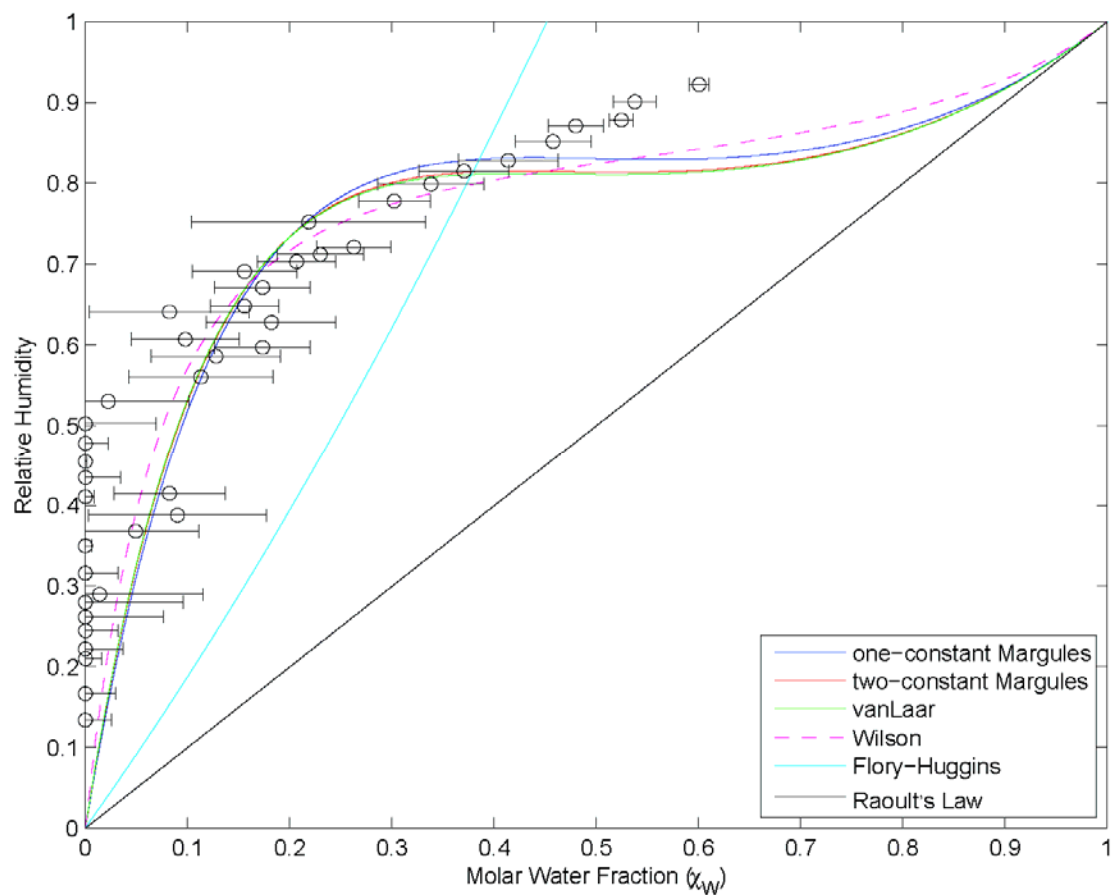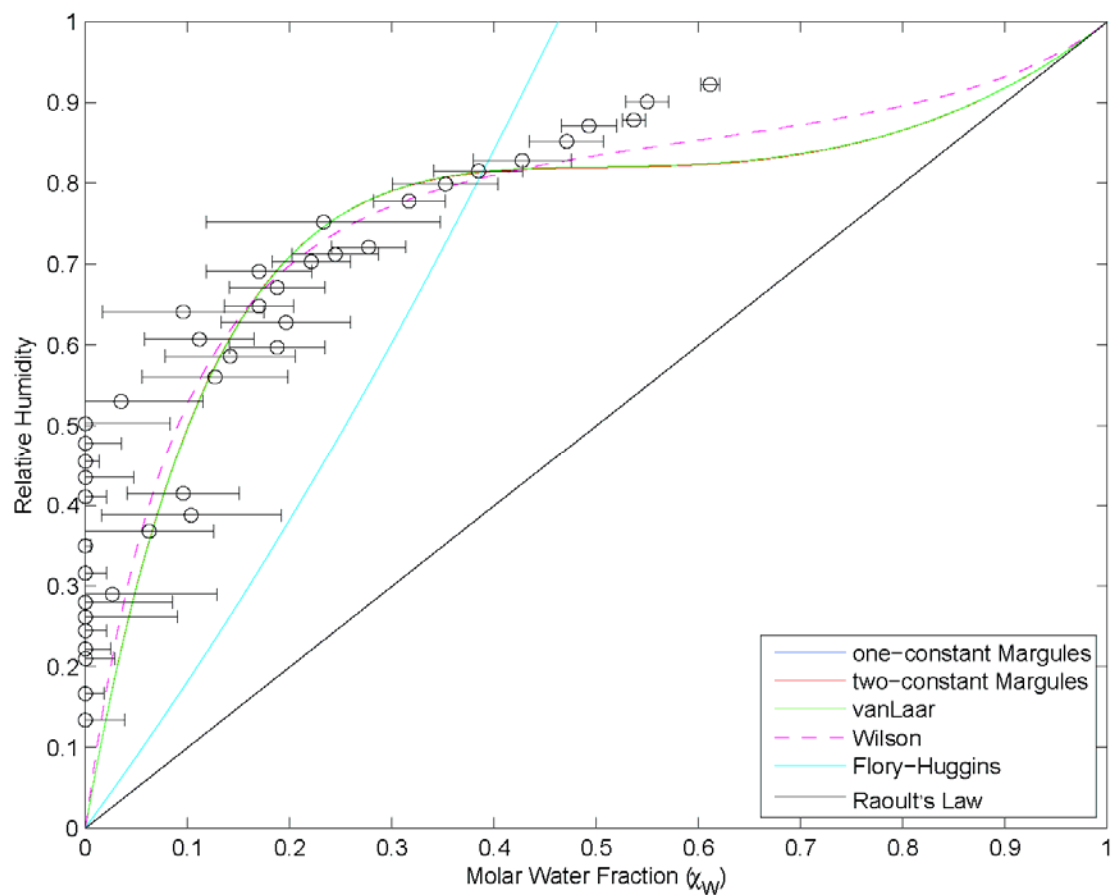
Figure A5. One- and two-parameter correlative liquid activity coefficient models used to fit the equilibrium molar fractions of water (χ_w) calculated from the [C_2MIM][BF_4] ionic liquid nanoparticle GF values using eq 4.1 (actual densities).[3] The two-parameter equations (i.e., two-constant Margules, van Larr, and Wilson models) performed better than the one-parameter equations (i.e., one-constant Margules and Flory-Huggins models). Raoult's law for an ideal solution is represented by the dark grey, solid line.

Figure A6. One- and two-parameter correlative liquid activity coefficient models used to fit the equilibrium molar fractions of water (χ_w) calculated from the [C$_2$MIM][BF$_4$] ionic liquid nanoparticle GF values using eq 4.2 (ideal solution approximation).[3] The two-parameter equations (i.e., two-constant Margules, van Larr, and Wilson models) performed better than the one-parameter equations (i.e., one-constant Margules and Flory-Huggins models). Raoult's law for an ideal solution is represented by the dark grey, solid line.

Figure A7. One- and two-parameter correlative liquid activity coefficient models used to fit the equilibrium molar fractions of water (χ_w) calculated from the [C$_4$MIM][BF$_4$] ionic liquid nanoparticle GF values using eq 4.1 (actual densities). The two-parameter equations (i.e., two-constant Margules, van Larr, and Wilson models) performed better than the one-parameter equations (i.e., one-constant Margules and Flory-Huggins models). The dashed line for the Wilson model indicates that the least-squares optimization did not converge. Raoult's law for an ideal solution is represented by the dark grey, solid line.

Figure A8. One- and two-parameter correlative liquid activity coefficient models used to fit the equilibrium molar fractions of water (χ_w) calculated from the [C$_4$MIM][BF$_4$] ionic liquid nanoparticle GF values using eq 4.2 (ideal solution approximation). The two-parameter equations (i.e., two-constant Margules, van Larr, and Wilson models) performed better than the one-parameter equations (i.e., one-constant Margules and Flory-Huggins models). Raoult's law for an ideal solution is represented by the dark grey, solid line.

Figure A9. One- and two-parameter correlative liquid activity coefficient models used to fit the equilibrium molar fractions of water (χ_w) calculated from the [C$_6$MIM][BF$_4$] ionic liquid nanoparticle GF values using eq 4.1 (actual densities). The two-parameter equations (i.e., two-constant Margules, van Larr, and Wilson models) performed better than the one-parameter equations (i.e., one-constant Margules and Flory-Huggins models). The dashed line for the Wilson model indicates that the least-squares optimization did not converge. Raoult's law for an ideal solution is represented by the dark grey, solid line.

Figure A10. One- and two-parameter correlative liquid activity coefficient models used to fit the equilibrium molar fractions of water (χ_w) calculated from the [C$_6$MIM][BF$_4$] ionic liquid nanoparticle GF values using eq 4.2 (ideal solution approximation). The two-parameter equations (i.e., two-constant Margules, van Larr, and Wilson models) performed better than the one-parameter equations (i.e., one-constant Margules and Flory-Huggins models). The dashed line for the Wilson model indicates that the least-squares optimization did not converge. Raoult's law for an ideal solution is represented by the dark grey, solid line.

Table A1. Liquid Activity Coefficient Models Exact and Ideal Fitting Parameters

	one-constant Margules		two-constant Margules			van Laar			Wilson			Flory-Huggins	
	A/RT	R^2	α/RT	β/RT	R^2	α	β	R^2	$Λ_{12}$	$Λ_{21}$	R^2	$φ_w$	R^2
[C₂MIM][Cl] Ideal	-11035 ±205	0.990	-14900 ±376	11125 ±976	0.996	-2.36 ±0.12	-4.02 ±0.05	0.995	4.17 ±0.10	3.75 ±0.75	0.994	0.00201 ±0.01967	0.956
[C₄MIM][Cl] Exact	-7690 ±310	0.982	-11944 ±597	10256 ±1264	0.992	-1.50 ±0.11	-3.06 ±0.08	0.992	3.87 ±0.19	1.34 ±0.23	0.991	0.299 ±0.017	0.981
[C₄MIM][Cl] Ideal	-6453 ±282	0.982	-11275 ±531	10678 ±1058	0.993	-1.26 ±0.09	-2.68 ±0.07	0.992	3.69 ±0.20	1.05 ±0.18	0.992	0.357 ±0.014	0.9874
[C₆MIM][Cl] Exact	-5300 ±269	0.970	-7354 ±823	4720 ±1741	0.971	-1.49 ±0.28	-2.09 ±0.10	0.971	2.67 ±0.30	1.61 ±0.50	0.968	0.601 ±0.017	0.969
[C₆MIM][Cl] Ideal	-4768 ±255	0.971	-6857 ±767	4731 ±1570	0.972	-1.300 ±0.24	-1.89 ±0.10	0.971	2.59 ±0.31	1.40 ±0.42	0.970	0.631 ±0.016	0.974
[C₂MIM][BF₄] Exact	2254 ±172	0.907	3484 ±790	-1891 ±1190	0.922	0.528 ±0.095	1.36 ±0.26	0.934	1.31 ±0.25	0.176 ±0.094	0.934	1.27 ±0.04	0.898
[C₂MIM][BF₄] Ideal	1981 ±167	0.922	3153 ±729	-1851 ±1120	0.934	0.397 ±0.073	1.36 ±0.29	0.949	1.54 ±0.24	0.148 ±0.078	0.948	1.19 ±0.04	0.915
[C₄MIM][BF₄] Exact	4260 ±175	0.823	4325 ±1106	-81 ±1357	0.824	1.71 ±0.13	1.73 ±0.18	0.825	0.314 ±0.068	0.284 ±0.084	0.834	1.68 ±0.10	0.601
[C₄MIM][BF₄] Ideal	3999 ±147	0.841	4958 ±906	-1205 ±1125	0.863	1.50 ±0.10	1.80 ±0.17	0.867	0.431 ±0.070	0.231 ±0.068	0.874	1.62 ±0.09	0.645
[C₆MIM][BF₄] Exact	5030 ±279	0.624	4490 ±2109	679 ±2600	0.616	2.10 ±0.25	1.94 ±0.31	0.615	0.181 ±0.088	0.220 ±0.124	0.624	2.17 ±0.11	0.360
[C₆MIM][BF₄] Ideal	4900 ±279	0.625	4880 ±2082	27 ±2596	0.625	1.98 ±0.24	1.98 ±0.33	0.626	0.233 ±0.105	0.191 ±0.126	0.634	2.14 ±0.11	0.395
Average R^2		0.876			0.883			0.885			0.888		0.789
R^2 of [CₙMIM][Cl]		0.979			0.985			0.984			0.983		0.974
R^2 of [CₙMIM][BF₄]		0.790			0.797			0.802			0.808		0.636